2017

Pore Formation in Aluminum Castings: Theoretical Calculations and the Extrinsic Effect of Entrained Surface Oxide Films

Pedram Yousefian

UNF UNIVERSITY *of* NORTH FLORIDA.

Pore Formation in Aluminum Castings:

Theoretical Calculations and the Extrinsic Effect of

Entrained Surface Oxide Films

by

Pedram Yousefian

A thesis submitted to the School of Engineering

in partial fulfillment of the requirements for the degree of

Master of Science in Mechanical Engineering

UNIVERSITY OF NORTH FLORIDA

COLLEGE OF COMPUTING, ENGINEERING, AND CONSTRUCTION

July 2017

The thesis "Pore Formation in Aluminum Castings: Theoretical Calculations and the Extrinsic Effect of Entrained Surface Oxide Films" submitted by Pedram Yousefian in partial fulfillment of the requirements for the degree of Master of Science in Mechanical Engineering has been

Approved by the thesis committee: **Date**

_____   _____

Dr. Murat Tiryakioğlu

Thesis Advisor and Committee Chairperson

_____   _____

Dr. Paul Eason

_____   _____

Dr. Stephen Stagon

Accepted for the School of Engineering:

_____   _____

Dr. Murat Tiryakioğlu

Director of the School

Accepted for the College of Computing, Engineering, and Construction:

_____   _____

Dr. Mark Tumeo

Dean of the College

Accepted for the University:

_____   _____

Dr. John Kantner

Dean of the Graduate School

Dedication

…to my supervisor, Dr. Murat Tiryakioǧlu

Without whom I couldn't do it

ACKNOWLEDGMENTS

TABLE OF CONTENTS

Page

LIST OF TABLES

LIST OF FIGURES

NOMENCLATURE

Symbol		Meaning
α	:	Atomic packing factor
θ	:	Wetting angle
ΔG_0	:	the free energy of activation for the motion of an individual molecule of liquid past its neighbors into or away from the pore surface
ΔP	:	Pressure difference between the exterior and the interior of the pore (GPa)
λ_{DA}	:	Dendrite arm spacing (μm)
σ	:	Bulk surface energy per unit area (J/m2)
σ_{eff}	:	Effective surface energy (J/m2)
σ_f	:	Fatigue strength
σ_{LP}	:	Liquid-pore surface energy (J/m2)
σ_{LO}	:	Liquid-solid surface energy (J/m2)
σ_{PO}	:	Pore-solid surface energy (J/m2)
γ	:	Curvature energy (N)
ρ	:	Density (kg/m3)
C_{AP}	:	Atomic packing factor
c_v	:	Vacancy concentration
E_n	:	Formation energy of a spherical cluster of vacancy (J)
E_v	:	Formation energy of a vacancy (J)
f		Density function
F_A	:	Area fraction of pores
F_P	:	Probability
f_V	:	Volume fraction of pores
P	:	Pressure (GPa)
h	:	Planck's constant (J.s)
H_V	:	Molecular heat of vaporization (J)
HV	:	Vickers Hardness
J_0	:	Nucleation rate factor (s-1)
J	:	Nucleation rate (s-1)
k	:	Boltzmann's constant (J.K-1)
M	:	Molar mass (kg/mol)
n	:	Number of atoms/vacancies
N_A	:	Avogadro's number (mol-1)
N_P	:	Number of pores per bulk volume (mm^{-3})
r	:	Radius of nuclei/atoms/vacancies (nm)
T	:	Temperature (K)
V	:	Volume (m^3)
W	:	Work (J)
W_s	:	Required energy to form a vacancy cluster containing n vacancies in the absence of gas (J)

Subscripts:

*	:	Critical
A	:	Atom
atm	:	Atmosphere
e	:	External
g	:	Gas
H	:	Hydrostatic
Het	:	Heterogeneous
Hom	:	Homogeneous
l	:	Liquid
s	:	Shrinkage
V	:	Vacancy

ABSTRACT

Aluminum alloy castings are being integrated increasingly into automotive and aerospace assemblies due to their extraordinary properties, especially high strength-to-density ratio. To produce high quality castings, it is necessary to understand the mechanisms of the formation of defects, specifically pores and inclusion, in aluminum. There have been numerous studies on pore formation during solidification which lead to hot tearing and/or reduction in mechanical properties. However, a comprehensive study that correlates pore formation theory with *in situ* observations and modeling assumptions from the literature as well as experimental observations in not available. The present study is motivated to fill this gap.

An in-depth discussion of pore formation is presented in this study by first reinterpreting *in situ* observations reported in the literature as well as assumptions commonly made to model pore formation in aluminum castings. The physics of pore formation is reviewed through theoretical fracture pressure calculations based on classical nucleation theory (i) for homogeneous and heterogeneous nucleation, and (ii) with and without dissolved gas, i.e., hydrogen. Based on the fracture pressure for aluminum, critical pore size and corresponding probability of vacancies clustering to form the critical-size pore have been calculated by using thermodynamic data reported in the literature. Calculations show that it is impossible for a pore to nucleate either homogeneously or heterogeneously in aluminum, even with dissolved hydrogen. The formation of pores in aluminum castings can only be explained by inflation of entrained surface oxide films entrained during prior damage to liquid aluminum (bifilms) under reduced pressure and/or with dissolved gas, which involves only growth, avoiding any nucleation problem. This mechanism is consistent with reinterpretations of *in situ* observations as well as assumptions made in the literature to model pore formation.

To determine whether damage to liquid aluminum by entrainment of surface oxides can be observed and measured, Reduced Pressure Tests (RPT) have been conducted by using high

quality, continuously cast A356.0 aluminum alloys ingots. Analyses of RPT samples via micro-computer tomography (μ-CT) scanning have demonstrated that number of pores and volume fraction of pore in aluminum casting increased by raising the pouring height (i.e., velocity of the liquid). Moreover, pore size distributions were observed to be lognormal, consistent with the literature.

Cross-sections of RPT samples have been investigated via scanning electron microscopy. In all cases, the presence of oxygen was detected inside, around and between the pores. The existence of oxide films inside all pores indicates that oxide films act as initiation sites for pores and hydrogen only assist to growth of pores. For the first time, the pore formation is reconciled with physical metallurgy principles, supported by observations of oxide films in aluminum castings. Results clearly indicate that pores are extrinsic defects and can be eliminated by careful design of the entire melting and casting process.

1. Introduction

Aluminum is the second most plentiful metallic element on earth, with the significant properties such as its light weight, strength, recyclability, corrosion resistance, durability, ductility, formability and conductivity. Therefore it is not surprising that it has become an economic competitor of steels in a variety of engineering applications, especially since the end of the 19th century [1]. Currently, the annual production of aluminum is higher than all other non-ferrous metals combined.

Due to its good combination of engineering properties, aluminum alloys have been used in aerospace and automotive industries. Examples of the use of aluminum alloys in aerospace and automotive applications are provided in Figure 1, respectively. Demands such as reduced pollution, improved fuel efficiency and increased performance have been the driving force to replace ferrous components with aluminum alloy [2].
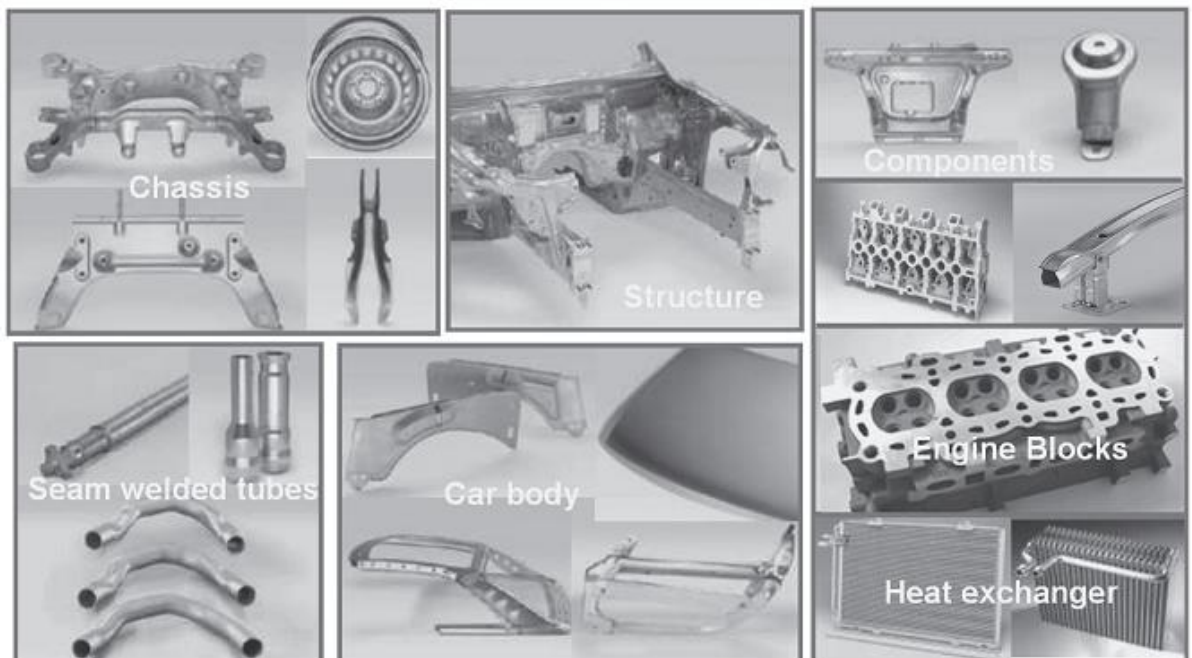
Figure 1. Aluminum products for advanced automotive applications [3]

One factor limiting wider use of aluminum castings is the profusion of structural defects [4], such as pores and entrained oxide films, which degrade mechanical properties such as tensile strength [5, 6], elongation [7-11], as well as fatigue life [6, 12-15]. A pore that initiated a fatigue crack in a 319-aluminum alloy casting is presented in Figure 2, and an entrained and folded-over oxide film, i.e., bifilm found on the fracture surface of an A356 aluminum alloy casting is presented in Figure 3.
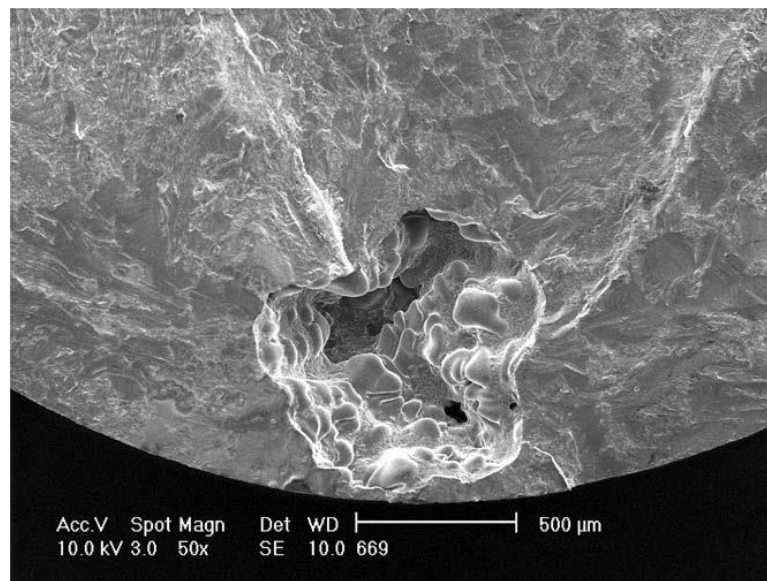
Figure 2. Fatigue crack initiating pore near surface of a 319 aluminum alloy casting [16].
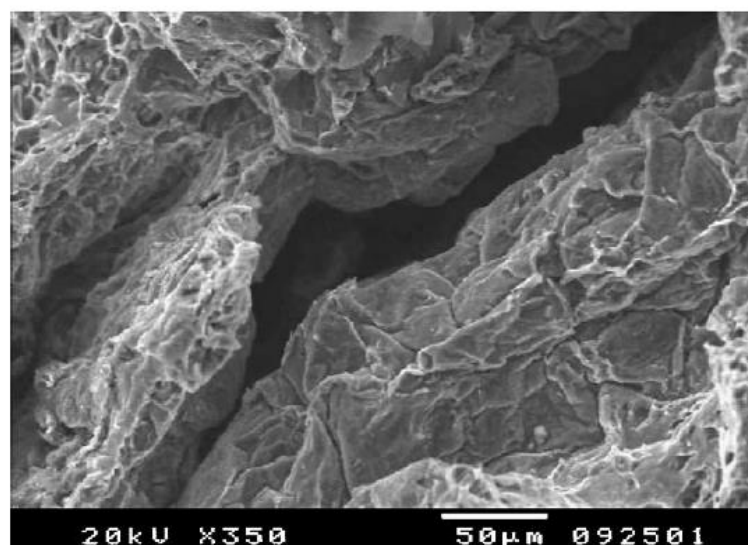
Figure 3. An oxide film found on the fracture surface of an A356 alloy casting [17].

Tiryakioğlu [10] demonstrated how area fraction of pores reduced the elongation of A356-T6 alloy castings with a yield strength of 250 MPa, which is presented in Figure 4.a. Tiryakioğlu [10] also showed 1% area fraction of porosity is sufficient to reduce elongation by 50%. Similar results were reported by Liu and Samuel [18] for the effect of oxide films on elongation, Figure 4.b.
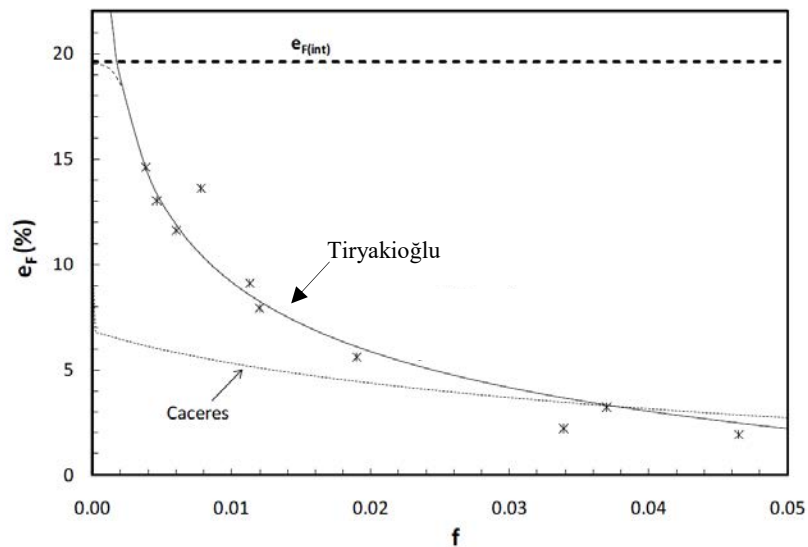
(a)
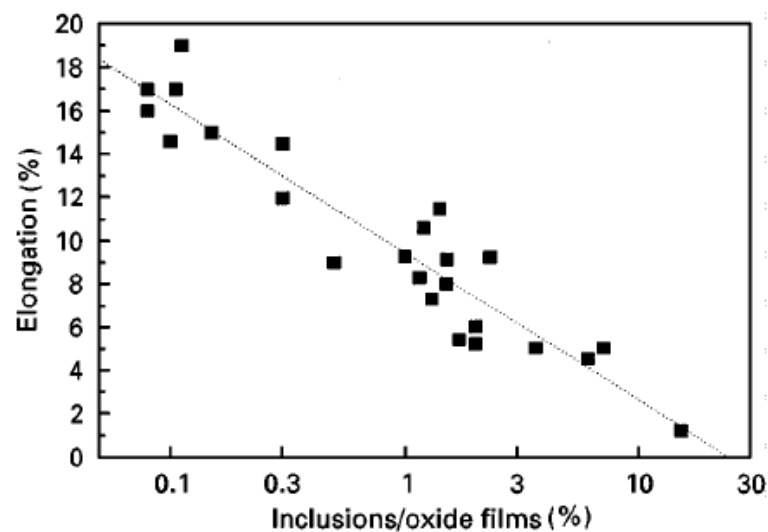
(b)

Figure 4. The effect of area fraction of defects on elongation of A356 aluminum alloy castings: (a) the effect of area fraction of pores (f) [10], and (b) effect of area fraction of oxides [18].

Wang et al. [19] also discussed that there is a relationship between fatigue strength, σ_f, at 10^7 cycles and the size of the largest pore in various Al-Si-Mg-(Cu) alloy castings, shown in Figure 5. Tiryakioğlu [20, 21] showed that there is a direct relationship between the largest pore size (A_i) and fatigue life, N_f, as presented in Figure 6.
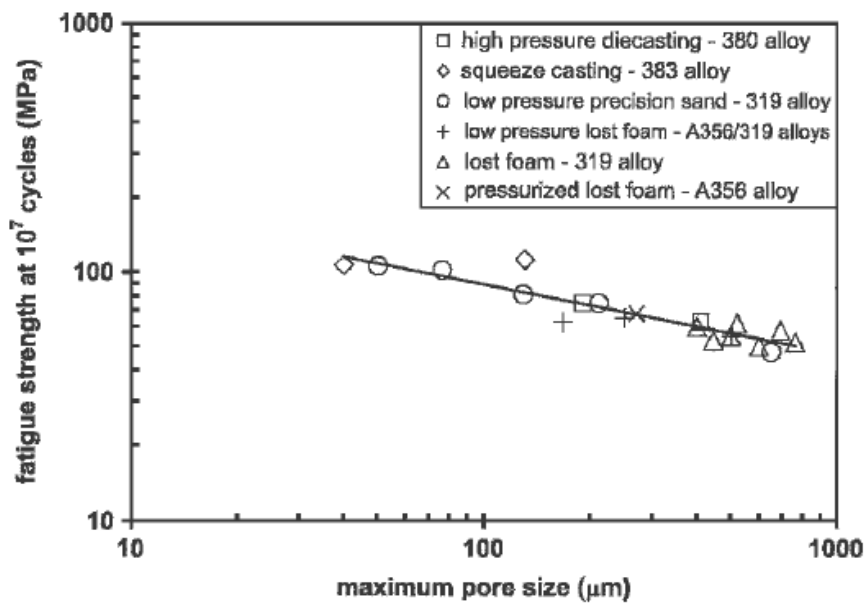
Figure 5. The relationship between maximum pore size and fatigue strength at 10^7 cycles determined in various Al-Si-Mg-(Cu) aluminum alloy castings [19].
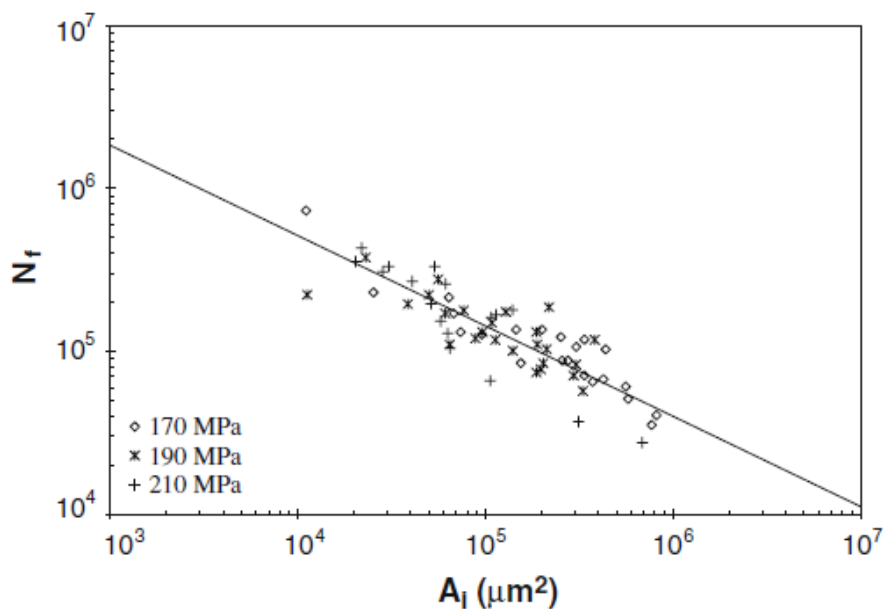
Figure 6. The change in fatigue life with area of the largest pore in A356 castings, obtained originally at three different alternating stress levels, later transformed to the same alternating stress [21].

In addition, pores can lead to rejection of the aluminum castings during final nondestructive inspection, such as radiographic inspection according to ASTM-E155. Moreover, pores have been observed [22] to initiate hot tears, which are common in high strength cast aluminum alloys, such as the Al-Cu alloys. Therefore, understanding pore formation is paramount to lowering production costs through elimination rejections, increasing their quality and performance, and consequently their wider use.

1.1. Pore Types

It is commonly assumed that pores nucleate in the last stages of solidification [23], by shrinkage and/or rejection of dissolved gas by the solidifying metal. Porosity formation in aluminum alloys can be classified as follows:

According to size:

a. macroporosity

b. microporosity

According to cause:

a. shrinkage

b. gas

These categories are not hard distinctions, but they do provide a starting point for an introduction. Pores have been characterized based on their appearance on micrographs, as either shrinkage or gas pores. Two examples are presented in Figure 7 [24], where the pore presented in Figure 7.a has a tortuous shape because it is surrounded by the tips of dendrites and as a result, is interpreted as a shrinkage pore. The pore in Figure 7.b, however, is circular, and consequently, is interpreted as a gas pore.
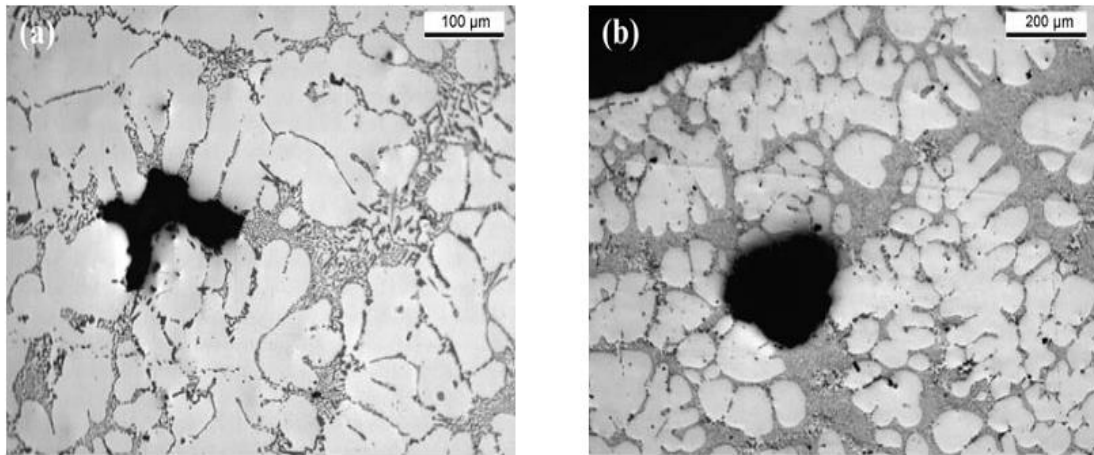
Figure 7. Pores in a low-pressure die cast A356 engine block, interpreted as a (a) shrinkage, and (b) gas pore [24].

The shrinkage porosity emerges due to the density difference between the solid and liquid alloy phases. By proceeding of solidification, the volume reduces and liquid around it flows in to compensate. Depending on the amount and distribution of solid, the fluid flow may be disrupted or even completely blocked. When sufficient liquid cannot flow in, the solid may flow in (a process known as solid feeding, and is essentially the plastic collapse of the casting by a creep process at the high temperatures involved). If neither liquid nor solid can feed the shrinkage, a large internal tensile stress develops that may be sufficient for pore formation.

The gas porosity may arise from entrained gas during pouring, from reaction between liquid metal and molding material, or may be precipitated during solidification as a result either of chemical reaction or of a the solubility difference of gas in the solid and in the liquid [25].

The solubility of a hydrogen in liquid aluminum is a function of the external pressure in accordance with Sievert's Law, which introduces the solubility of a gas in a metal at constant temperature is proportional to the square root of its external partial pressure.

$$H_2 \rightleftharpoons 2[H] \tag{1}$$

$$K = \frac{[H]}{\sqrt{P_{H_2}}} \tag{2}$$

The influence of temperature on solubility of hydrogen in aluminum presented in Figure 8. Since the partition coefficient is approximately 0.05, corresponding to a concentrating effect of 20 times in the solid, some of the gas will be rejected from solution during solidification.
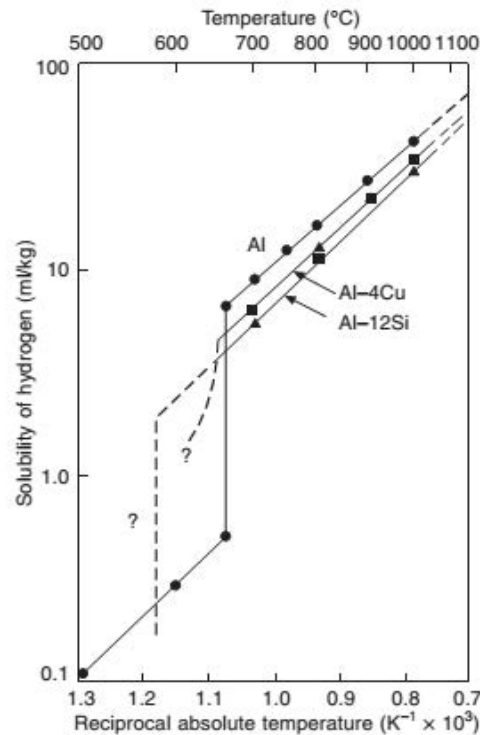
Figure 8. Hydrogen solubility in aluminum and two of its alloys [4]

Because most aluminum castings have an abundance of pores, some researchers have stated that pores are intrinsic defects [26, 27] and therefore cannot be eliminated. Whether pores are indeed intrinsic defects is addressed in this study, by reviewing and reinterpreting previous results of pore formation observations, common assumptions made in pore formation models and the physics of pore formation. The differences between observations and the physics of pore nucleation are addressed and a mechanism that bridges the gap between physics and observations is discussed.

Research Question 1: Are pores extrinsic defects or intrinsic?

1.2. A Review of *In Situ* Observations of Pore Formation

Researchers have used a variety of methods to investigate pore formation during solidification, including

- metallography of samples from castings after solidification,

- metallography of castings quenched while partially solidified,

- in situ observation pores formed in transparent organic materials [28] with low melting points which behave similarly to metals, such as cyclohexane [29] and succinonitrile acetone [22] with isothermal [30, 31] and gradient [32, 33] microscope stages

- *in situ* observation of pores in solidifying metals via x-rays

In this study, the results from the last group will be discussed.

In one of the earlier *in situ* studies using x-rays, Lee and Hunt [34] investigated pore formation in a directionally solidifying Al-Cu alloy. Four images from their observations are presented in Figure 9, in which a pore is indicated by an arrow. Note that the pore is not spherical and has a minor axis of approximately 0.2 mm. Non-spherical pores were also reported by Arnberg and Mathiesen [35] in their *in situ* study of solidification of an Al-30%Cu alloy by using x-ray radiography. Yin and Koster [36] observed how pore shape evolves with solidification time in their study with pure aluminum. The x-ray radioscopic images of the pore observed by Yin and Koster are presented in Figure 10. The pore presented in Figure 10.a is approximately 2 mm in diameter and appears near the solid-liquid interface when solid fraction, f_S, is 0.24. In Figure 10.b, the pore has grown in size to about 5 mm in diameter, maintaining its spherical shape, which becomes elongated in Figure 10.c, when the interfaces move. When the solidification is complete, the pore is not only elongated, but also has a tail, most probably due to liquid metal being sucked away due to solidification shrinkage. Yin and Koster attributed the pore formation to the supersaturation of hydrogen near the solid liquid interface due to the rejection of hydrogen by solidifying aluminum. Similarly, Catalina et al.

[37] also observed in an Al-0.25wt.%Au alloy that a spherical pore formed away from the liquid-solid (S/L) interface and became elongated once it interacted with it.
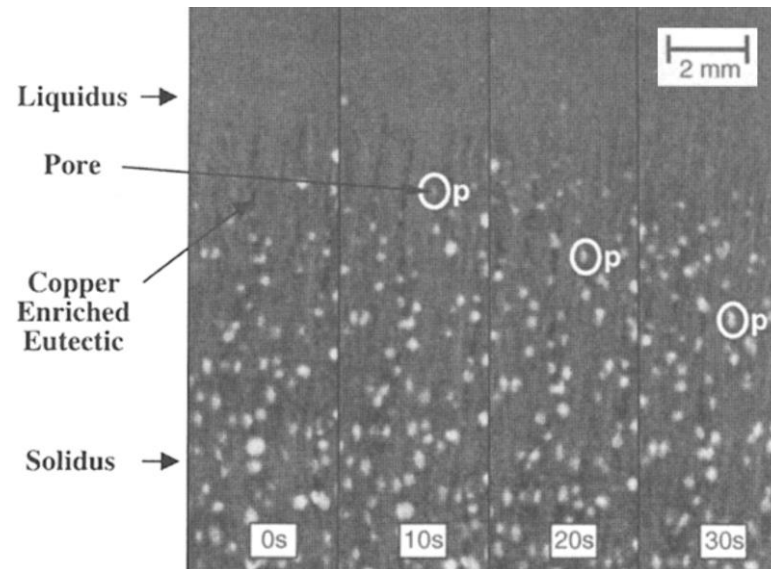
Figure 9. Sequence of *in situ* X-ray radioscopic images of pore growth during solidification of an Al-Cu alloy [38].

Murphy et al. [39] conducted solidification experiments on a grain-refined Al-20wt.%Cu alloy at very low cooling rates (0.084 K/s). Their observations at a solid fraction of 0.13 are presented in Figure 11. Note that spherical pores at t=91 s are approximately 100µm in diameter and they push the grains indicated (indicated in color) as they grow while maintaining their spherical shape.
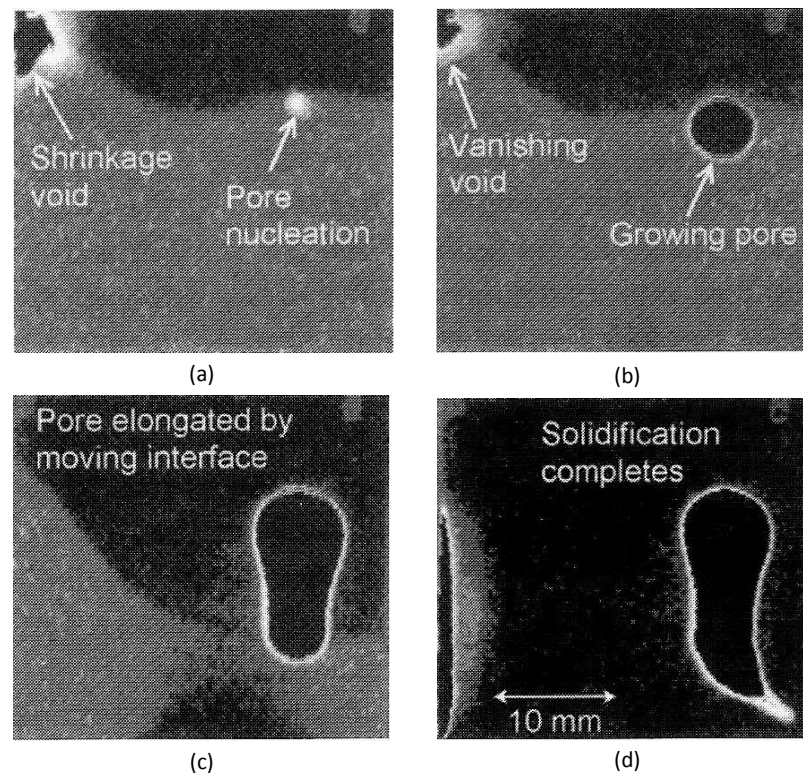
Figure 10. Sequence of in-situ X-ray radioscopic images of pore nucleation and growth during solidification of pure aluminum [36].
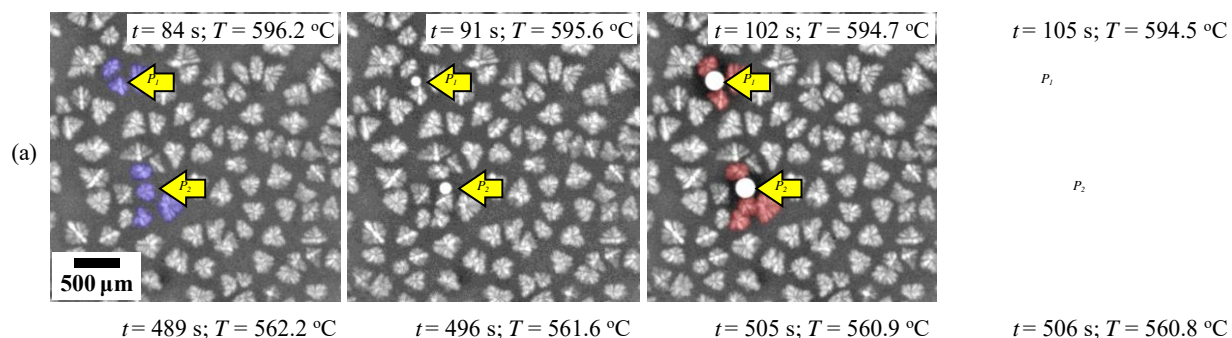
Figure 11. The solidification of grain refined Al-20wt.%Cu sample. The locations of pores are indicated by arrows. Grains that were affected by the nucleation and growth of pores are indicated in color (Courtesy of D. Browne).

Lei [40] studied pore formation during directional solidification of Al-7wt.%Si and Al-12wt.%Si alloys. They observed that pores appeared in the liquid at a distance of approximately 15 mm from the eutectic S/L interface, where the hydrogen supersaturation is usually expected to be quite low. Their results for the Al-7wt.%Si alloy are shown in Figure 12. Note that pores have diameters as low as ~150 µm and are approximately spherical at t=75s. However starting at t=90s, they progressively become tortuous, probably due their interaction with dendrites.
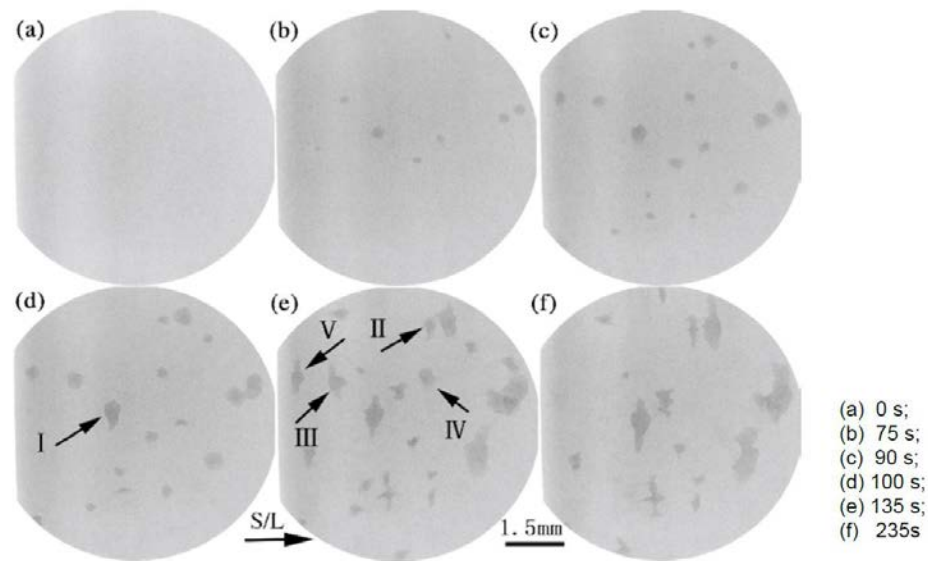
Figure 12. The solidification sequence of an Al-7wt%Si sample. Pores are almost spherical at t=75s but they become increasing more tortuous with increasing time [40].

The results outlined above from in situ observations via x-rays in the literature show that pores can form (a) at a low solid fraction, (b) away from S/L interface, (c) usually as spheres and (d) their final shape, i.e, what can be observed on a metallographic section, such as the ones in Figure 7, cannot be used to describe how they have nucleated. Even whether pores actually nucleate in aluminum has been questioned by Arnberg and Mathiesen [35] who suspected that only pore growth could be observed in *in-situ* experiments. This hypothesis is supported by the findings of Kato [41] who investigated high purity copper in an atmosphere of H_2-Ar gas mixture. He observed that pores were formed heterogeneously on oxide films of aluminum and silicon when the hydrogen partial pressure in the atmosphere exceeded 0.3 atm. Hence, while pore formation was studied in several studies, it remains unclear whether the actual nucleation of pores has ever been observed.

1.3. Application of the Classical Nucleation Theory to Pores in Castings

The physics of nucleation in condensed systems has been understood since the pioneering works of Völmer and Weber [42, 43], Becker and Döring [44] and Gibbs [45]. The application

of classical nucleation theory for pore nucleation has been addressed in several reviews [46-52]. The theory for pore nucleation will be summarized here. For more details, the reader is referred to the references above.

The simplest case of pore formation is homogeneous nucleation in the absence any dissolved gas. Let us consider a pore nucleus with the external pressure, P_e, acting outside its surface. The external pressure will be the sum of the shrinkage pressure (P_s), the hydrostatic pressure due to depth (P_h), and the pressure applied to the surface of the liquid (P_{atm}). As a result, the amount of work (W) required to fracture the liquid to create a pore of volume V is equal to P_eV. There is, however, a surface energy barrier that needs to be overcome for the pore to be stable, which is equal to σA, where σ is the bulk surface energy per unit area (or tension) [53] and A is the surface area of the pore. The work to fill the pore with dissolved gas at internal pressure P_g is equal to $-P_gV$. The amount is negative because P_g helps the formation of the pore. Finally, the total work for the formation of the pore is:

$$W = \sigma A + V(P_e - P_g) \tag{3}$$

Assuming that pore nucleus is spherical and denoring (P_e-P_g) as ΔP, we have:

$$W = 4\pi r^2\sigma + \frac{4}{3}\pi r^3 \Delta P \tag{4}$$

The schematic plot showing the effect of the two contributions to W as a function of pore radius is presented in Figure 13. Note that the critical radius above which a pore is stable, r^* is found by:

$$r^* = \frac{-2\sigma}{\Delta P^*} \tag{5}$$

where ΔP^* is a negative number. Note that while surface energy for liquid metals is known, either ΔP^* or r^* need to be estimated or alternatively assumed. Before the theoretical values based on classical nucleation theory are calculated, first assumptions made in the literature are presented.
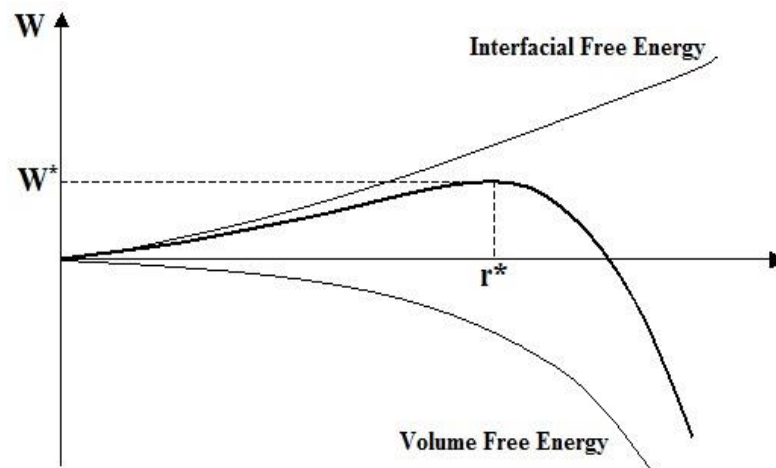
Figure 13. Schematic plot of total work for pore nucleation as a function of pore radius.

1.3. Assumptions for Modeling Pore Formation

Over recent decades, significant effort has been exerted to model pore formation during the solidification process to help foundry engineers design industrial casting processes. These efforts range from analytical models and criteria functions to complex computational simulations [54]. As indicated above, these models need to assume either the critical radius or required pressure for pore formation as a nucleation criterion. Some of the assumptions made for modeling pore nucleation are summarized in Table 1. Note that researchers assumed either that there is no nucleation barrier to pore nucleation or critical radius as a set quantity related to microstructure, to model industrial casting processes accurately. The assumption frequently made that there is no barrier to nucleation means that the surface energy barrier to be overcome is zero, i.e., no new surface is created during nucleation. Although this assumption has been shown to give accurate results for industrial processes, it is of course inconsistent with the principles of classical nucleation theory. This assumption is first compared to theoretical results based on classical nucleation theory.

Table 1. Assumptions made in literature for modeling pore nucleation.

Pore Nucleation criteria		Ref.	Notes on other assumptions
ΔP^*	r^*		
= 0	n/c [1]	[23]	
n/c	$\lambda_{DA}/2$	[55, 56]	
n/c	$\lambda_{DA}/2$	[57]	Minimum supersaturation required for pore nucleation
n/c	1 μm	[58]	
~0	n/c	[59]	Pores nucleate when the pressure in mushy zone is greater than the sum of the metallostatic head of the riser and the atmospheric pressure
n/c	n/c	[60]	Nucleation occurs when hydrogen supersaturation is higher than 0.1 cc/100g
n/c	n/c	[61-63]	Empirically fitted stochastic distribution of pores based on supersaturation
= 0	half of cell size (5 to 10μm)	[64, 65]	
n/c	= 10 μm	[66]	Pore nucleation is not considered
= 0	n/c	[67, 68]	Pores nucleate by gas supersaturation at heterogeneous nucleation site

1 Not Considered

Research Question 2: Are *in situ* observations and modeling assumptions consistent with the physics of pore nucleation?

2. Theoretical Background and Calculations of Fracture Pressure of Liquid Aluminum

2.1. Homogeneous nucleation

If a liquid is brought suddenly into a metastable state, by nucleation and growth processes, pores may appear spontaneously and a phase separation takes place. Steady-state theories [42-44] of nucleation consider growth of clusters from a supersaturated vapor of single molecules by a series of bimolecular reactions in which the clusters grow by addition of one molecule per reaction. The nucleation rate is then considered to be product of the concentration of critical nuclei and the frequency with which they grow by addition of one molecule. A basic quantity, describing the kinetics of this process, is the steady-state nucleation rate, J, which is expressed commonly as [42, 44, 50, 69]:

$$J = J_0 exp\left(-\frac{W^*}{kT}\right) \tag{6}$$

Although Equation 6 is universally accepted to be valid, the nucleation rate factor, J_0, has been interpreted differently among researchers. Fisher [53, 69] estimated J_0 from the theory of absolute reaction rates to be

$$J_0 = \frac{N_A kT}{h} exp\left(-\frac{\Delta G_0^*}{kT}\right) \tag{7}$$

Fisher stated that the rate of formation of bubbles of vapor in a mole of liquid subjected to a negative pressure P could be found by inserting Equation 7 into Equation 6:

$$J = \frac{N_A kT}{h} exp\left[\frac{-(\Delta G_0^* + W^*)}{kT}\right] \tag{4.a}$$

Fisher [53] then proceeded to introduce the fracture pressure of liquids, ΔP^*, based on the kinetics of phase transitions, as:

$$\Delta P^* = -\sqrt{\frac{16\pi\sigma^3}{3kT \ln\left(\frac{kN_A T}{h}\right)}} \qquad (8)$$

The fracture pressure equation by Fisher provided close estimates for acetic acid and benzene.

Other researchers also attempted to develop similar equations for fracture pressure of liquids. Bankoff [70] modified Fisher's equation by considering a superheated liquid:

$$\Delta P^* = -\frac{\rho_l}{\rho_l - \rho_g}\sqrt{\frac{16\pi\sigma^3}{3kT \ln\left(\frac{6kN_A^{2/3}T}{h}\right)}} \qquad (9)$$

Bernath [71] calculated ΔP^* by considering the frequency of nucleus formation which is a function of the molecular latent heat of vaporization, resulting in a cavity into which molecules may or may not vaporize:

$$\Delta P^* = -\sqrt{\frac{\frac{9.06\sigma^3}{kT}}{\ln\left(\frac{1.45\rho N_A^2 \sigma^2}{\Delta P^* M^{3/2}\sqrt{kN_A T}}\right) - \frac{H_v}{kT}}} \qquad (10)$$

The fracture pressure for homogeneous pore nucleation in pure aluminum at melting temperature and the corresponding critical radius (r*) values calculated Equations 8-10 as well as Equation 5 are presented in Table 2. The surface energy of liquid aluminum at melting temperature was taken as 0.914 J/m^2 [72]. Note that these values are for liquid aluminum without dissolved gas or curvature effects. These assumptions will be revisited below.

Table 2. Fracture pressure, critical size of a nucleation pore, number of vacancies in the cluster and the probability of formation of that vacancy cluster calculated for pure solidifying aluminum without dissolved gases or curvature effects.

Equation	ΔP^*(GPa)	r* (nm)	n_v*	$P_F(n_V^*)$
Fisher	-3.41	0.535	39	2.30×10^{-115}
Bankoff	-3.81	0.478	28	3.56×10^{-94}
Bernath	-2.35	0.765	160	6.12×10^{-246}

Note that all equations give critical pore size results that are several orders of magnitude smaller than r* assumed for modeling, Table 1. Moreover, while pressure assumed for pore nucleation is consistently around zero in Table 1, calculated fracture pressures are several gigaPascals. These theoretical values are 3 to 4 orders of magnitude higher than experimental tensile strength values reported in the literature (~1 MPa) for aluminum alloys at melting temperatures [56, 57]. Hence, there is a significant discrepancy between the theoretical values and those assumed to have models that accurately predict pore formation. Moreover, it can be concluded that homogeneous nucleation of a pore in solidifying aluminum is impossible.

It is noteworthy in Table 2 that Fisher and Bankoff equations yielded very similar results and the Bernath equation gave a slightly lower value. The Bernath equation has been shown [73] to be accurate for a number of liquids at room temperature. Moreover, the fracture pressure of liquid lead was investigated [74, 75] via molecular dynamics. Fracture pressure results were in the order of estimates provided by three equations [76]. In addition, in an independent study, Martynyuk [77] used the modified Van der Walls equation to calculate the ideal tensile strength of metals, including aluminum, at melting temperature. Martynyuk found the ideal tensile strength of isotropic aluminum at melting temperature to be 4.80 GPa, which is closer to the values calculated by the Bankoff and Fisher equations for liquid aluminum at the same temperature. Hence, there is evidence in the literature supporting the accuracy of the level of theoretical fracture pressure for liquid aluminum.

In the absence of dissolved gas, the only mechanism available for a pore to nucleate is the formation of a vacancy cluster with a radius equal to r*, because of the supersaturation of vacancies created during the solidification process [78, 79]. The number of vacancies in the cluster with the critical pore size, n*, is found by:

$$n_v^* = C_{AP} \left(\frac{r^*}{r_A}\right)^3 \qquad (11)$$

C_{AP} is 0.74 for aluminum because of its face-centered cubic (FCC) crystal structure. Number of vacancies in the cluster with the critical pore size was calculated by inserting r* in Equation 11. The number of vacancies needed in a vacancy cluster to form a pore with the critical size were calculated for the three fracture pressure equations. The results are presented in Table 2, which show that large vacancy clusters are needed for fracture, i.e., pore formation.

Brooks [80] derived an equation for the concentration, i.e., probability of vacancy clusters with n_v vacancies, $P_F(n_V)$ as:

$$P_F(n_V) = \left[c_v exp\left(\frac{E_V - (E_n/n_v)}{kT} \right) \right]^{n_v} \tag{12}$$

Jackson [81] calculated the formation energy of a vacancy (E_V) and spherical cluster of vacancy (E_n) as:

$$E_V = 12\sqrt{2}r_v{}^2\sigma \tag{13}$$

$$E_n = 15.36n^{2/3}r_v{}^2\sigma \tag{14}$$

Thomas and Willens [82, 83] conducted experiments to determine the vacancy concentration in liquid high purity aluminum (99.996% Al) by quenching from the liquid state. In these experiments, vacancies formed dislocation loops instead of voids, as also observed by Kuhlmann-Wilsdorf and Wilsdorf [84]. The change in vacancy concentration (c_v) in aluminum in liquid and solid states with temperature is presented in Figure 14. At the melting point of aluminum, the equilibrium vacancy concentration is approximately 0.001, which has been used as an approximation for all metals [78].
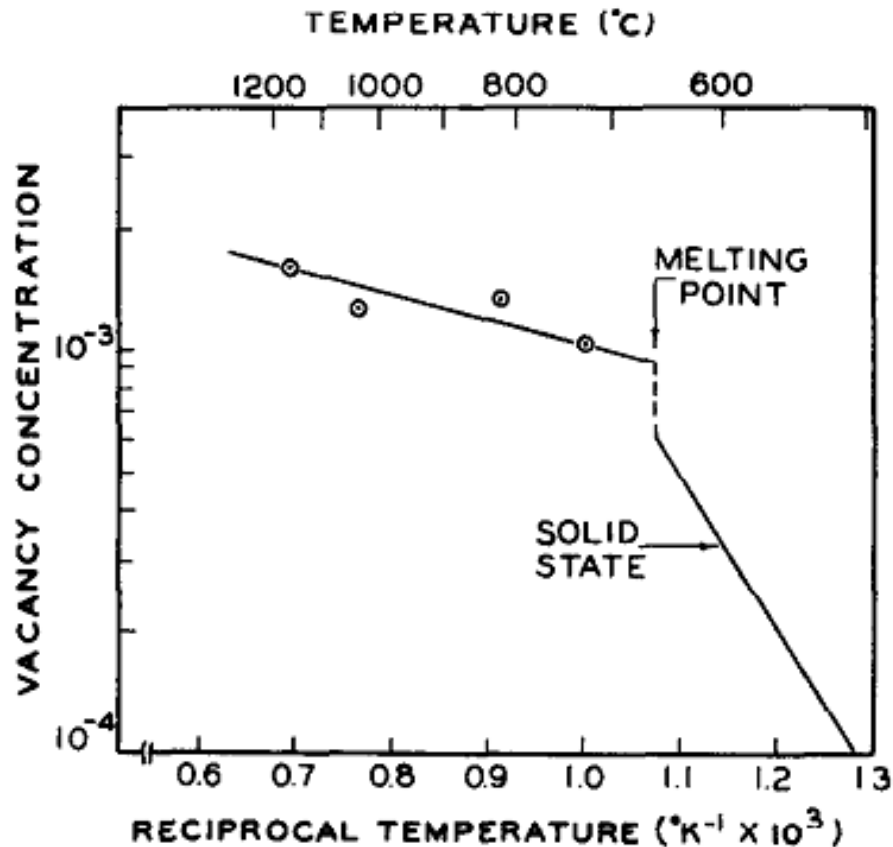
Figure 14. Relationship between vacancy concentration and temperature [85].

By taking the radius of a vacancy in aluminum as 0.158 nm [86], the equilibrium

vacancy concentration at melting temperature to be 10^{-3}, the probability of a vacancy cluster

with the size of a critical pore was calculated for the three fracture pressure equations by using

Equations 12-14. The results are also presented in Table 2. These results are extremely low

probabilities, which leads to reaffirmation of the conclusion that homogenous nucleation of

pores in pure aluminum without dissolved H is not possible.

2.1.1. Effect of curvature on surface energy

In large vacancy clusters, the surface energy is simply the product of surface area and bulk

surface energy as introduced in Equation 4 [81]. However as the vacancy cluster gets smaller

in size, curvature effect will become increasingly more pronounced and will have a surface

energy significantly less than a flat surface [84, 87], especially if the number of vacancies in

the cluster is less than 40 [88]. In the limit, if the radius of curvature of the surface is zero there

is no surface, so the surface energy is zero. Si-Ahmed and Wolfer [89] showed that the effect

of curvature on surface energy to form a vacancy cluster can described as

$$W_s = 4\pi r^2 \sigma \left[1 - \frac{0.8}{n_v + 2} \right] \qquad (15)$$

Hence effective surface energy can be written as:

$$\sigma_{eff} = \sigma \left[1 - \frac{0.8}{n_v + 2} \right] \qquad (16)$$

Subsequently, the critical pore size can calculated by effective surface energy into Equation 5,

in both numerator and denominator. The results presented in Table 3 show that curvature

effects reduces fracture pressure values slightly but have essentially no effect on the critical

pore size. Therefore, the conclusion that homogenous nucleation of pores in aluminum during

solidification is impossible remains unchanged. This conclusion is consistent with the

theoretical calculations of Zinkle et al. [79] who showed that pores were not favored in

aluminum, and even if they form, they collapse into more stable, fully condensed, forms, such

as loops and stacking-fault tetrahedrons.

Table 3. Fracture pressure, critical radius and vacancy cluster size recalculated by taking
curvature effects into account.

Equations	ΔP*(GPa)	r* (nm)	n*
Fisher	-3.31	0.539	40
Bankoff	-3.66	0.484	29
Bernath	-2.35	0.776	160

2.1.2. The Effect of Dissolved Gas

The effect of gases dissolved in liquid metal on pore formation can be considered in two ways;

(i) affecting stability of pores by changing the surface energy of solidifying metal, and (ii)

increasing internal pressure in liquid. These aspect will be addressed in this section for liquid aluminum.

Hydrogen is the only gas with any significant solubility in liquid aluminum. The solubility of hydrogen is approximately 7 mL/kg in liquid and 0.4 mL/kg in solid state at melting temperature [90]. It is often speculated in the literature that the large difference in the solubility of H in liquid and solid states is the main reason for porosity in aluminum castings. The 7mL/kg equilibrium concentration of hydrogen in liquid aluminum at melting temperature corresponds to approximately 1 atomic part per million (appm) [91] which is three orders of magnitude lower than that of vacancies. Hence, formation of vacancy clusters is still the required nucleation mechanism for pores, with dissolved gas only increasing the stability of pores and driving their growth [92].

As stated in the last section, theoretical calculations showed that pores are metastable in aluminum, although several researchers [93-97] reported observing pores in pure aluminum samples quenched from high temperatures (~1000 K) at high cooling rates (~10^4 K/s). It was speculated [79] that impurity atoms such as dissolved hydrogen can increase the stability of pores and therefore pores do not collapse to form loops or stacking-fault tetrahedrons. Obviously, the high cooling rates used in these studies are much higher than the ones in castings, and therefore results obtained from thin films cannot be directly applied to aluminum castings.

There is evidence provided in the literature [92, 98-104] that suggest that surface energy can be reduced as much as 50% by the presence of dissolved gasses. To determine what the effect of such a reduction would be, surface energy with dissolved gas, σ_g, was changed systematically from 0.914 J/m^2, the bulk surface energy of liquid aluminum, to 50% of that value. Fracture pressure, critical pore size and number of vacancies in the initial cluster were calculated by using Equations 8, 5 and 11, respectively. Results, indicated with subscripts "g"

were normalized by taking ratios of calculations in the presence of gas to those without dissolved gas. The effect of reduction in surface energy on fracture pressure, critical pore size and number of vacancies are presented in Figure 15. Although a decrease in surface energy should reduce the fracture pressure, the final result will be a larger critical pore size, and consequently a higher number of vacancies in the cluster and a lower probability of its formation. Therefore, any reduction in surface energy due to dissolved gas, such as hydrogen in aluminum, only serves to make homogeneous nucleation more difficult.
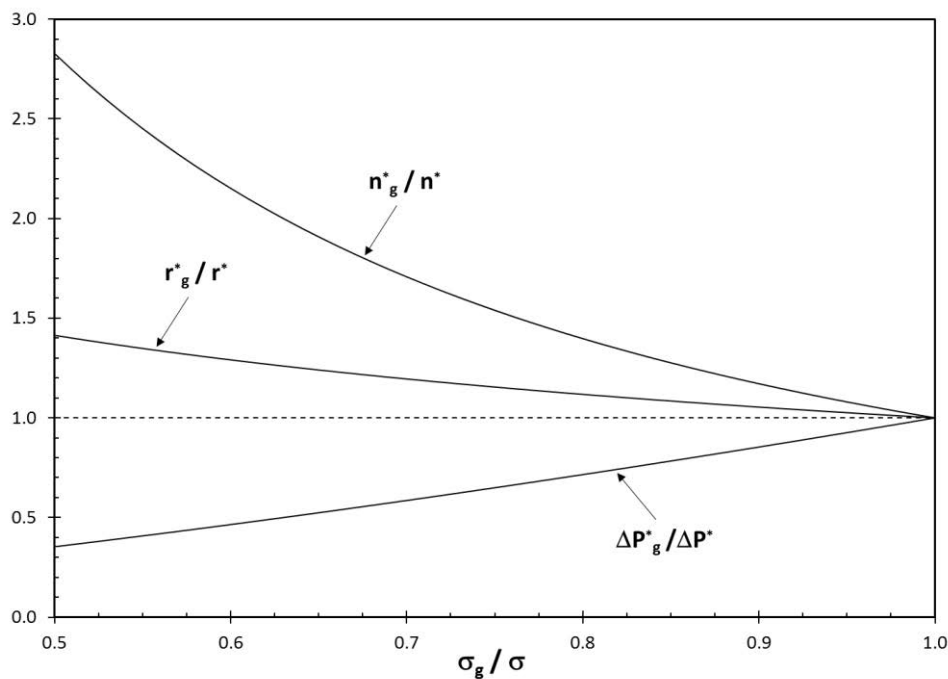
Figure 15. The effect of change in surface energy on fracture pressure, critical pore size and number of vacancies needed for the pore to be stable.

The second effect of dissolved hydrogen stated widely in the literature is its effect on the overall pressure, based on the assumption that aluminum goes from equilibrium solubility in liquid to solubility in solid instantaneously upon freezing. It is assumed that pressure build-up from rejected hydrogen atoms will add to the hydrostatic pressure of contraction to be sufficient to nucleate a pore [4, 105]. Thus, the pore will nucleate when the effective pressure

exceeds the fracture pressure of the liquid, followed by rapid growth of the pore, as observed in in situ experiments outlined above.

Because the solubility of hydrogen in liquid aluminum is approximately 20 times that in solid at melting temperature, excess hydrogen is expected to build up in intercellular and interdendritic channels. Piwonka and Flemings [23] hypothesized that this supersaturation can be as high as 100 times the solubility of hydrogen in liquid. To test the hypothesis of Piwonka and Flemings, the *in situ* experiments by Murphy et al. [39] were revisited. The vicinity of the first pore, designated as P_1, in Figure 11 at t = 84s is presented again in Figure 16.a. The area designated by the box between the two cells between where the pore forms later is taken as the control volume. In Figure 16.b, the digital version of the box is presented with solid indicated in black and liquid in white. Digital image analysis showed that the local solid fraction is 0.434. By using the equilibrium solubility of hydrogen in liquid and solid provided above, the concentration of hydrogen in the liquid between the two cells can be estimated to be 1.73 times the equilibrium amount. Consequently, based on Sievert's law, the partial pressure of hydrogen can be calculated as 3 atmosphere or 3×10^{-4} GPa, which is four orders of magnitude less than the fracture pressure. Moreover, it is visible in Figure 11 that the pore that forms pushes the cells as it expands. Therefore, there is no physical constraint in the area where the pore forms. Based on these results, it can be concluded that the pore in Figure 11 did not nucleate homogeneously due to increased pressure from hydrogen supersaturation.

(a)   (b)
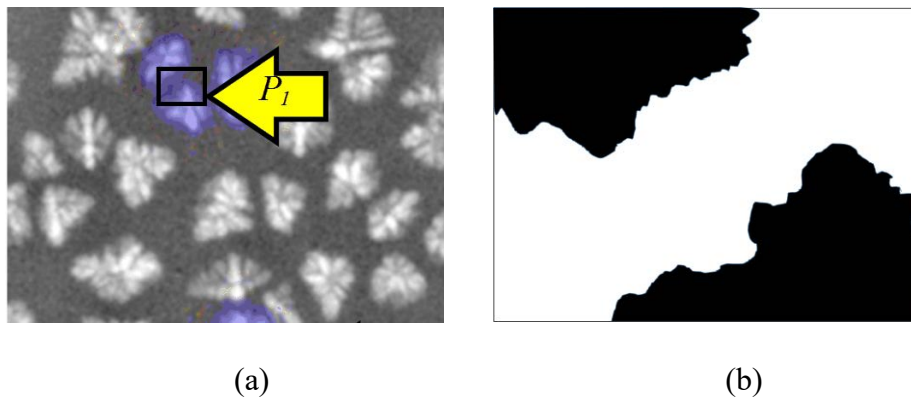
Figure 16. (a) The vicinity of the first pore in experiments by Murphy et al. [39] and (b) the digital version for image analysis of the area in the box.

The discussion presented in this section clearly demonstrates that homogeneous nucleation of pores in aluminum solidifying at rates common in industrial castings is impossible. In the next section, heterogeneous nucleation will be addressed.

2.2. Heterogeneous nucleation

In this section, whether pore nucleation is possible on certain types of preexisting solid surfaces which are poorly wetted such as non-metallic inclusions will be discussed. Fisher [53] studied heterogeneous nucleation of a pore at the interface between a solid substrate and a liquid by assuming a shape bounded by a plane and a portion of a spherical surface, as presented in Figure 17.a, where σ_{LP}, σ_{PO} and σ_{LO} represent the liquid-pore, solid-pore and solid-liquid surface tensions, respectively. Fisher showed that the fracture pressure at the interface where the pore has an angle θ with the solid substrate, is reduced by a factor:

$$\frac{\Delta P_{het}^*}{\Delta P_{hom}^*} = \sqrt{\frac{(2 - \cos\theta)(1 + \cos\theta)^2}{4}} \qquad (17)$$

As θ approaches 180°, i.e., perfect non-wetting substrate, the fracture pressure of heterogeneous nucleation goes to zero. However, $\theta \rightarrow 180°$ is unrealistic and according to Campbell [4], the maximum contact angle attainable is approximately 160°. At $\theta = 160°$, Equation 17 yields 0.05. Therefore the fracture pressure for heterogeneous nucleation in liquid aluminum falls between

-191 and -118 MPa. These values are still much higher than the ones assumed in the literature and the tensile strength of pure aluminum and aluminum alloys reported at melting temperature.

a   b
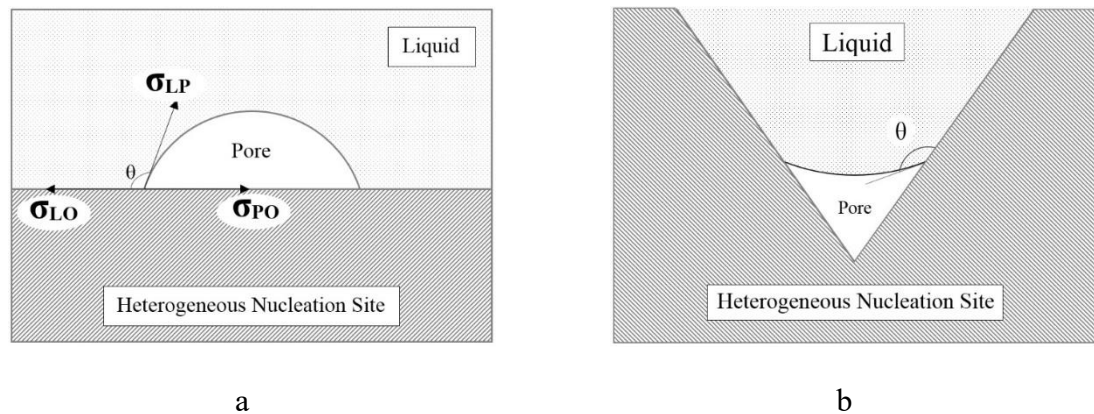
Figure 17. Heterogeneous nucleation of a pore at various interfaces: (a) on a plane surface, (b) on concave substrate.

Chalmers [106] stated that the work of formation of an embryonic pore is reduced on a concave substrate, and Fisher [53] speculated that it may become zero for perfectly sharp notches. Hence, pore nucleation in a perfectly sharp notch corresponds to the nucleation of a crack in the solid inclusion. There are good reasons for believing that, similarly to the nucleation of pores in liquids not being possible, the nucleation of cracks in solids is also impossible [107]. Bankoff [70] considered the growth and emergence of the embryo from re-entrant angles. Although nucleation may occur easily at the root of the notch, the growth of the resulting pore will be arrested at the notch entrance because the pore radius must exceed the critical size with respect to the bulk of the liquid. Based on this, although an inclusion may increase the probability of pore nucleation, it is not possible to attribute the pores in aluminum castings to heterogeneous pore nucleation. Therefore nucleation of pores in solidifying aluminum, either homogeneously or heterogeneously, is impossible.

3. Reconciliation of Observations, Calculations and Assumptions

If pores cannot nucleate in liquid aluminum either homogeneously or heterogeneously, how can the prevalence of pores in aluminum castings be explained? Although pores cannot nucleate in liquid aluminum, there is a mechanism by which pores can grow, without nucleation. This mechanism is based on the bifilm theory, which is first outlined.

3.1. Bifilm Theory

Although the molten aluminum can actually benefit from oxide skin due to the protective nature of the alumina which is created on the surface, prevent to continue the oxidation into the melt. The problem begins only when the surface oxide film is submerged due to an external or internal force and the film has to fold over itself while it is entrained into the bulk liquid. Since the film has grown from the melt, the underside is in atomic contact but the top surface will be crystalline. After entrainment, the two oxide surfaces will have contact without any bonding between them. The entrainment process is shown schematically in Figure 18.
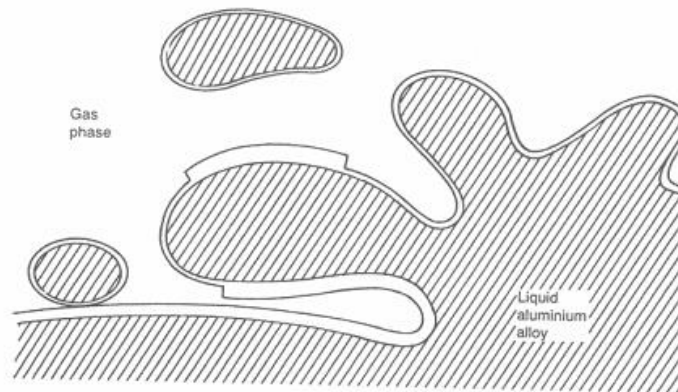
Figure 18. Surface turbulence and entrainment of surface oxide films [4].

Surface turbulence is the chaotic breaking up of the surface of the liquid, which allows the surface oxide film to entrain in the melt. Surface turbulence is different from bulk turbulence which can be assessed by the Reynolds number. Although it is possible to prevent surface

turbulence in liquid metal during pouring, avoidance of bulk turbulence is almost impossible [108]. Clearly only surface turbulence is of concern here.

Campbell [108] introduced when liquid metal is restrained with pressure of $2\gamma/r$ and it has velocity V and density ρ, the inertial pressure against the surface is equal to ρV^2, as presented in Figure 19. If V exceeds a critical value the inertial pressure will motivate the surface to form a droplet with radius of approximately r. So the critical velocity to break the surface can calculated by

$$V = \sqrt[4]{4\frac{g\sigma}{\rho}} \qquad (18)$$

Campbell [108] also stated the fourth power relation demonstrates all metals practically have the same critical velocity; which is close to 0.35 to 0.5 m/s for all liquid metals.
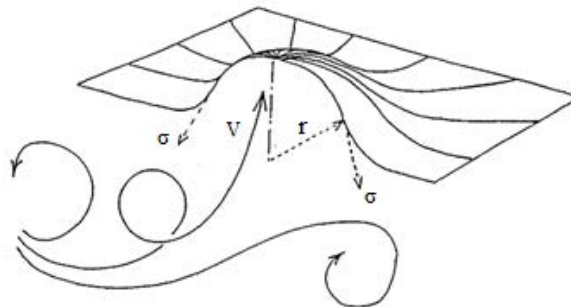
Figure 19. The balance of inertial and surface tension pressure at the surface of the liquid [108].

Runyoro et al. [109] investigated how the bending strength of pure aluminum bars changed with increasing gate (filling) velocity. The results shown in Figure 20 clearly suggest a sudden drop as the critical velocity of 0.5 m/s is exceeded. Under gravity, a fall of only 12 mm is required to reach this velocity. The step function appearance is curious; if the entrainment

effect, i.e., crack size, can be expected to get larger with velocity, the results showing a step function is not entirely consistent with fracture mechanics principles.
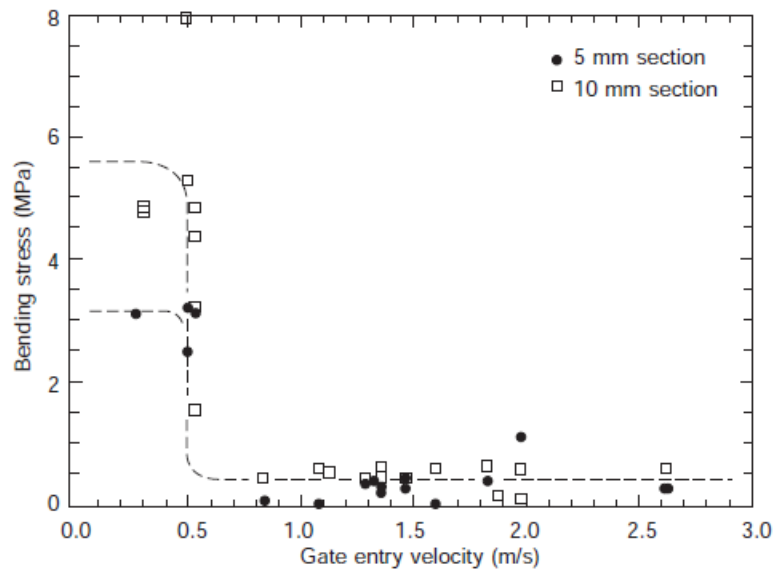
Figure 20. Bending strength of 5 and 10 mm plate castings in aluminum castings as a function of metal entry velocity into the mold [109].

Research Question 3: Is the damage to liquid aluminum by entrainment a step function?

Bifilm defects are usually too thin to detect via nondestructive tests but they have been observed on micrographs and fracture surfaces. Divandari [110] captured a polished section of a cast aluminum alloy breaking into a tangled bifilm, presented in Figure 21. Recently, the scanning electron microscope (SEM) has detected much more detail of bifilms. A bifilm, found by Green and Campbell [5] on the fracture surface of an Al–7Si–0.4Mg alloy casting is shown in Figure 22. The composition was confirmed by microanalysis to be alumina and the thickness of the thinnest part appeared to be close to 20 nm [4], which suggest that the film formed during mold filling. Because the thickness of the newly formed (or "young") oxide films is so low, Campbell [108] referred to these defects as "invisible macrodefects".

Research Question 4: Are bifilms still invisible?
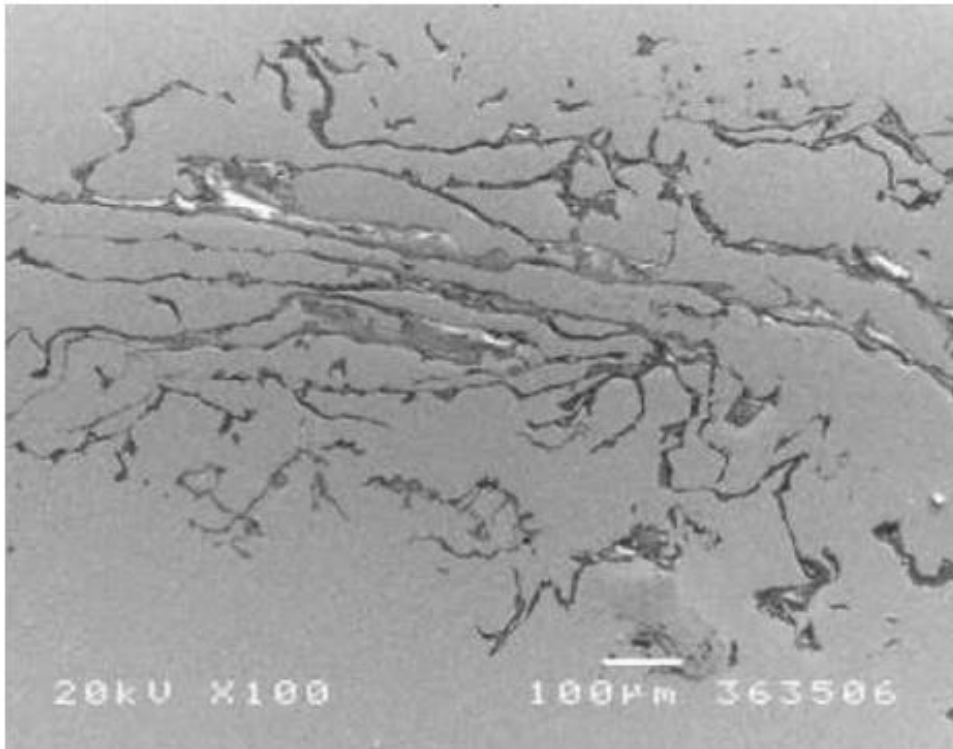
Figure 21 Polished surface of Al–7Si–0.4Mg alloy breaking into a bifilm, showing upper part of the double film removed, revealing the inside of the lower film [110].
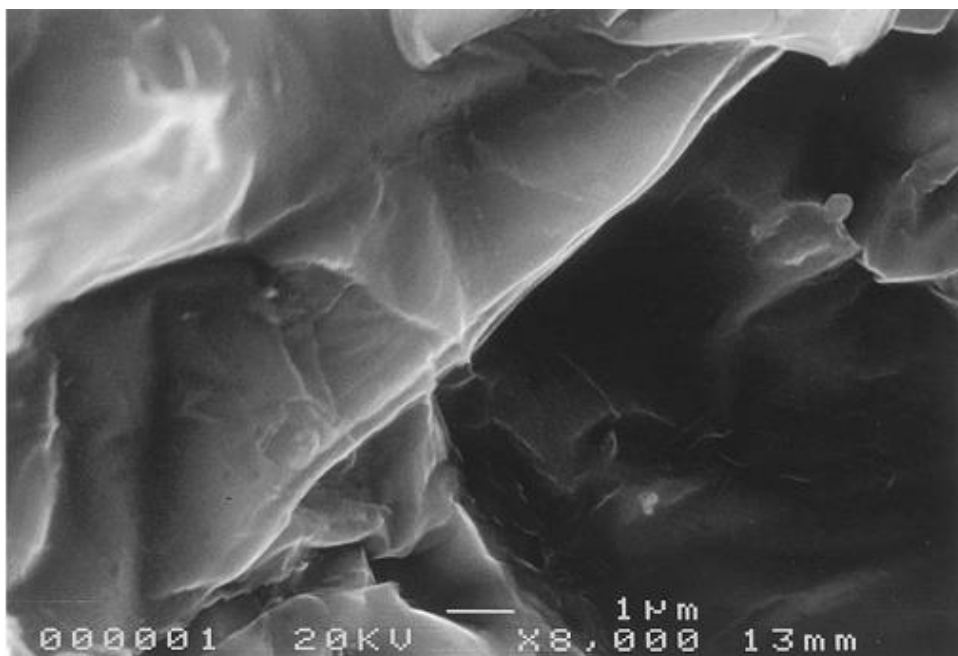
Figure 22. A bifilm on the fracture surface of an Al–7Si–0.4Mg alloy casting [5].

Another way to determine bifilms presence is use of the reduced pressure test (RPT) for aluminum alloys. The popularity of the RPT as currently widely used in the industry lies in the relative simplicity and inexpensive nature of the test. The technique is also known, with slight variations in operating procedure, as the Straube-Pfeiffer vacuum solidification test (Germany), Foseco Porotec test (UK), and IDECO test (Germany) [4]. RPT test has been designed to demonstrate the porosity potential of the melt by providing the required conditions for the effective control of porosity with both entrained inclusions and hydrogen content. During the test, a sample of liquid aluminum is allowed to solidify in vacuum (under reduced pressure). The reduction of pressure magnifies the effect of dissolved gas on the opening up of bifilms. The bifilms are normally difficult or impossible to see by X-ray radiography and to the unaided eye on a polished section when solidified under one atmosphere pressure. One primary disadvantage of RPT machine is that results are not quantitative. Nevertheless, it becomes possible to identify the size, shape, type and distribution of non-metallic inclusions in the final product which can be seen on a polished cross section of the reduced pressure test [2].

The Reconciliation

Campbell [4] stated that the entrainment of the surface oxides to form double parallel oxide films (bifilms) may act as initiation sites and subsequently, they can easily open up by pressure of dissolved gas. This point is supported by the findings of Fox and Campbell [111] who conducted an experiment in which a reduced pressure test sample was observed via real time x-ray radiography under different pressure levels. Two radiographs taken at a pressure of 1.0 and 0.01 atmosphere during this experiment are presented in Figure 23. At 1.0 atm, there are no visible pores, however, there are numerous dark patches. When pressure is reduced, the dark patches, which are bifilms in their compact, convoluted state, open up under the expansion of entrained air (residual gases, hydrogen and argon) between the two layers of the oxide. Hence pores form without any nucleation, and only through growth of the bifilms, at only

modest reduced pressures of almost 1 atm, consistent with the assumptions for fracture pressure levels presented in Table 1. Bifilms could ravel into small compact features by the internal turbulence created in the melt. As a result, their size could be reduced approximately 10 times from their original size. In this form, they are usually relatively harmless [112]. However, during solidification, they could unravel back to their original starting shape to form a planar crack as a result of hydrogen diffusion and/or solidification shrinkage.

(a)   (b)
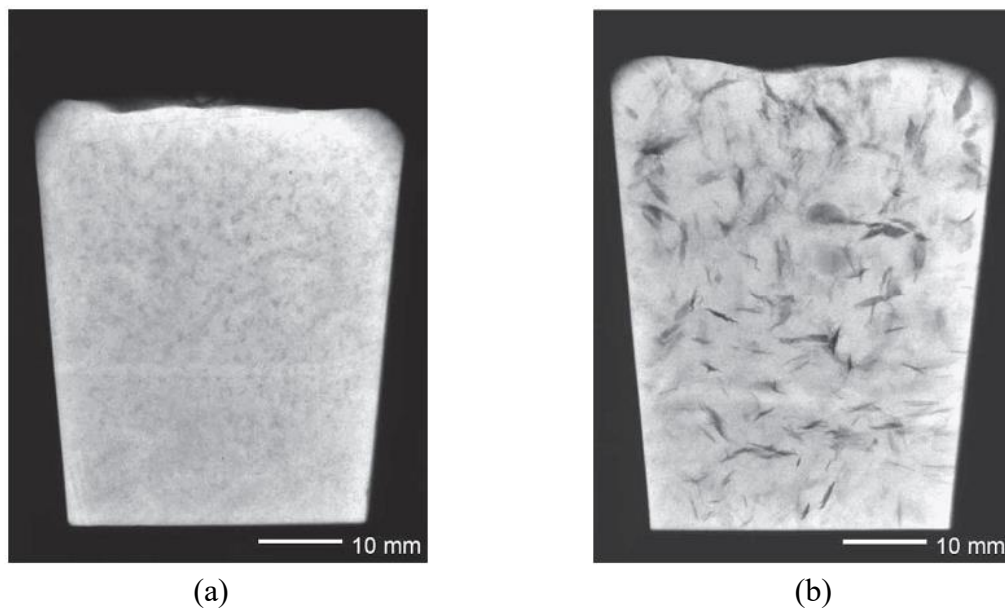
Figure 23. Radiographs of reduced pressure test samples of the same as-melted Al–7Si–0.4Mg alloy solidified; (a) Under pressure of 1 atm, (b) Under pressure of 0.01 atm [111].

Similarly, the *in-situ* observations summarized previously show growth of pores, even when the bulk and local solid fractions are well below the levels required for pore nucleation. For pores to form under such conditions, where nucleation is impossible, the only viable mechanism is the opening up of folded-over films entrained by turbulence (bifilms). This mechanism is shown schematically in Figure 24.
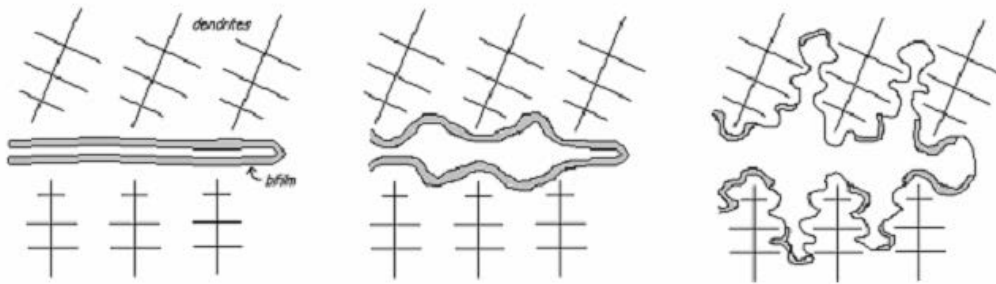
Figure 24. The opening of bifilms and porosity formation [4].

Hence the presence of bifilms entrained is the sole mechanism underlying pore formation. In the presence of bifilms, nucleation is completely bypassed because fracture of the liquid under pressure is no longer needed due to the crack-like nature of bifilms. To the author's knowledge, this effect of bifilms, i.e., bypassing nucleation, has not been highlighted previously. This explanation is in complete agreement with the *in situ* observations, as well as the pressure assumptions presented in Table 1. The initial growth of pores in relatively large, enveloping bifilms might display a series of spherical forms if the bifilm is mechanically weak as a result of its thinness. In contrast, irregular forms may result because of the mechanical constraint of thicker, more rigid bifilms. However, if bifilms are much smaller in size, as would be expected from fresh, "young" oxides that become "chopped" during mold filling, it is conceivable that a pore would initially form by opening the bifilm, but then grow beyond the size of the bifilm as a substantially sphere expanding freely in the liquid, as also observed during in situ experiments. The presence of oxides on the walls of pores has been confirmed recently [5, 113-115]. However, bifilms between pores or away from the pores have not been reported on micrograph, to the author's knowledge.

Research Question 5: Can bifilms be observed away from pores on micrographs?

If nucleation of pores is not possible, one may ask how the hydrogen rejected from solidifying aluminum would be accommodated in the absence of oxide films. It is well known that hydrogen and vacancies have a high binding energy [116-118] and a vacancy in aluminum is capable to trapping up to twelve hydrogen atoms [119]. Therefore hydrogen supersaturation, assumed in the literature to drive pore nucleation upon solidification of aluminum can be easily accommodated by the solid equilibrium vacancy concentration, shown in Figure 14. Hence, the assumption usually made in the literature that hydrogen necessarily precipitates during solidification, because of the abrupt change in hydrogen solubility, is not well founded.

With the insights provided in this study, we can turn our attention back to certain points raised earlier in the paper;

1. The final shape of the pores does not necessarily indicate the root cause of pore initiation. In Figure 1, the presence or otherwise of dendrites merely indicates the timing of the growth of the pore; if early, it will be round, whether pore growth is driven by shrinkage or gas because the pore will grow freely in the liquid. However if the pore forms late during solidification, it will exhibit cusps (again, whether shrinkage or gas driven) as a result of impingement on surrounding dendrites. Examples are provided in Ref. [4], in Figures 7.46 and 7.47, which show subsurface pores around a core. All pores are in the same hydrogen diffusion field from the reaction with the core binder, but adjacent pores are dendritic or round randomly. It is because of very different ease of unfurling of randomly furled bifilms.

2. Note in Figure 12 that some pores smaller than 1 mm are not spherical. Pores smaller than about 1 mm diameter become increasingly like spherical bullets as their size diminishes; they become mechanically very hard and undeformable as a result of their diminishing radius of curvature. Thus all small pores should be expected to be perfectly round. If not, some important factor must be influencing

their shape. Consequently, pores in Figure 12 can be attributed to bifilms opening during the last stages of solidification. Pores may be forming on raveled bifilms, in which case part of the bifilm will open easily and quickly, and therefore likely to create a small spherical pore, but the remainder of the bifilm only unfurls slowly, to form a fairly linear pore, or fairly linear array of small pores. The evidence for such a process has been presented by Tynelius and Major [120] as a combination of the dendrite arm spacing (i.e., local solidification time) and hydrogen content, as presented in Figure 25.a. Tylenius and Major indicated that they could not explain their results. The explanation was provided later by Campbell [121], as presented in Figure 25.b. The degree of unfurling of the bifilm is determined by the drive for growth, i.e., gas content and local solidification time (as determined by dendrite arm spacing), the latter of which can be also taken as an indication of negative pressure due to shrinkage of the metal around an internal pore.

3. The assumptions made in pore formation models in aluminum castings, summarized in Table 1, were coupled with growth and solidification equations to give good results compared to experimental data. These assumptions for pore nucleation, i.e., fracture pressure (~0.1 MPa) and critical pore size (~$\lambda_{DA}/2$), can only be valid if the bifilm theory is applied, which states that there are preexisting unbonded surfaces, i.e., bifilms, already in the liquid metal.

4. Bifilms are extrinsic defects that form due to entrainment of surface oxide films. Consequently, the statements made in the literature that pores in castings are intrinsic are not accurate.
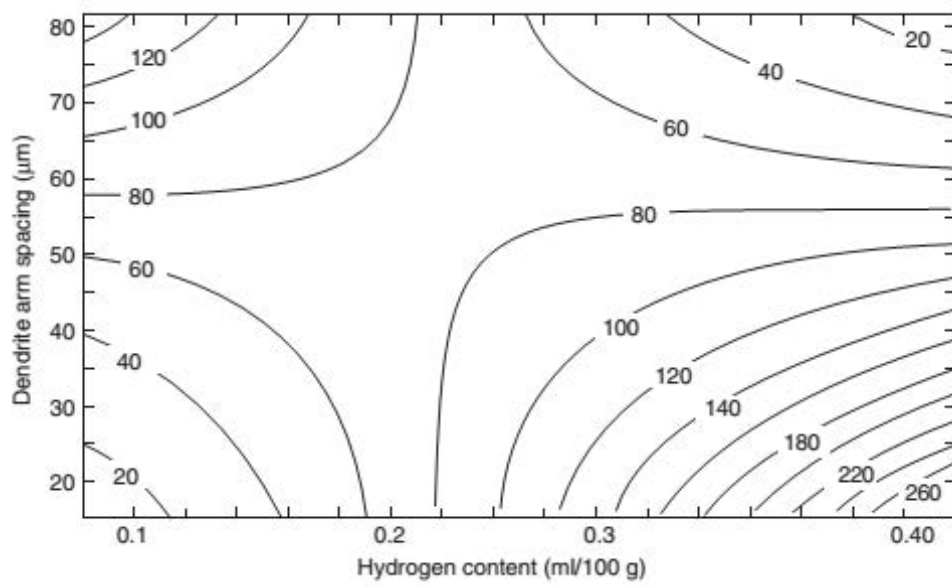
(a)
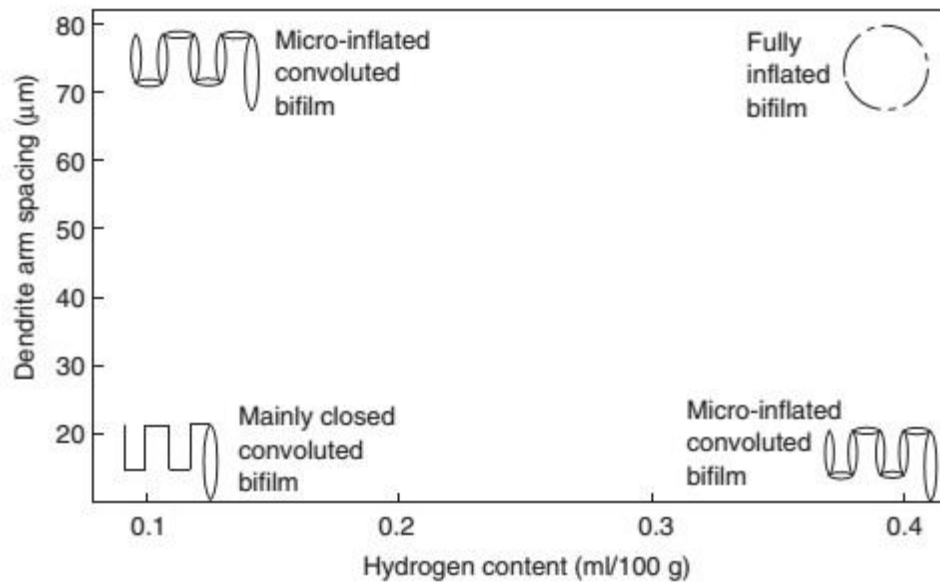
(b)

Figure 25. (a) Experimental results by Tynelius et al. presenting the relationship between hydrogen content and solidification time (assessed as DAS), (b) Campbell interpretation by a bifilm model.

4. Experimental Procedure

4.1. Alloy and Melting Procedure

In this study, a high quality, continuously cast A356 alloy ingots were used. The composition is given in Table 4. The alloy has a liquidus temperature of 613°C. The experiments with the reduced pressure test were conducted to study of the effect of pouring conditions on the pore size distribution. The first concern was to run an experiment with special attention to reduce turbulence during pouring. To perform an experiment approximately 0.5kg of alloy was melted in a graphite crucible in an electric resistance furnace at 650°C. To eliminate entrainment of any surface oxides, ingot was first cut into pieces, which were later machined to cylinders with the size of the crucible. This technique has not been used in any other study, to the author's knowledge.

Table 4. Chemical compositions and melting point of aluminum alloys A356.0

	Si	Fe	Cu	Mn	Mg	Zn	Ti	Al	T_m
AA 356.0	6.5-7.5	0.6	0.25	0.35	0.20-0.45	0.35	0.25	Remainder	$613^{\circ C}$

4.2. Reduced Pressure Test (RPT)

Sample collection for RPT was started when the whole charge was in liquid state. Four RPT samples were collected by various pouring conditions in steel mold and solidified under vacuum pressure of 0.2 atm; one without pouring which machined in the same size and shape of steel mold (sample A), two with 25mm pouring height (samples B & C), one with 150mm pouring height (sample D), and. The picture and dimension of the RPT steel mold is given in Figure 26. The RPT machine available in the School of Engineering laboratories, pictured in Figure 27, was used.

(a)   (b)

Figure 26. RPT steel mold: (a) picture and (b) drawing.

Figure 27. Reduced pressure test machine used in this study.

4.3. μ-CT Imaging

Each sample was analyzed to investigate pore size and location distribution by Shimadzu inspeXio SMX-225CT Microfocus X-Ray CT System (Figure 28).

Figure 28. Shimadzu inspeXio SMX-225CT Microfocus X-Ray CT System.

4.4. Microscopy and Microanalysis

After porosity investigation with X-ray CT machine, samples were sectioned (cut by a saw longitudinally into halves), ground with 80, 240, 1200 and 2400 grade papers, and polished by 5μm diamond polishing paste. The sectioned reduced pressure test samples were investigated with a TESCAN Vega3 scanning electron microscope. The X-ray detector is part of an Oxford Energy Dispersive Spectrometer (EDS) system which was used for the semi quantitative X-ray analysis of the local composition of the alloy.

5. Results and Discussions

This chapter represents the primary results and discussions of the effect of pouring conditions on pore size distribution and bifilms assessment. Detailed X-ray CT pictures, pore size distribution, SEM images, all included in this chapter.

5.1. X-ray CT analysis

3D image of RPT samples were captured by X-ray CT machine as one of them is shown in Figure 29.
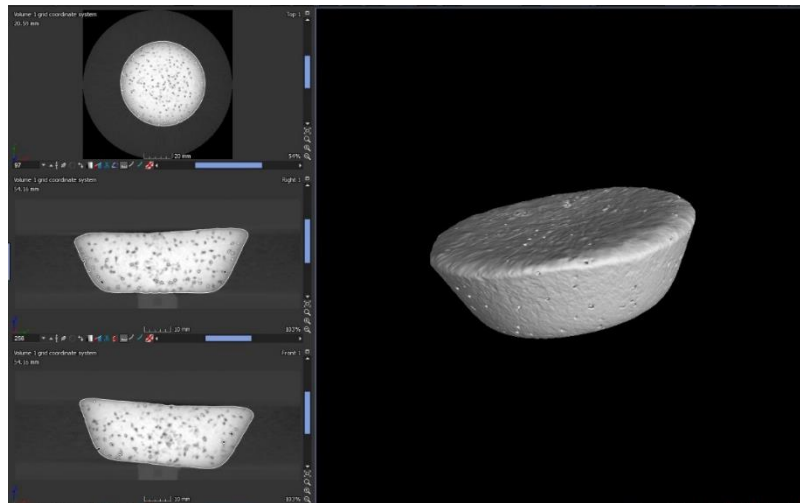
Figure 29. 3D image of sample D.

After that all images were analyzed with porosity analysis module at myVGL 3.0 software. The summary of results is presented in Table 5. Equivalent radius, r_{eq}, indicates the radius of the circumscribed sphere of the defect.

Table 5. X-ray CT scan measurements of pores in RPT samples of A356 alloy.

Sample	h_d (mm)	Sample Volume (mm^3)	Total Pore Volume (mm^3)	Number of pores	f_V (%)	N_P (mm^{-3})	Average Volume (mm^3)	Average r_{eq} (mm)
A	0	54657	986	734	1.80	0.0134	1.14	0.648
B	25	53466	2598	961	4.86	0.0180	2.74	0.868
C	25	68883	3879	1146	5.63	0.0166	3.83	0.971
D	150	59683	3953	2036	6.62	0.0341	1.89	0.767

The CT scans of samples A through D are shown in Figure 30-Figure 37.
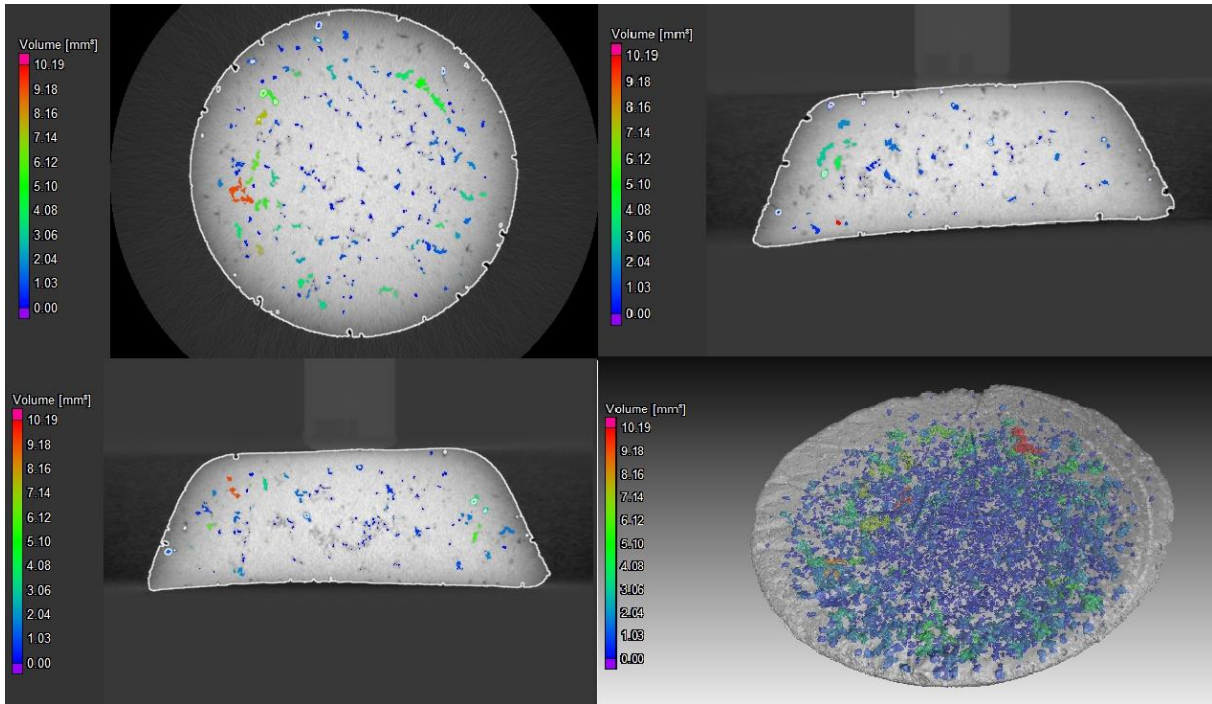
Figure 30. X-ray CT image after porosity analysis sample A

Figure 31. Largest pore in sample A with 10.19 mm^3 volume
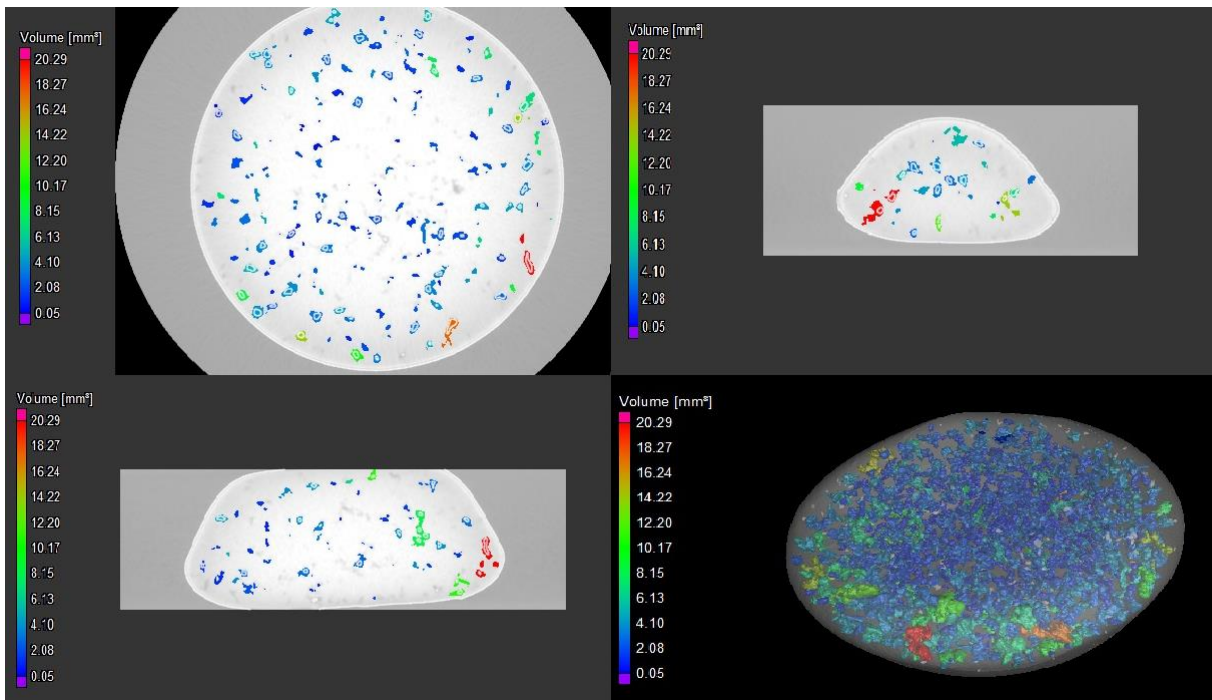
Figure 32. X-ray CT image after Porosity analysis sample B
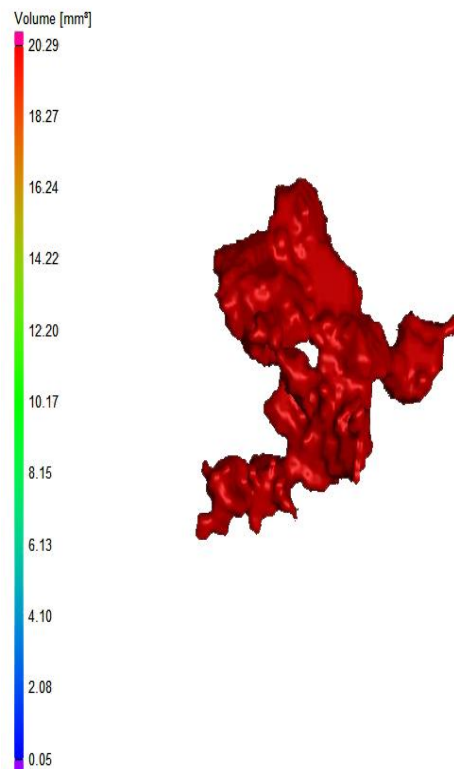
Figure 33. Largest pore in sample B with 10.19 mm^3 volume
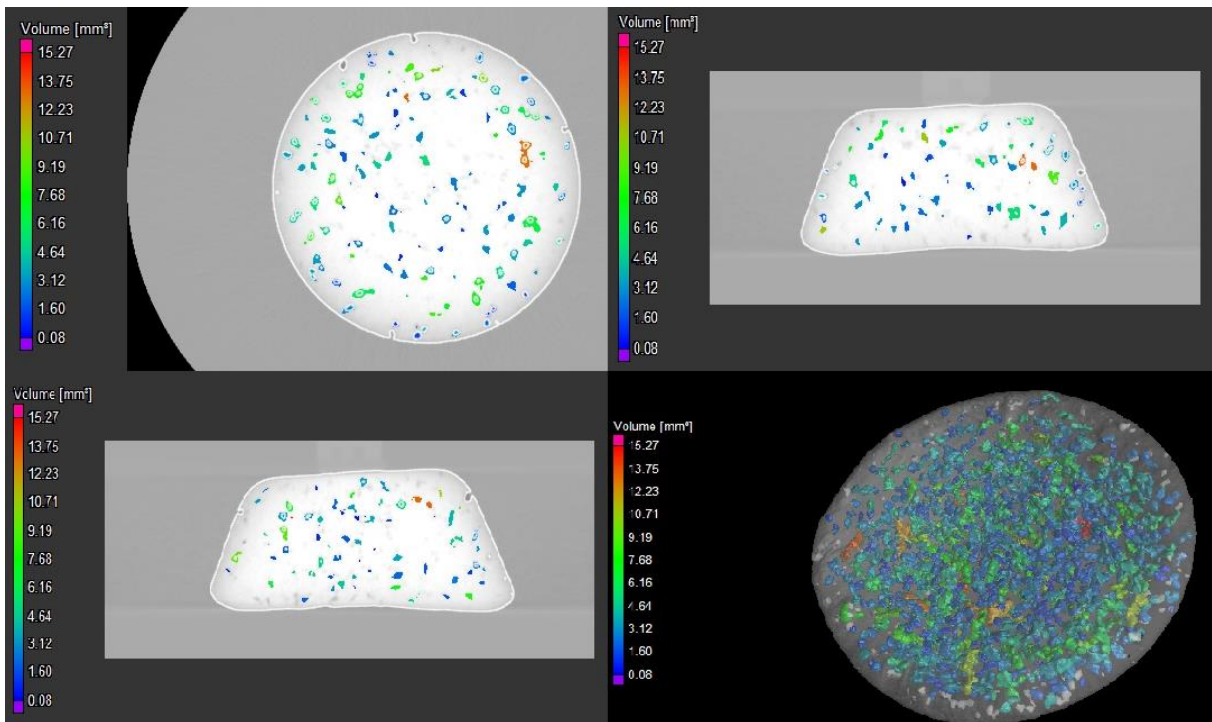
Figure 34. X-ray CT image after Porosity analysis sample C
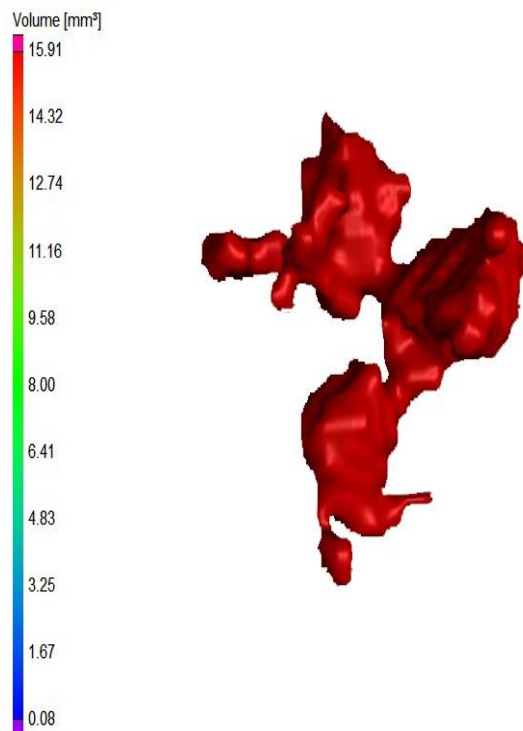
Figure 35. Largest pore in sample C with 10.19 mm^3 volume
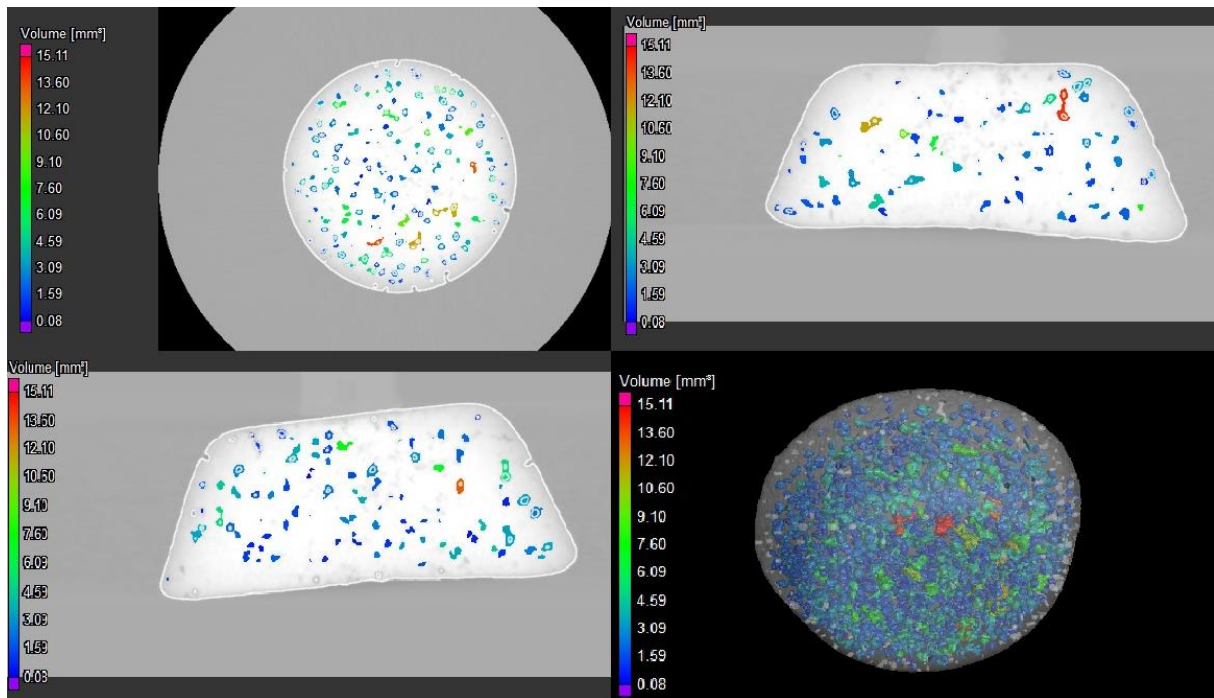
Figure 36. X-ray CT image after Porosity analysis sample D
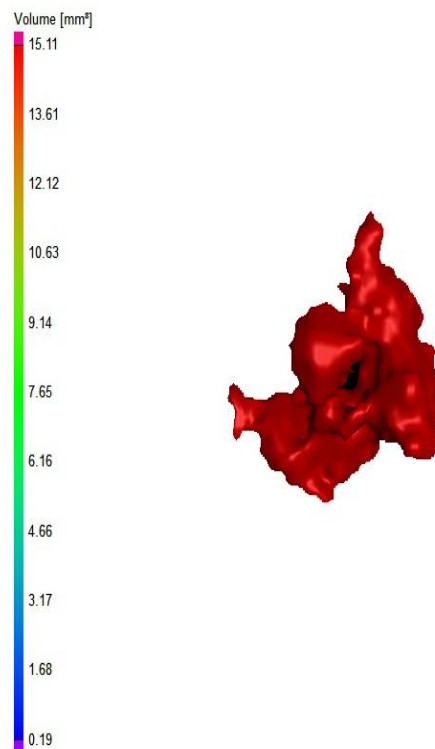
Figure 37. Largest pore in sample D with 10.19 mm^3 volume

Pore size distribution in each sample was found by exporting data from X-ray CT analysis.

Histograms as well as lognormal distributions fitted by using the maximum likelihood method

are presented in Figure 38. The lognormal distribution was hypothesized because pore size distribution in castings should theoretically be lognormal [122]. Moreover, recent observations in Mg [123] and Al [124, 125] alloy castings confirmed this theory. The density function (f) for the lognormal distribution is written as;

$$f(V) = \frac{1}{V\sigma\sqrt{2\pi}}\exp\left[\frac{-(\ln(V)-\mu)^2}{2\sigma^2}\right] \qquad (19)$$

where σ is the shape and μ is the scale parameter. The expected value, i.e., mean (average) of a lognormal distribution is found by;

$$\bar{V} = e^{\mu+\frac{\sigma^2}{2}} \qquad (20)$$
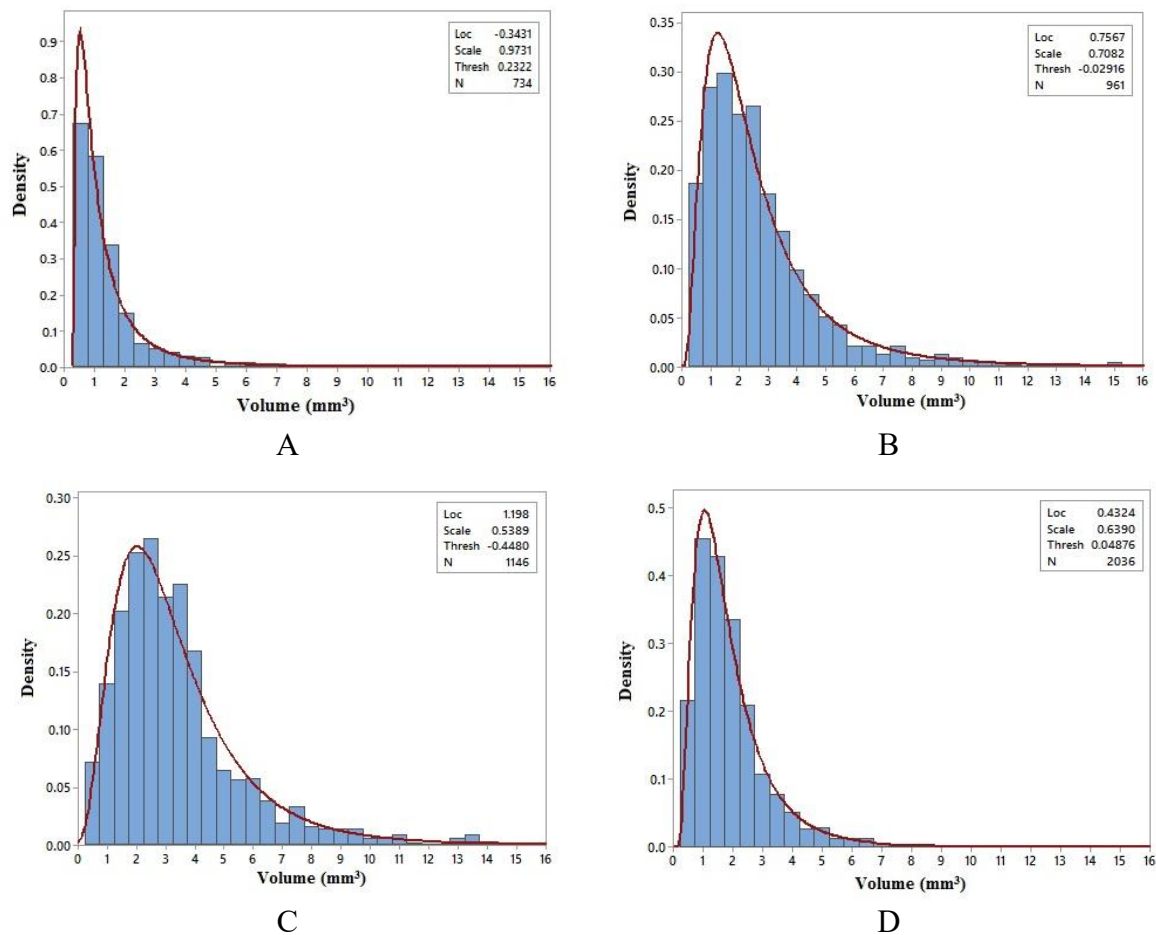
Figure 38. Pore size density distributions of A356 alloy RPT samples: A-sample without pouring, B&C- samples with 25 mm pouring (drop) height, D- sample with 150 mm drop height.

The estimated parameters are listed in Table 6. The goodness-of-fit of the estimated parameters was tested by using the Anderson-Darling statistic [126]. In all cases, the hypothesis that the data come from the fitted lognormal distributions could not be rejected.

Table 6. Estimated lognormal distribution parameters of A356 alloy RPT samples.

Sample	h_d (mm)	Location parameter	Scale parameter
A	0	-0.343	0.973
B	25	0.757	0.708
C	25	1.198	0.539
D	150	0.432	0.639

The change in number density of pores with drop height, h_d, is presented in Figure 39.a. The strong linear increase provides evidence on how damage to liquid aluminum is increased with pouring height. The velocity of the metal, v, was calculated based on gravitational acceleration for each height. The change in number density with filling velocity is given in Figure 39.b. The exponential increase in number density with filling velocity is noteworthy. The effect of pouring height (and filling velocity) on volume percent of pores is shown in Figure 40. Note that unlike N_p, the slope decreases with increasing height (velocity). However, it is clear that damage increases continuously with increasing filling speed.

The change in average pore volume and average equivalent pore radius with pouring height and filling velocity are presented in Figure 41 and Figure 42, respectively. Results demonstrate that the no pouring sample (sample D) has smaller mean pore size value among all samples, as expected. The decrease of mean pore size value between samples with 25 mm pouring height and sample with 150 mm height is noteworthy. This result can be interpreted as follows; oxide films that form during mold filling, when entrained, are torn to many pieces due to first impact when they hit the steel mold and then due to the bulk turbulence.

Consequently, there are many more pores, as evidenced by increased N_p in Figure 39, but with smaller size. Yet the overall effect is still increased damaged, as depicted in Figure 40.
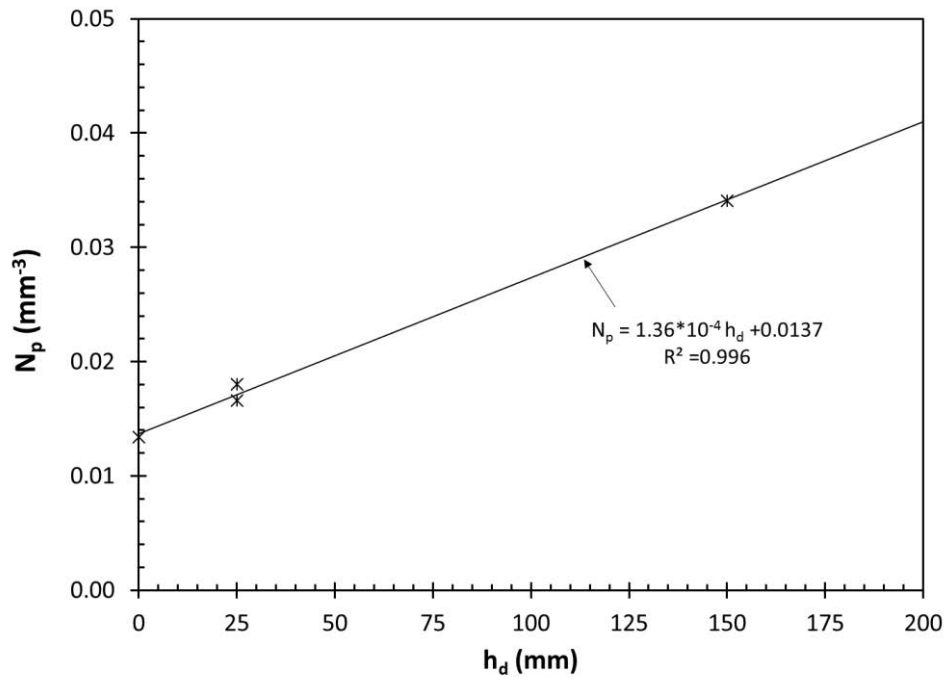
(a)
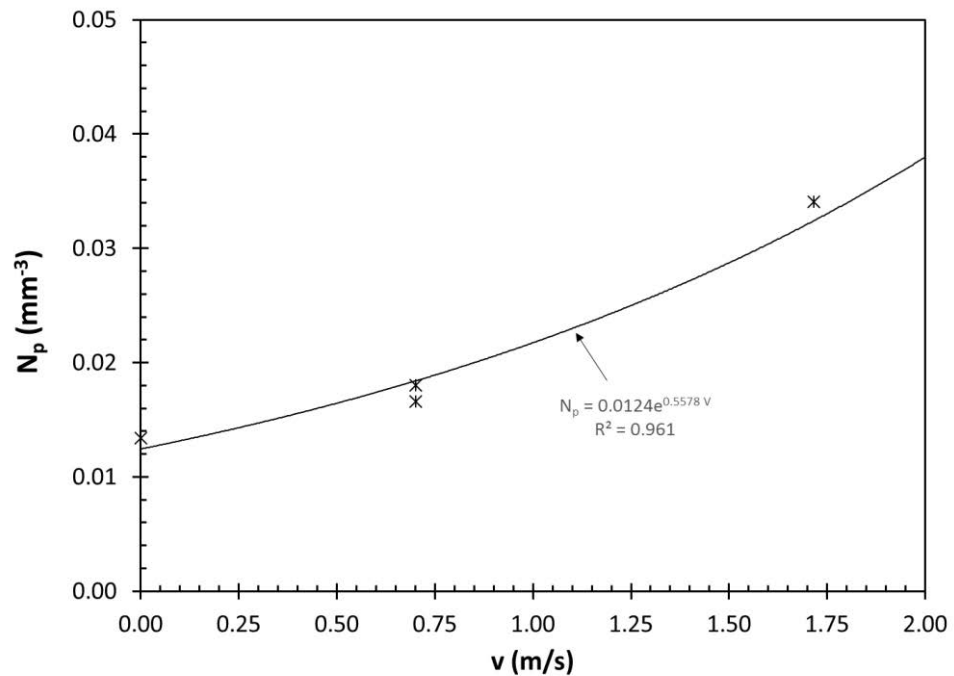
(b)

Figure 39. The change in number density with (a) drop height, and (b) filling velocity.
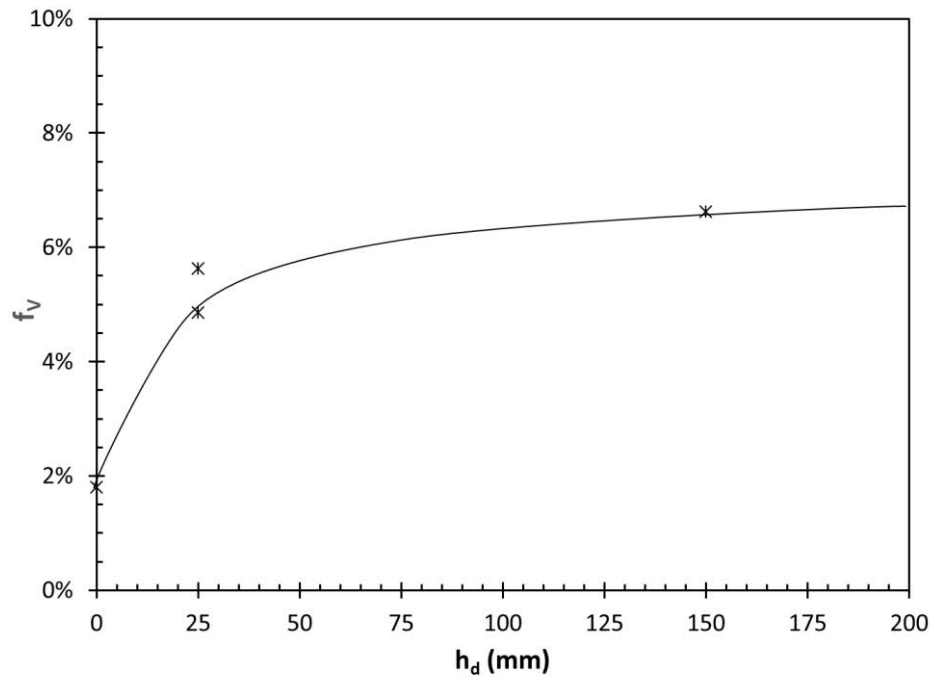
(a)
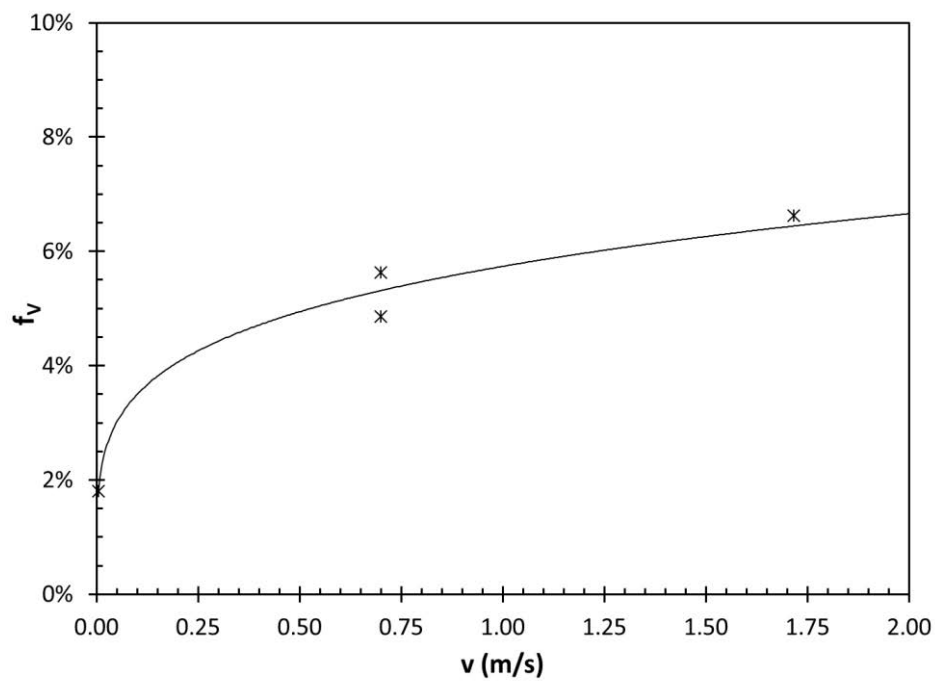
(b)

Figure 40. The change in volume fraction of pore with (a) drop height, and (b) filling velocity.
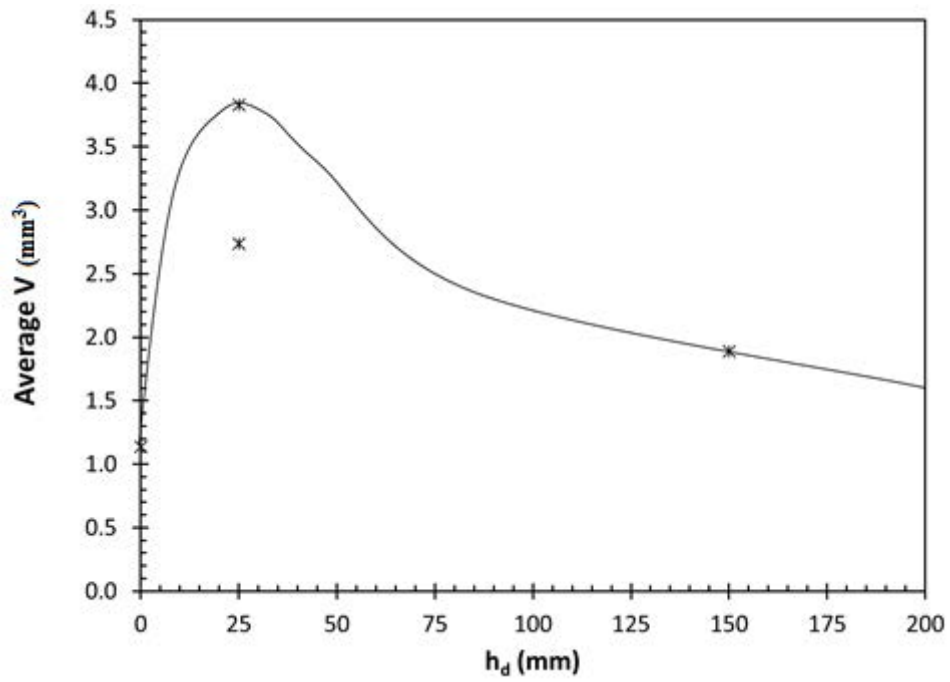
(a)
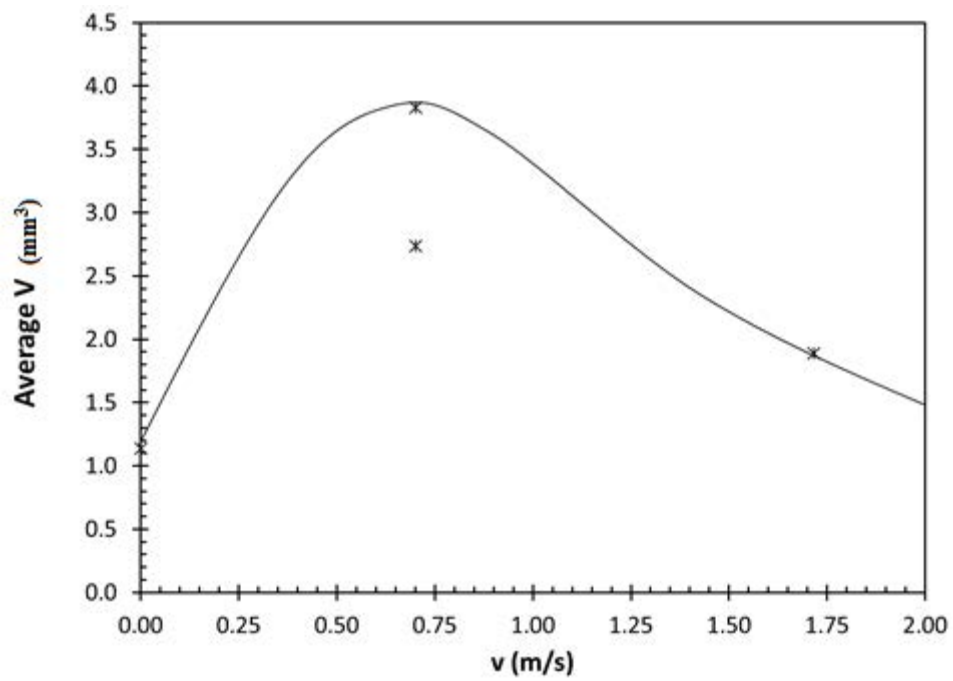
(b)

Figure 41. The change in average pore volume with (a) pouring height, and (b) filling velocity.
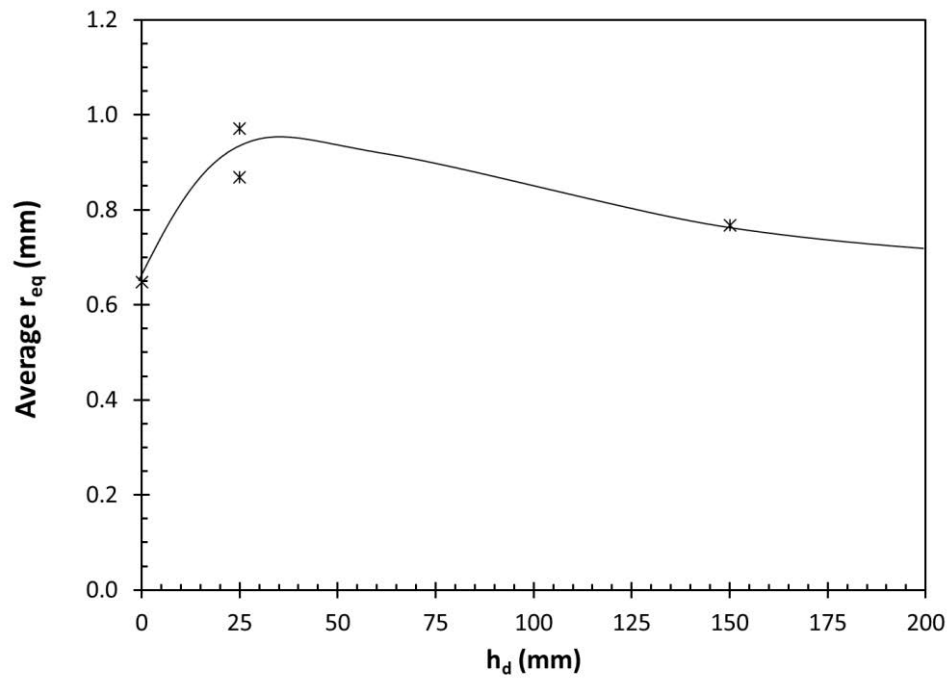
(a)
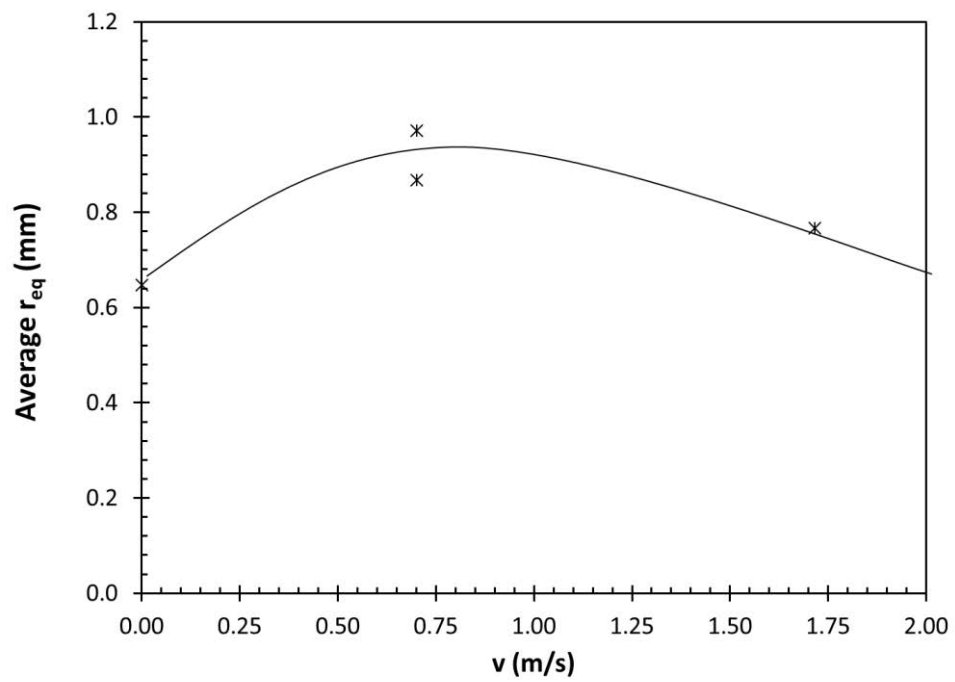
(b)

Figure 42. The change in average equivalent pore radius with (a) pouring height, and (b) filling velocity.

It is noteworthy that N_p and f_v, i.e., damage to liquid aluminum, increases continuously with filling velocity and there is no step function as in the results of Runyoro et al. [109]. From a fracture mechanics point of view, the expected breaking stress, σ_F, can be written as;

$$\sigma_F = \frac{K_c}{\beta\sqrt{\pi r_{eq}}}$$

(21)

The change in breaking stress with defect size is shown schematically [127], following the elastoplastic fracture mechanics model originally proposed by Gruenberg et al. [128]. Based on Figure 43, a continuous change in defect size would result in similarly a continuous change in breaking stress. Therefore, the step function reported by Runyoro et al. [109] is not consistent with fracture mechanics principles.
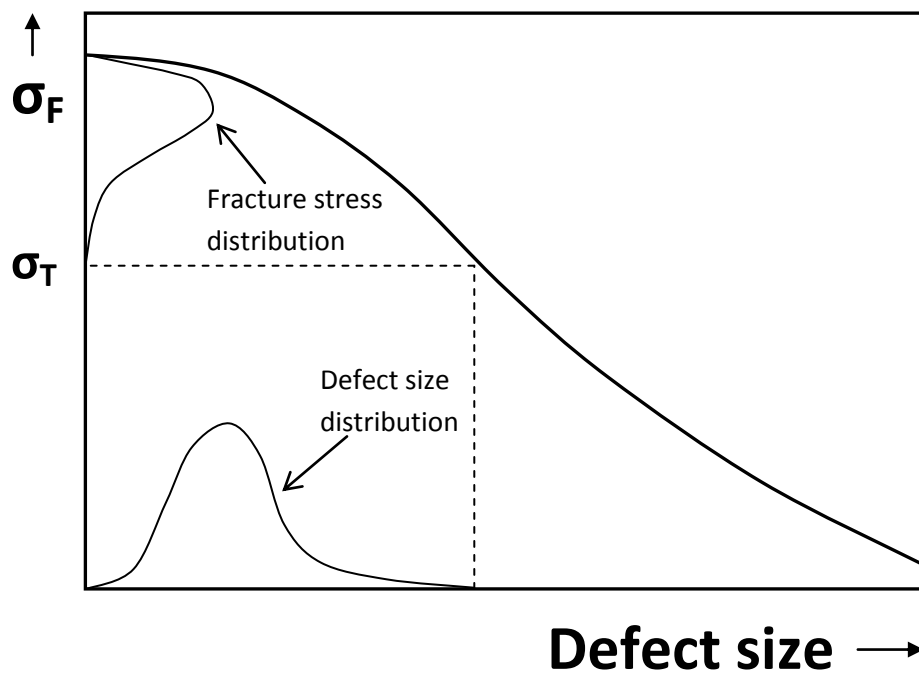
Figure 43. Schematic illustration of the link between defect size and fracture property distributions [127].

x5.2. Scanning Electron Microscopy of Pores

SEM images from a tangled pore exposed on sectioned the RPT sample of A356 alloy are presented in Figure 44 and Figure 45. Closer observations inside pores showed the presence of oxide films in every pore investigated, such as those presented in Figure 46 and Figure 47. There are newly-formed, thin ("young") oxides, as well as with original thick, "old" oxides coming from the crucible that were entrained into the melt. The oxide films torn apart between dendrites is exactly representing in Figure 24, suggesting that bifilms were fractured during solidification while pores grew under negative pressure.

Figure 48 shows a feature within a pore which shows wrinkles at its tips. This feature is interpreted as an oxide film folded-over multiple times during mold filling. Another interesting feature observed in some pores is "beach marks", indicated with arrows in Figure 49. To the author's knowledge, this feature has not been reported in the literature. The reasons for their formation is unknown and requires more research.
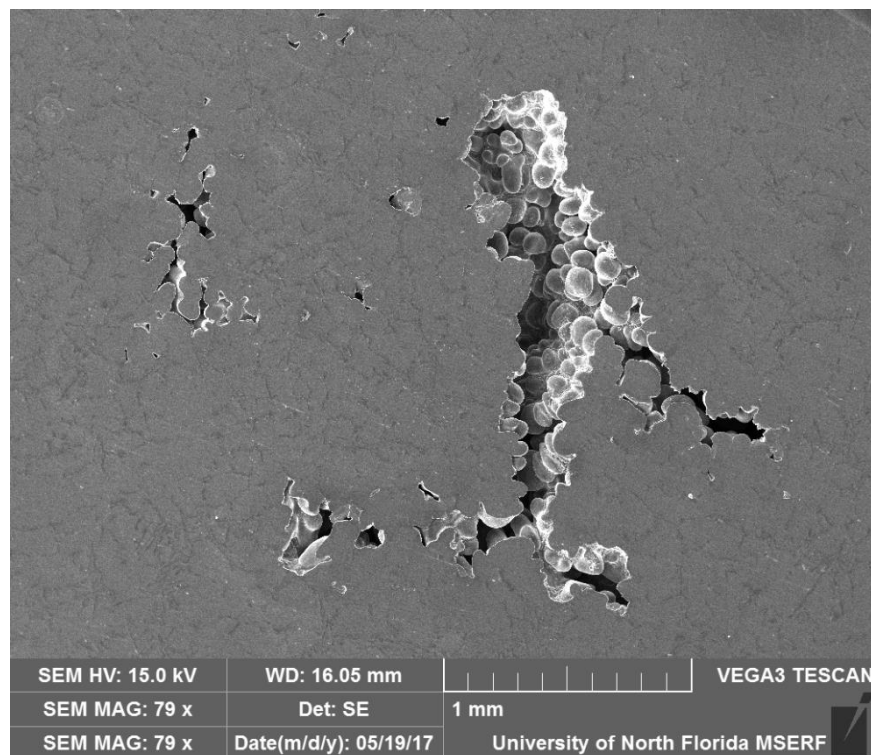
Figure 44. Overall view of a pore exposed on sectioned the RPT sample of A356 alloy.
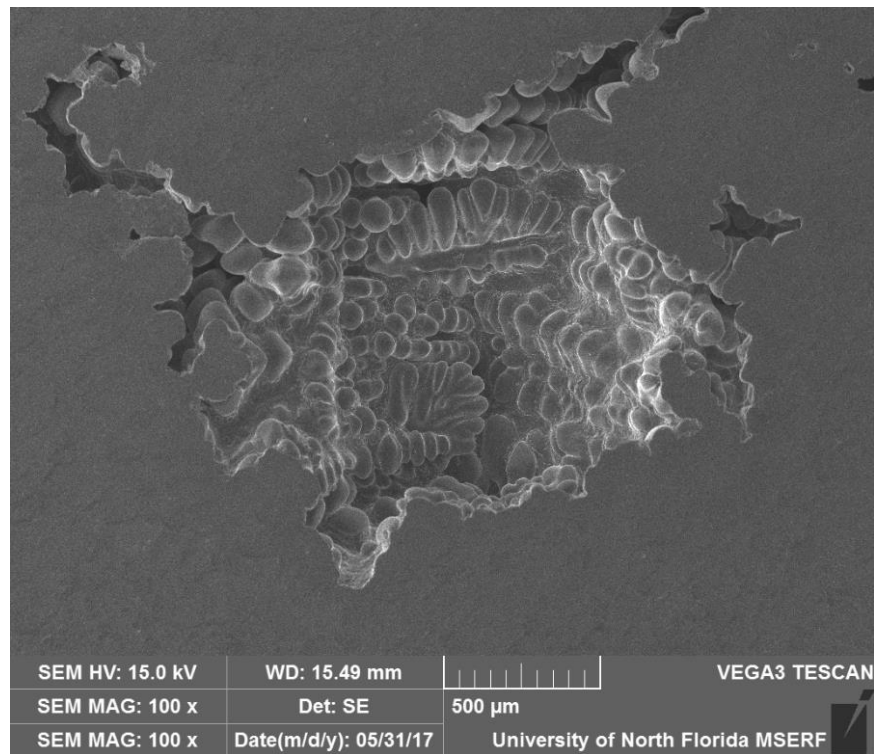
Figure 45. Overall view of a pore exposed on sectioned the RPT sample of A356 alloy.
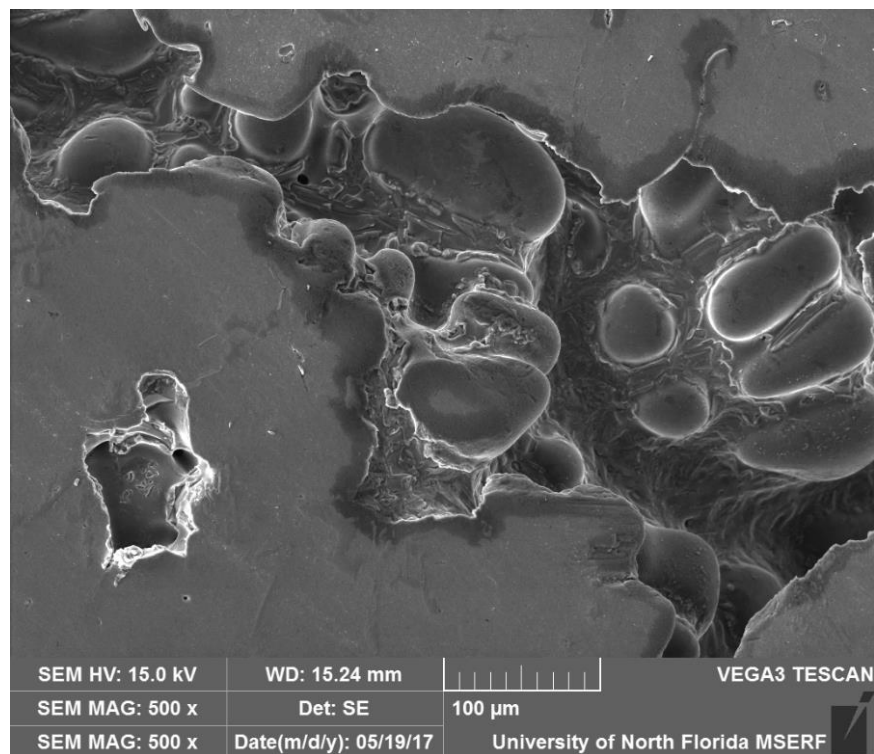
Figure 46. Close-up look at the pore exposed on sectioned the RPT sample of A356 alloy which presents fragments of a bifilm in between dendrites. (Dendrites are smooth and oxides are roughened areas)
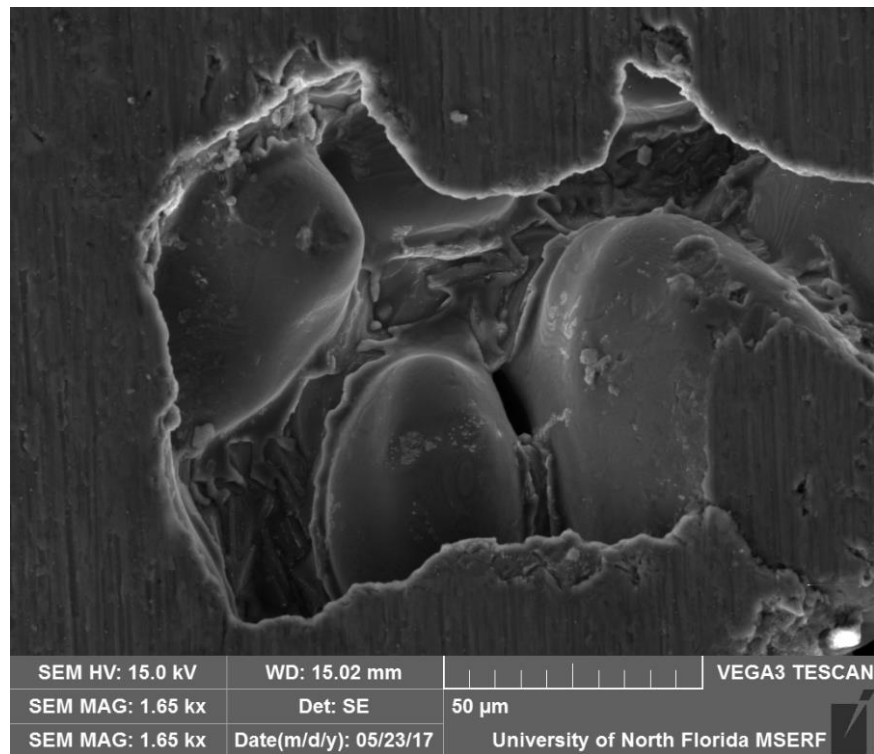
Figure 47. Close-up look at the pore exposed on sectioned the RPT sample of A356 alloy which presents fragments of a bifilm in between dendrites.
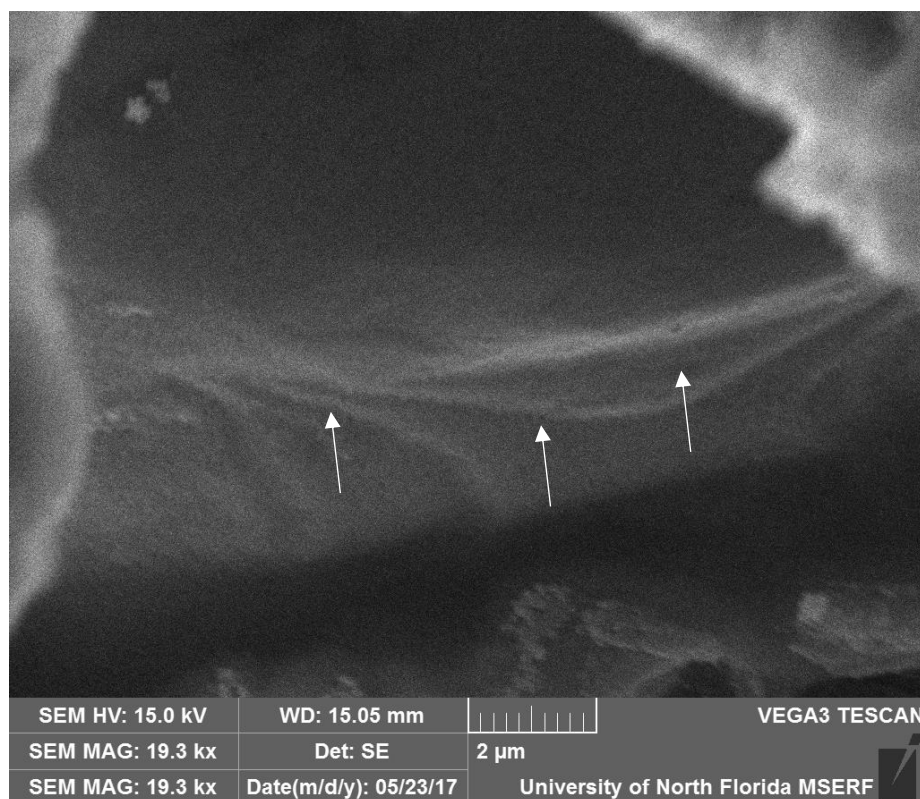
Figure 48. Magnified picture of a feature interpreted as a folded-over oxide film inside a pore.
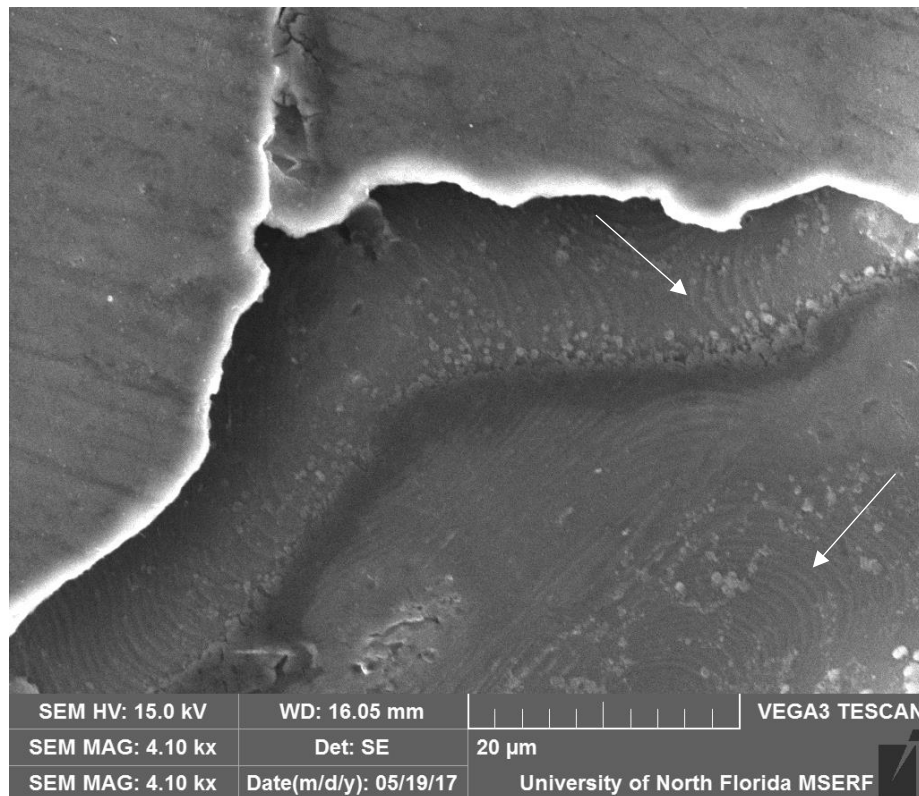
Figure 49. Close-up look at the surface of aluminum dendrite which shows oxide particles and some beach marks.

Electron diffraction spectroscopy (EDS) analysis was conducted in several regions where reliable data could be obtained. A pore is presented in Figure 50 and the EDS maps for several elements, including oxygen, aluminum, silicon and iron, are presented in Figure 51. Of particular importance is the EDS map for oxygen. The presence of oxygen inside the pore is clearly visible.

A pore and its surrounding area is shown in Figure 52. The most interesting aspect of this area is exposed in the EDS map for oxygen, shown in Figure 53. As indicated by arrows, oxygen is present at the edge of the pore. Additionally, a strong presence of oxygen is also evident away from the pores in a feature that is not completely discernible in Figure 52. This is a bifilm that never opened up during solidification, and would remain as an invisible defect without the EDS map. Hence, bifilms, reported as "invisible" defects by Campbell, are not invisible any more.
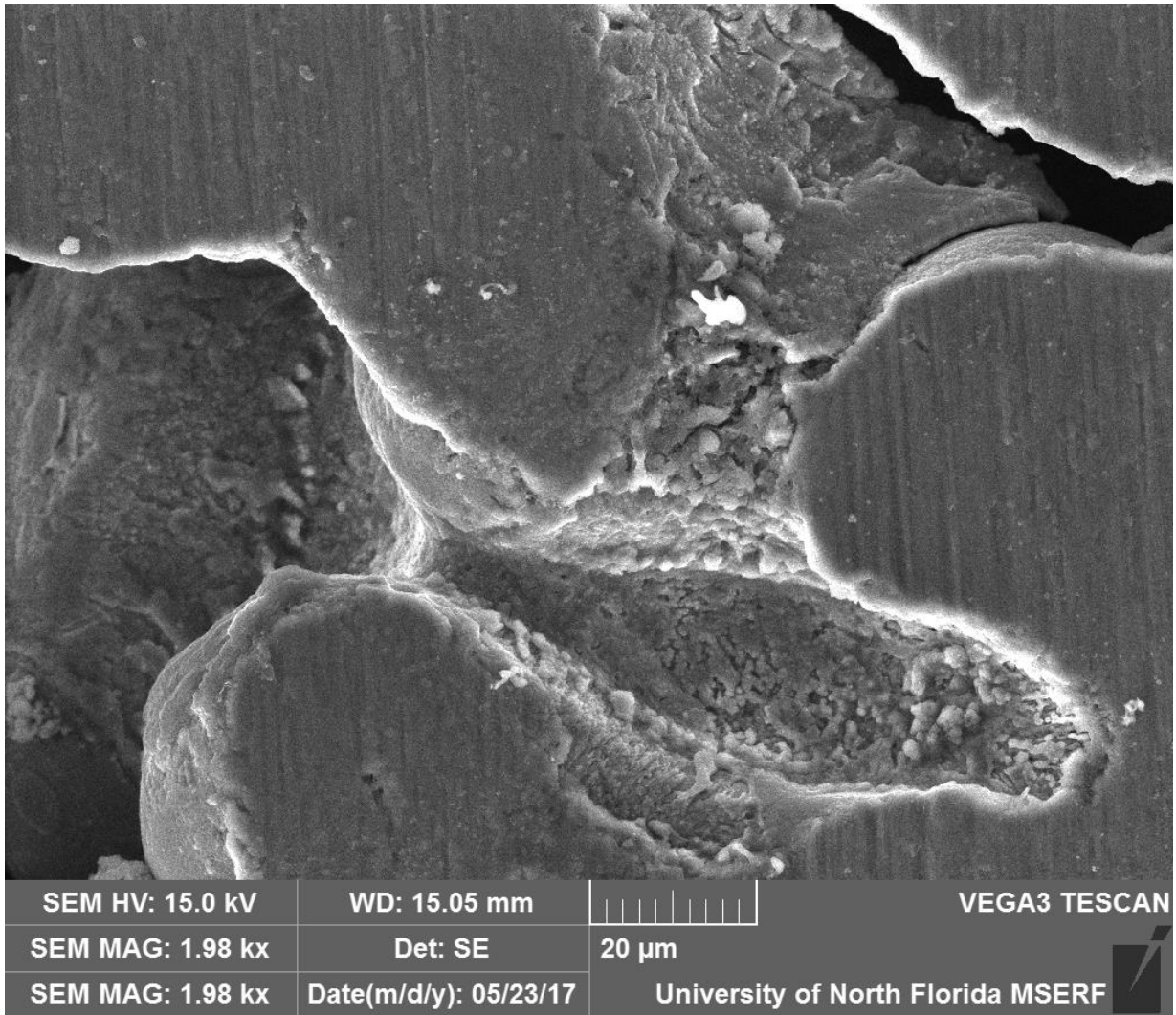
Figure 50. Close-up look at the root of a pore exposed on sectioned the of A356 alloy RPT sample
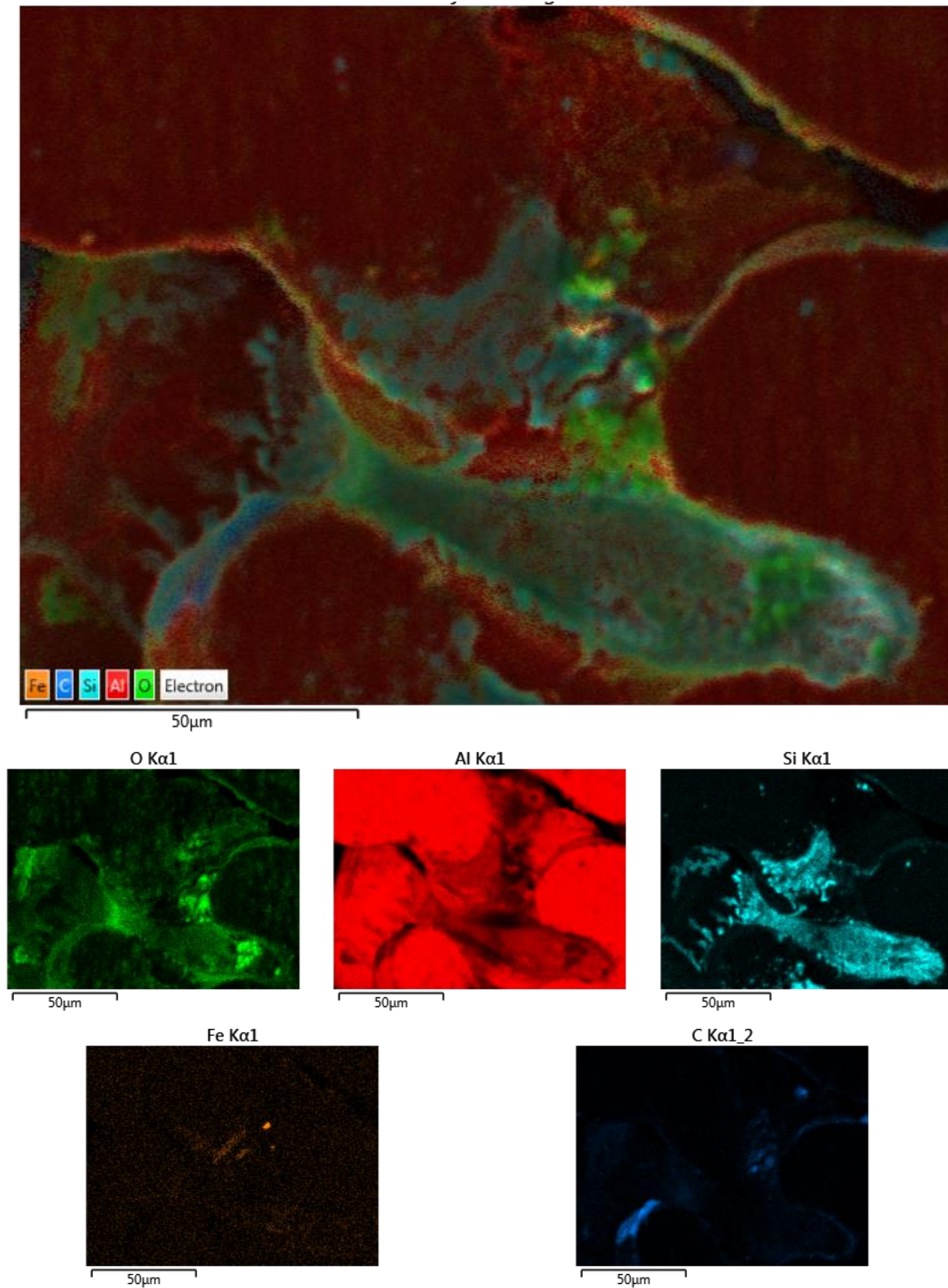
Figure 51. EDS analysis map of Figure 50 which demonstrate presence of oxide film and oxide flakes at the root of pore
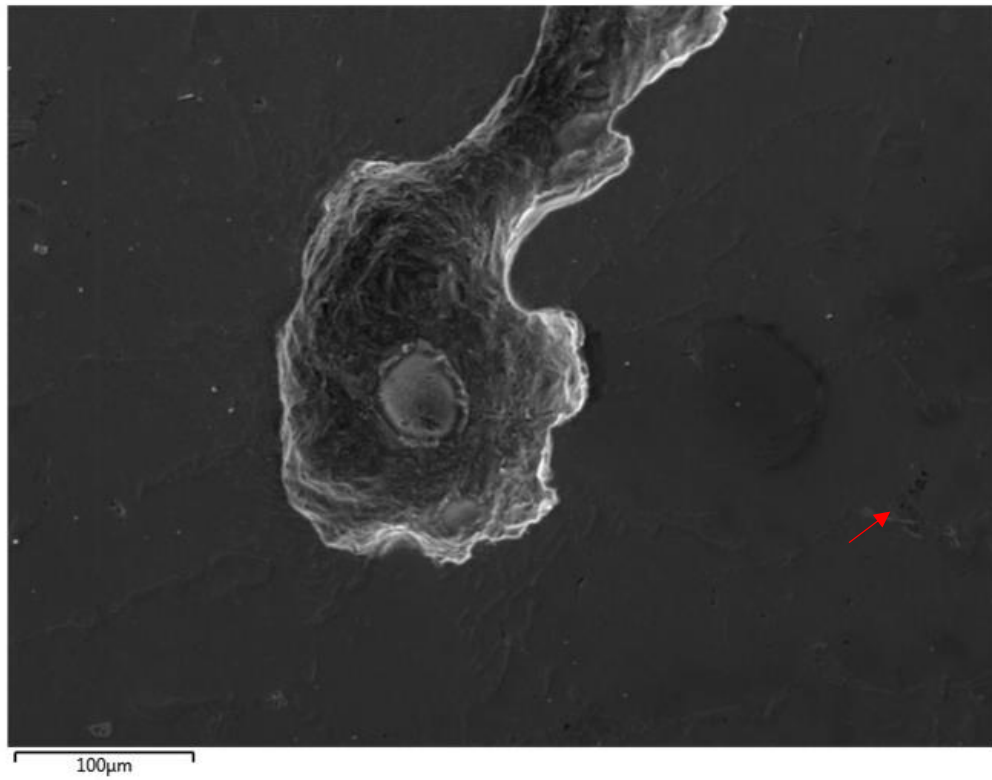
Figure 52. Close-up look at the root of a pore exposed.
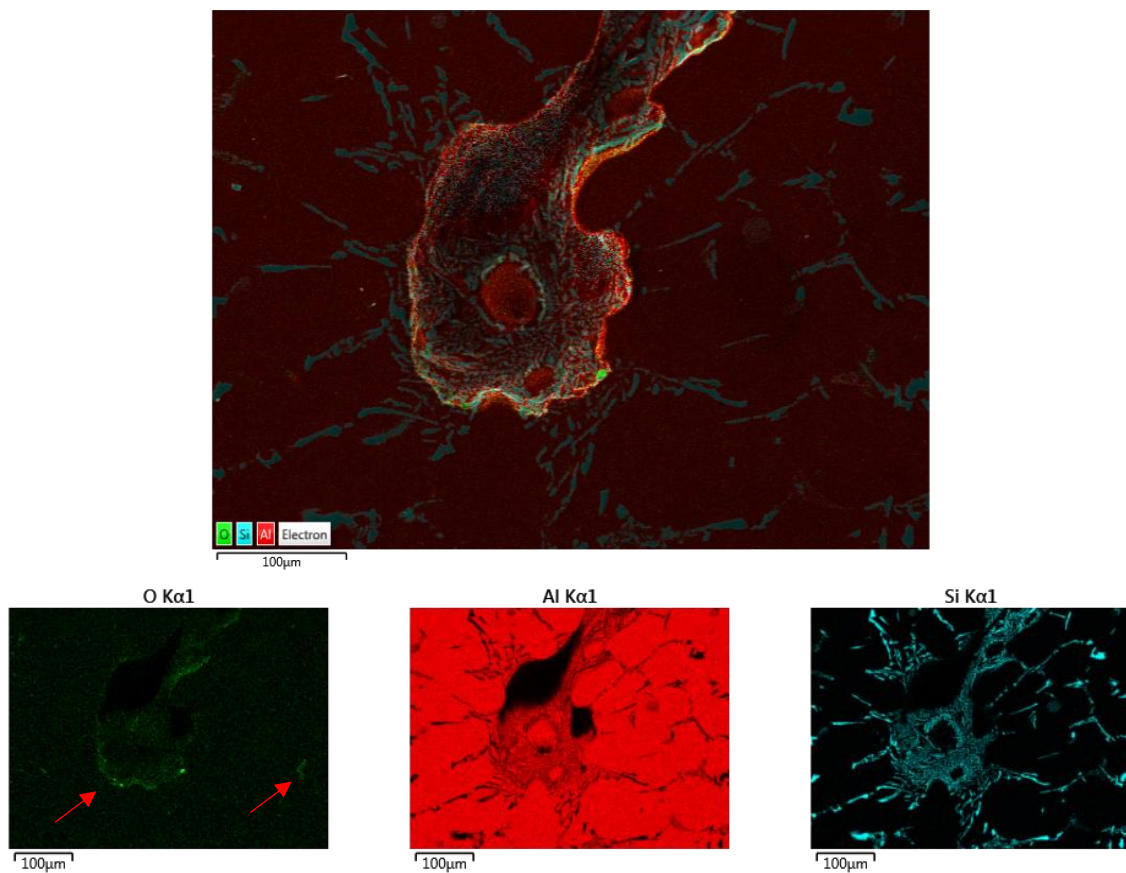
Figure 53. EDS analysis map of Figure 52 which demonstrate presence of oxide film at root of the pore.

A remarkable observation was made in the pore shown in Figure 54 in the encircled region. The EDS map for oxygen in Figure 55 shows presence of oxygen in three distinct locations indicated by arrows: (1) at the tip of the dendrite, providing evidence that dendrite is draped with an oxide film, (2) away from the pore, as an unopened, L-shaped bifilm, as well as (3) a slight linear trace. It is very significant that at the same location with the slight trace, there is Fe present. The long, linear shape of this Fe-bearing particle indicates that it is a β-phase (Al_5Fe) platelet, which seems to have precipitated on a "young" oxide bifilm.

A curved feature around a pore is shown in Figure 56. The EDS maps in Figure 57 show that the feature is a bifilm, evidenced by the strong presence of oxygen. EDS map for Si shows that Si eutectic particles precipitated on the bifilm. This finding will be discussed in detail later.

Figure 58 shows a pore and its vicinity in which no features are visible at first sight. EDS map for oxygen in Figure 59 show, however, the presence of three almost parallel bifilms as indicated with arrows. It is noteworthy that Si is present on two of those bifilms, giving further evidence that Si precipitated on oxides.

Two pores (possibly parts of a larger, buried pore) are shown in Figure 60. Curved features are barely visible on the SEM picture. EDS map for oxygen in Figure 61 clearly shows an intricate, curving bifilm, extending from inside one of the pores to the other one and beyond. This intricate bifilm, as well as the others shown above, clearly demonstrate that the actual size of the entrainment defect is larger than pores. This is a sobering observation, which emphasizes the importance of careful melt preparation, handling and filling system design.

It needs to be mentioned that all oxides observed in this study are actual damages to the metal, and not artifacts of polishing, because diamond polishing paste for sample preparation was used intentionally, as opposed to colloidal alumina suspensions. In addition, the absence

of carbon at the same spots where oxygen was found shows that oxygen traces are indeed oxides films, and not epoxy, in which samples were embedded.
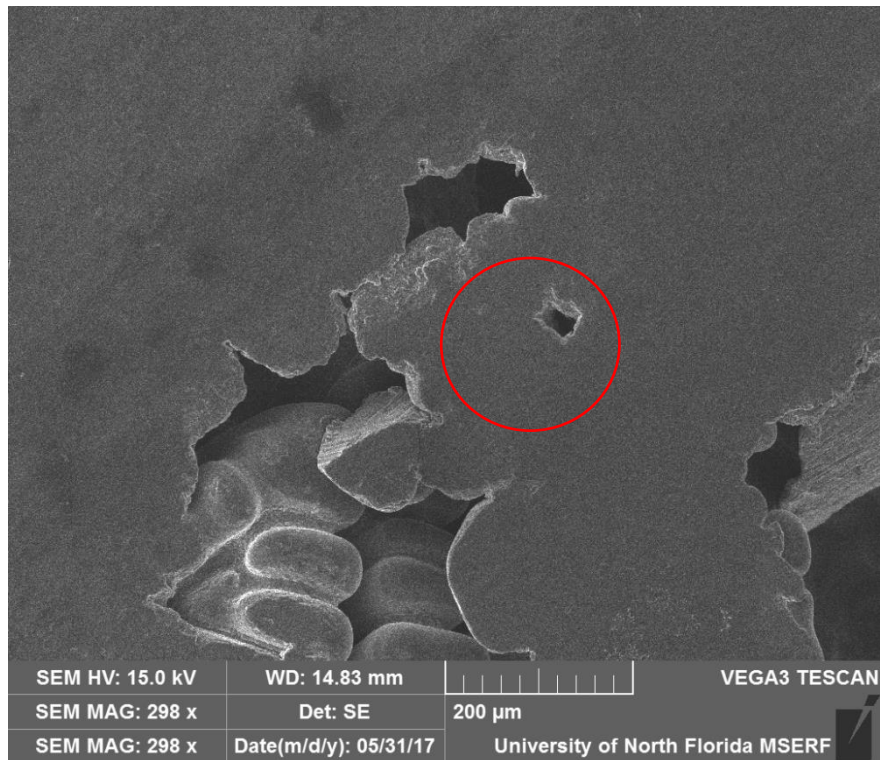
Figure 54. Close up look at the sectioned surface of the A356 alloy RPT sample
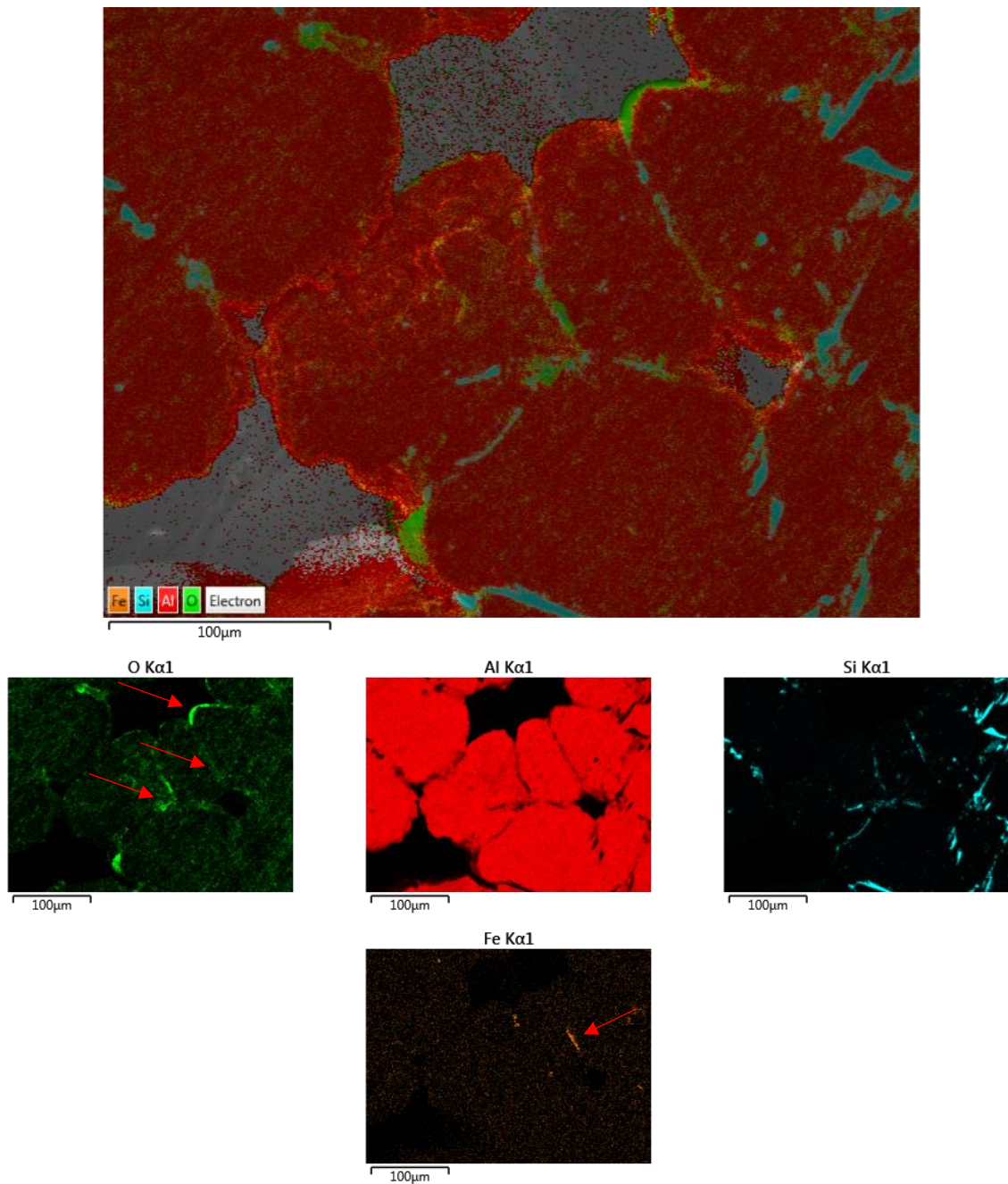
Figure 55. EDS analysis map of Figure 54, example of a closed bifilms which connected pores and act as a nucleation site for Fe particle
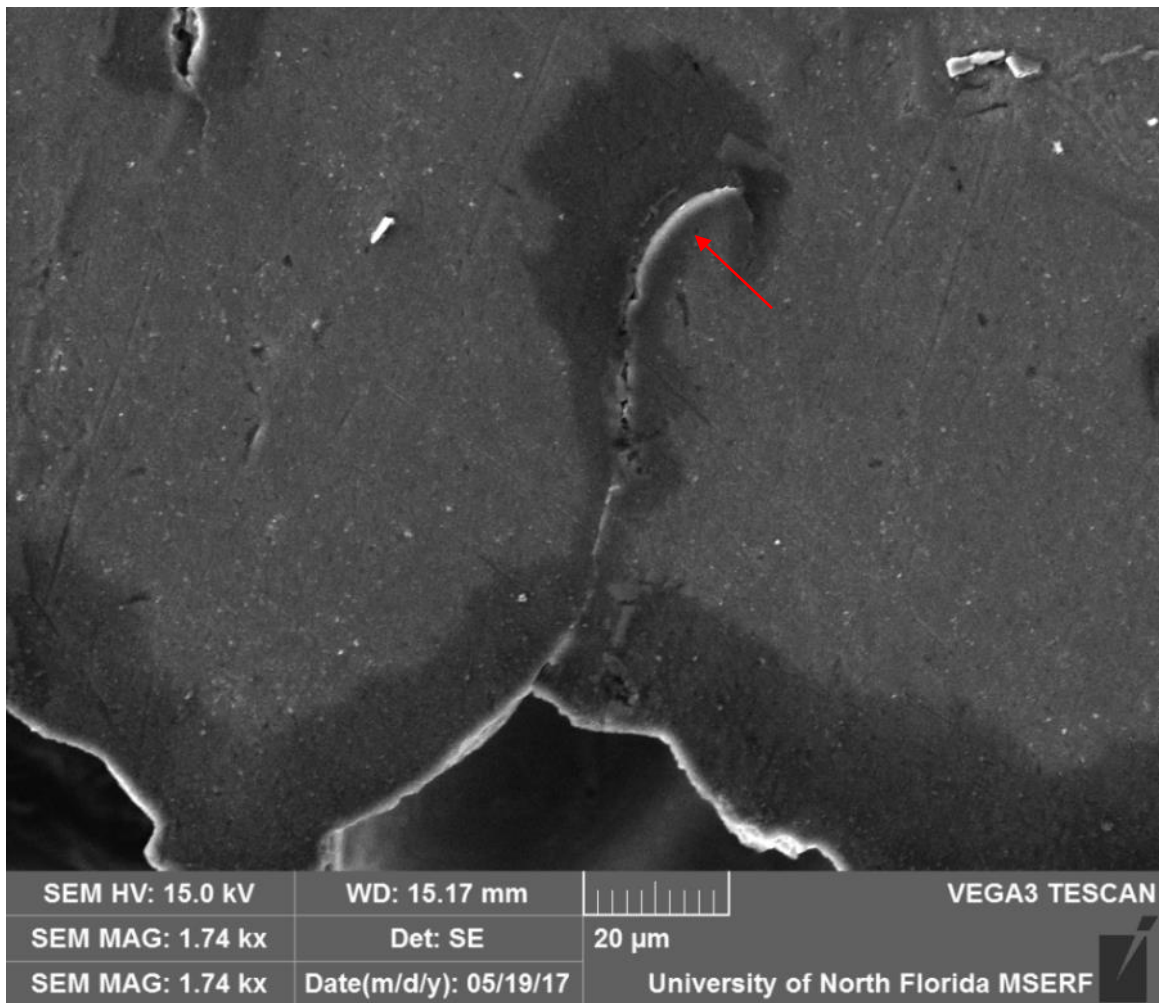
Figure 56. A curved feature near a pore.
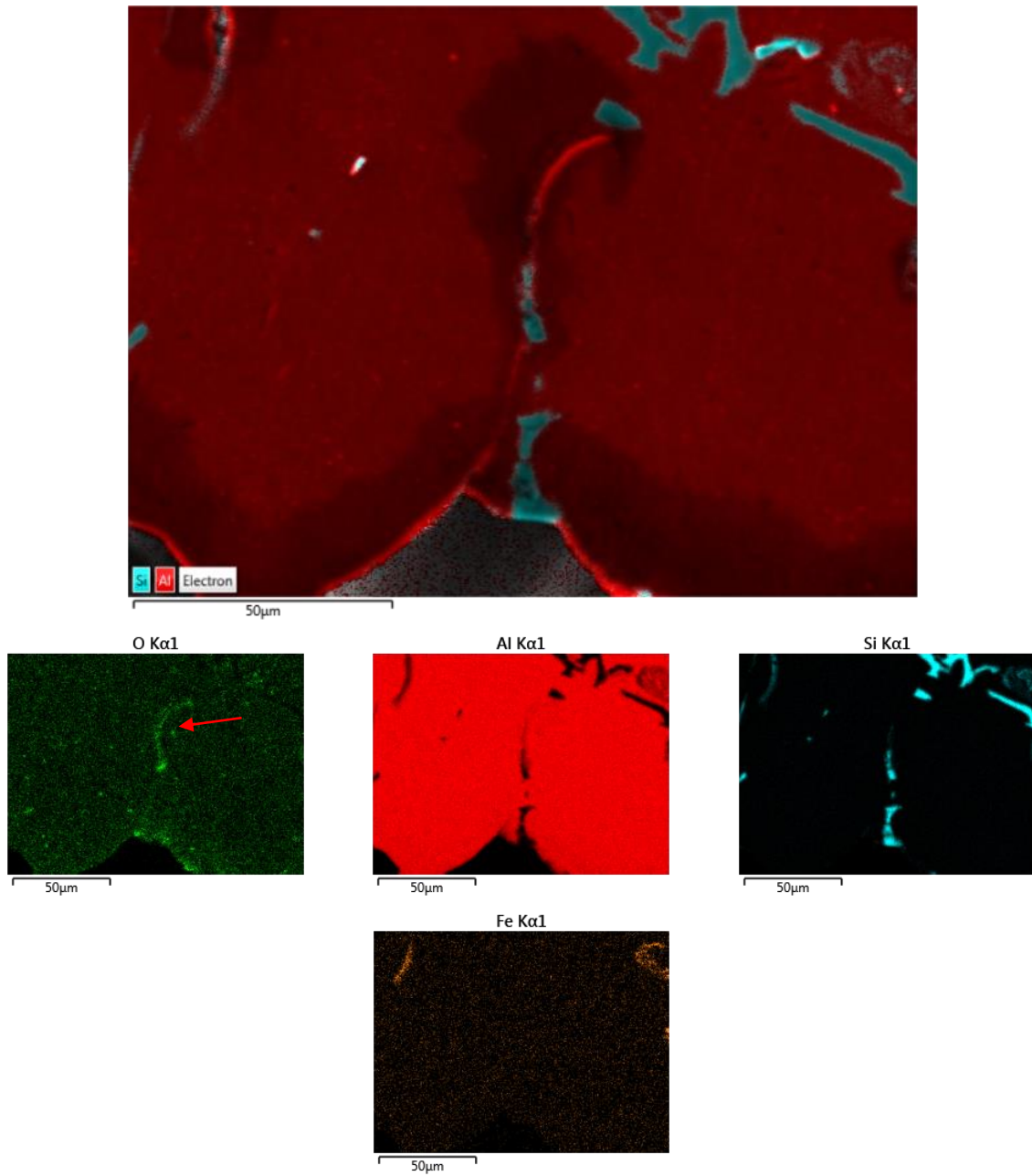
Figure 57. EDS analysis map of Figure 56 which illustrate the presence of a bifilm.
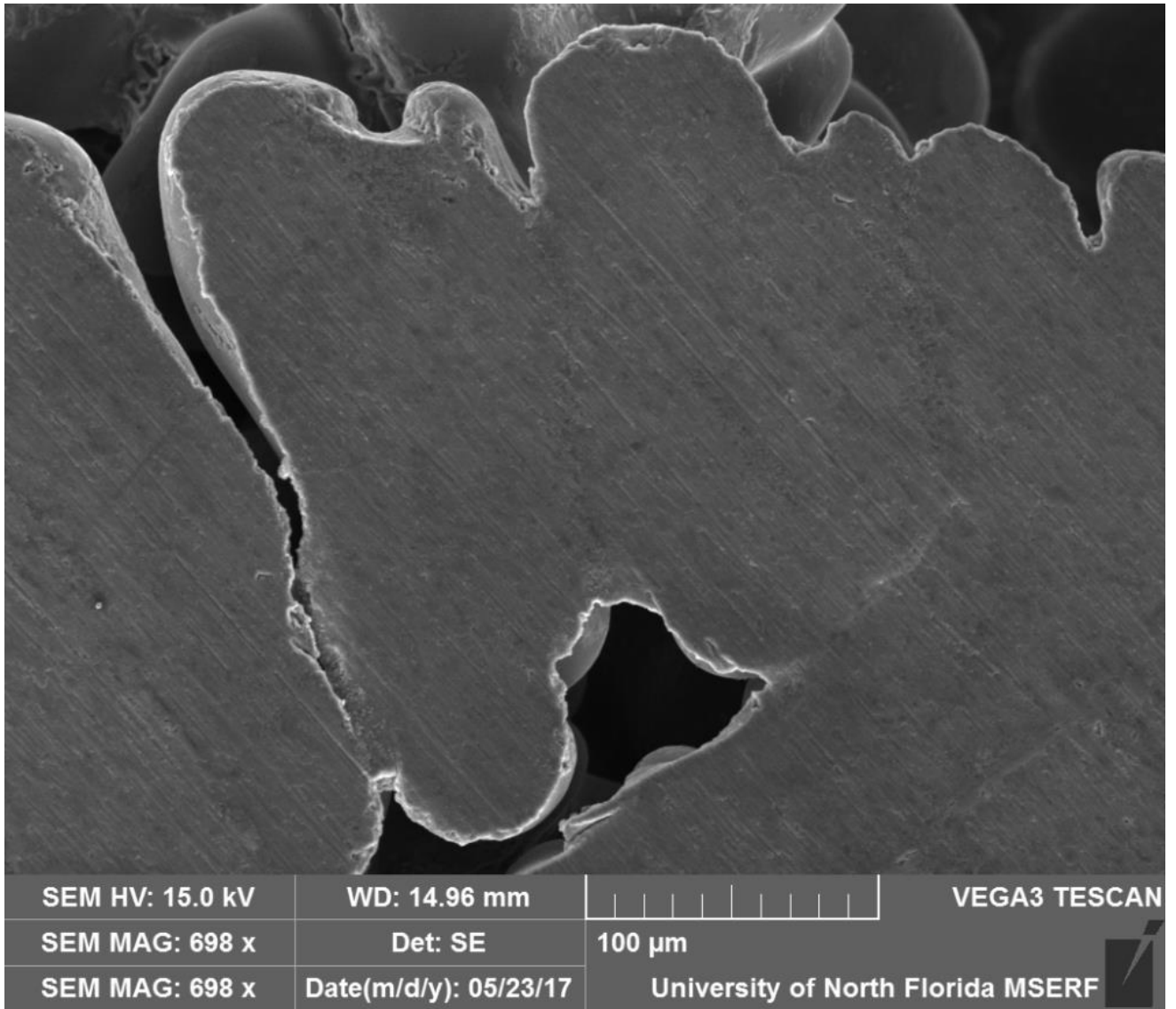
Figure 58. The vicinity of a pore.
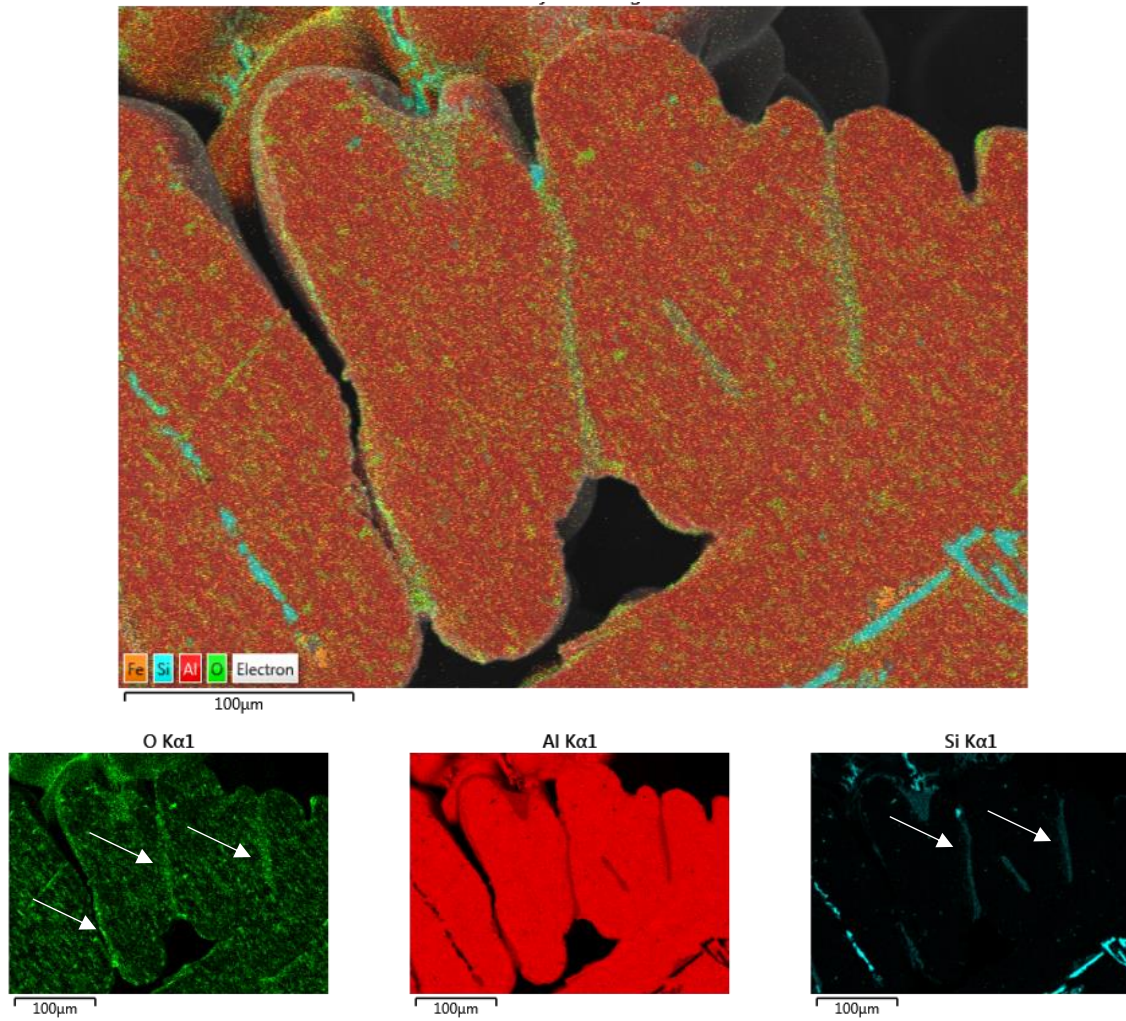
Figure 59. EDS analysis map of Figure 58 which illustrate presence of oxide film near silicon particles between dendrite arms.

Figure 60. Close up look at the sectioned surface of the A356 alloy RPT sample.
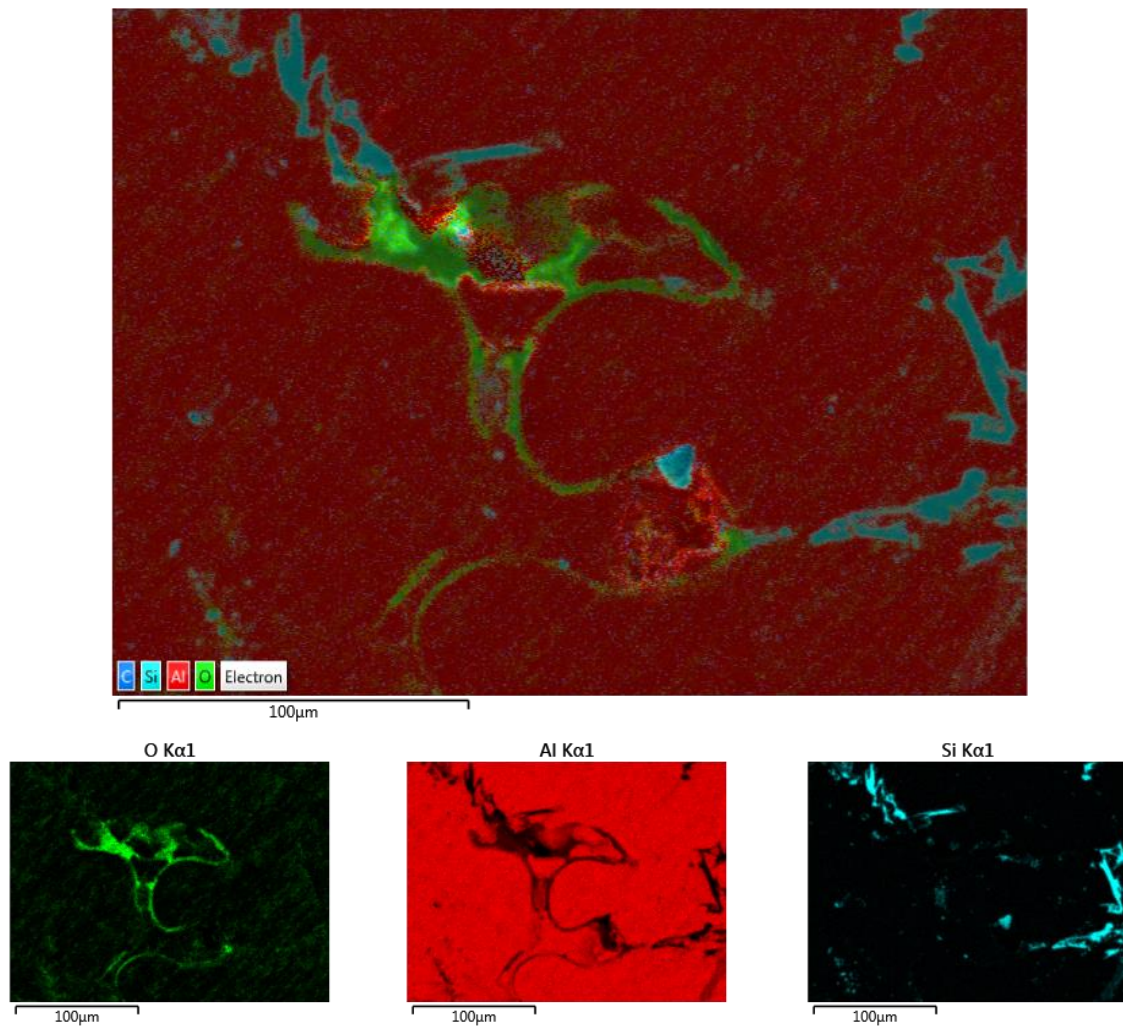
Figure 61. EDS analysis map of Figure 60 which shows presence of epoxy around the sample and a tangled long bifilm at the center of the picture.

Interpretation of Results

The results of the current study are in agreement with finding in former studies. That β-platelets precipitated on oxide bifilms was reported by Cao and Campbell [129, 130]. They stated that (i) the gap between two dry inner sides of a bifilm act as a crack, and (ii) the wetted outer sides are preferred substrates for the nucleation and growth of some intermetallics, especially Fe-rich phases. Cao and Campbell provided some SEM images, such as the one in Figure 62, which shows central cracks in certain intermetallics and apparent decohesion between some intermetallics. This phenomenon can only be explained by the bifilm theory. Experimental results reported by Miller et al. [131] and Liu et al. [132] provide strong support for this explanation. In both studies, the nucleation of β-platelets on bifilms were observed. A micrograph, showing a bifilm in the center of a β-platelet, provided by Liu et al., is presented in Figure 63. The results shown in Figure 55 is completely consistent with these studies.
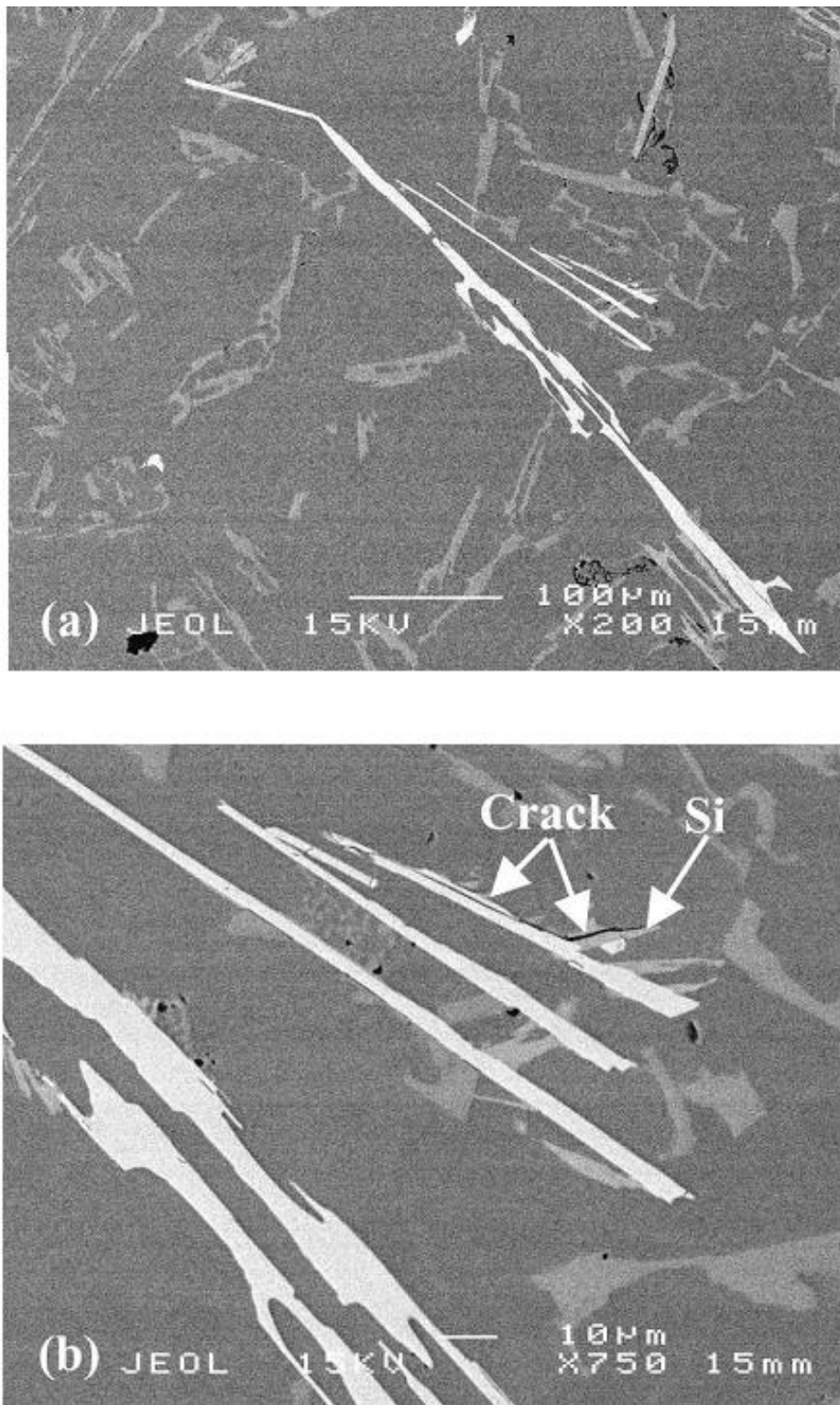
Figure 62. (a) and (b) Backscattered electron image of Al-11.5Si-0.4Mg Cast Alloy sedimented at 600 °C for 4 h showing β-Fe phase and cracks[129].
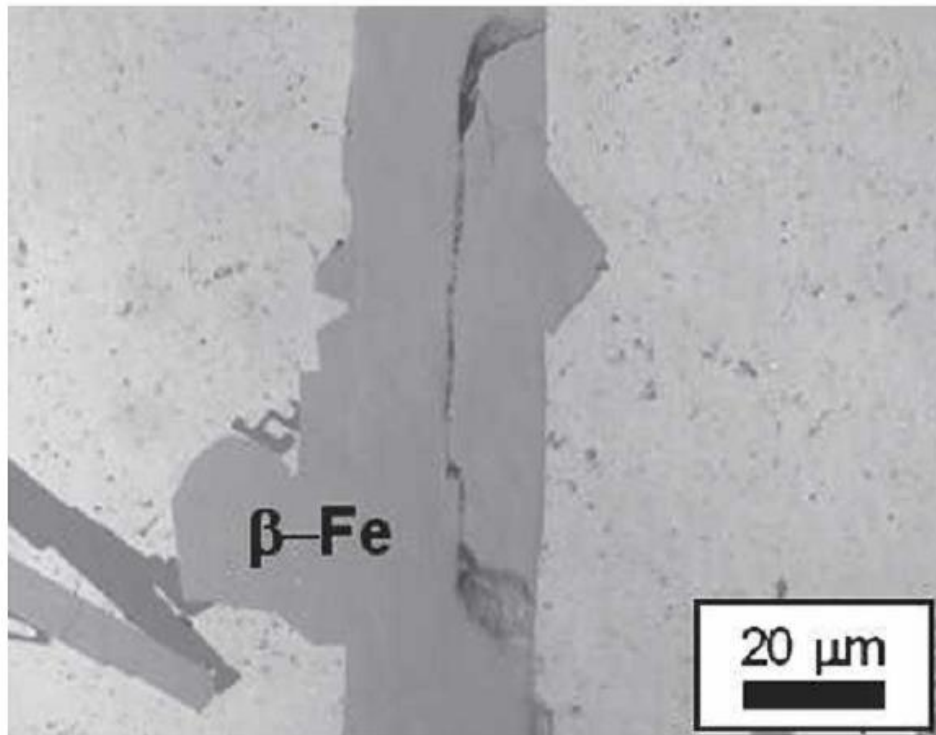
Figure 63. Optical micrographs of the Al-11.6Si-0.37Mg alloy prepared under conditions of heavily agitated to maximize oxide film entrainment. The β-Fe plate in the agitated sample contains a crack-like defect[131].

As stated above, in EDS maps in Figure 57 and Figure 59, evidence for O and Si being present at the same location was provided. This observation is consistent with results of Campbell [133] who found that a large bifilm can act as (i) a massive barrier, effectively separating two regions of the castings, and (ii) a preferential substrate for the silicon phase to precipitate on, as shown in Figure 64. In a different study, Tiryakioğlu [134] observed invisible interfaces on which Si particles seem to have precipitated, as shown in Figure 65. Indirect evidence for bifilms within Si particles was provided by Davidson et al. [135] who measured *in situ* the stress at which Si particles fractured in tension. The measured stress were at least an order of magnitude lower than expected strength levels. Davidson et al. attributed the results to the "possible" presence of incorporated of bifilms in Si, but added that these bifilms within

Si were not observed by anyone. Figure 59 clearly provides the evidence Davidson et al.

needed.
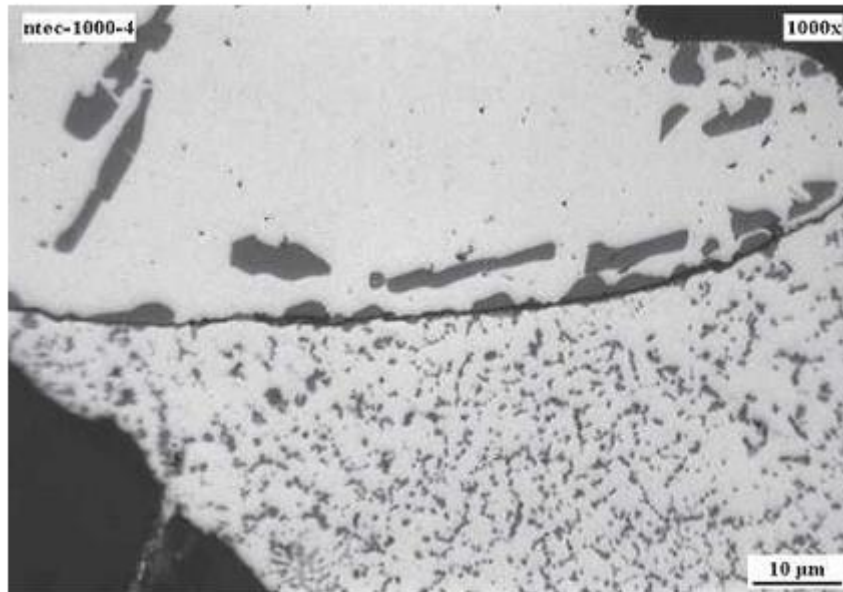
Figure 64. Example of a oxide bifilm acting as a substrate for silicon to precipitate on, but not for aluminum [133].
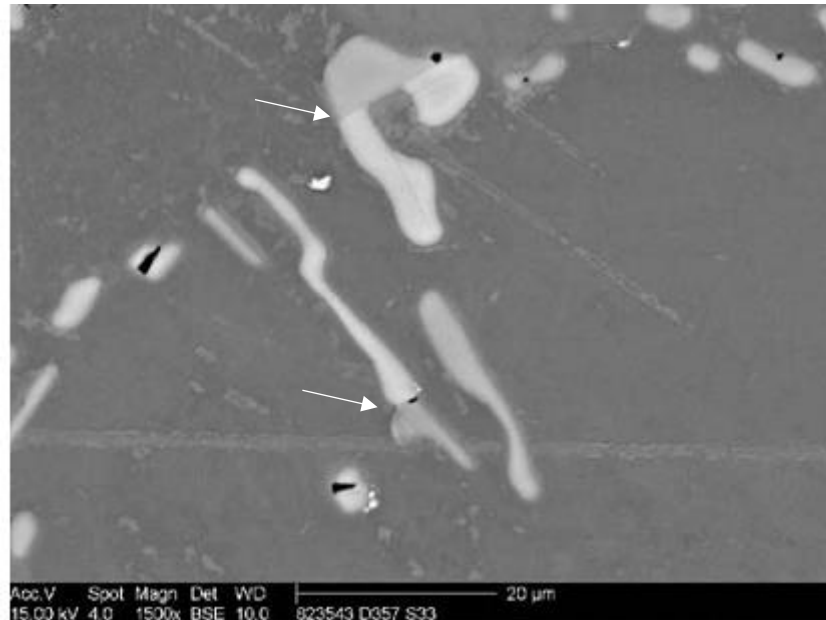
Figure 65. Microstructure of Al-7Si-0.6Mg alloy which shows hidden interfaces inside the silicon particles. (Si particles are gray and Mg_2Si particles are black spots)

6. CONCLUSIONS

Research Question 1: Are pores extrinsic or intrinsic defects?

- Calculations for fracture pressure, critical pore size and probability of formation of a vacancy cluster at or above the critical size, based on classical nucleation theory, showed that homogeneous nucleation of a pore in solidifying aluminum is impossible.

- The review of the literature along with calculations showed that for heterogeneous nucleation, (i) a substrate with low wetting condition needs to be present in liquid aluminum, (ii) the fracture pressure for heterogeneous nucleation on the most favored (least wetted surface) is two orders of magnitude higher than experimental tensile strengths for solidifying aluminum alloys. Therefore, heterogeneous nucleation is not possible.

- The only mechanism available for pore formation in solidifying aluminum is the presence of bifilms, which can inflate due to reduced pressure and/or hydrogen segregation. Therefore, pore formation does not involve nucleation, it is a pure growth process.

- The bifilm theory appears to be completely consistent with *in situ* observations and assumptions commonly made in the casting/solidification literature.

- <u>As opposed to statements made in the literature, pores are not intrinsic but extrinsic defects. Therefore they can be eliminated.</u>

Research Question 2: Are in situ observations and modeling assumptions consistent with the physics of pore nucleation?

- Assumption commonly made in the literature that pores form only in the last stages of solidification when solid fraction and local hydrogen supersaturation are high, is not accurate. Examples of *in situ* observations from the literature showed that pore may initiate (i) far from the solidification front where hydrogen supersaturation has not occurred yet, and (ii) at a low solid fraction

- The bifilm theory only can fill the gap between *in situ* observations and assumptions commonly made in the casting/solidification literature and also be an explanation which is consistent with the physics of pore nucleation.

Research Question 3: Is the damage to liquid aluminum by entrainment a step function?

- A step function is not consistent with elastoplastic fracture mechanics principles.

- X-ray CT porosity analysis showed number of pores and volume fraction of pore in aluminum casting were increased by raising the pouring height and also there is a linear relation between pouring height and number of pores per unit of bulk volume.

- X-ray CT porosity analysis also showed the average pore radius size, first increases by raising the filling velocity and then decreases. Also number density of pores and volume fraction of pores change continuously. Therefore a step function in breaking stress is not consistent with the results of the current study.

Research Question 4: Are young bifilms still invisible?

- Scanning electron microscopy images and EDS maps of RPT specimens confirmed the presence of oxide films inside all pores, between dendrite arms, even far from pores which did not open up during solidification. Therefore bifilms are not invisible anymore, or at least they are less invisible.

Research Question 5: Can bifilms be observed away from pores on micrographs?

- EDS analysis of RPT specimens demonstrated the presence of oxide films far away from pores which did not open up during solidification. These bifilms were not visible in SEM images.

7. FUTURE WORK

- Carry out more pouring tests with different pouring heights and alloys to have better statistical analysis.

- Carry out some tensile tests with the same poring conditions to correlates melt quality to mechanical properties and establish the map between pore volume fraction and number of pore per unit of bulk volume, showing the contours of strength and elongation.

- An investigation on image analysis of X-ray CT images to determine the morphologies of pores for prediction of mechanical properties, especially fatigue properties.

- Re-processing of the RPT test results obtained from the thesis and with the data that is going to be collected from the future tests, a statistical technique will be used to analyze RPT results in order to find out how many samples should be taken from a melt to get a reliable assessment of the quality of the melt.

References

[1]   J. R. Davis, *ASM specialty handbook: heat-resistant materials*. Asm International, 1997.

[2]   D. Dispinar, "Determination of metal quality of aluminium and its alloys," University of Birmingham, 2006.

[3]   J. Hirsch, "Aluminium in innovative light-weight car design," *Materials Transactions,* vol. 52, no. 5, pp. 818-824, 2011.

[4]   J. Campbell, *Complete Casting Handbook: Metal Casting Processes, Metallurgy, Techniques and Design*. Elsevier Butterworth-Heinemann, 2011.

[5]   N. R. Green and J. Campbell, "Statistical distributions of fracture strengths of cast Al-7Si-Mg alloy," *Materials Science and Engineering: A,* vol. 173, no. 1, pp. 261-266, 1993/12/20 1993.

[6]   C. Nyahumwa, N. R. Green, and J. Campbell, "Influence of casting technique and hot isostatic pressing on the fatigue of an Al-7Si-Mg alloy," *Metallurgical and Materials Transactions A,* journal article vol. 32, no. 2, pp. 349-358, 2001.

[7]   C. D. Lee and K. S. Shin, "Effect of microporosity on the tensile properties of AZ91 magnesium alloy," *Acta Materialia,* vol. 55, no. 13, pp. 4293-4303, 8// 2007.

[8]   C. D. Lee, "Effect of grain size on the tensile properties of magnesium alloy," *Materials Science and Engineering: A,* vol. 459, no. 1–2, pp. 355-360, 6/25/ 2007.

[9]   J. Song, S.-M. Xiong, M. Li, and J. Allison, "In situ observation of tensile deformation of high-pressure die-cast specimens of AM50 alloy," *Materials Science and Engineering: A,* vol. 520, no. 1–2, pp. 197-201, 9/15/ 2009.

[10]   M. Tiryakioğlu, "On estimating the fracture stress and elongation of Al–7%Si–0.3%Mg alloy castings with single pores," *Materials Science and Engineering A,* vol. 527, no. 18–19, pp. 4546-4549, 7/15/ 2010.

[11]   J. T. Staley Jr., M. Tiryakioğlu, and J. Campbell, "The effect of hot isostatic pressing (HIP) on the fatigue life of A206-T71 aluminum castings," *Materials Science and Engineering: A,* vol. 465, no. 1, pp. 136-145, 2007.

[12]   Q. G. Wang, D. Apelian, and D. A. Lados, "Fatigue behavior of A356-T6 aluminum cast alloys. Part I. Effect of casting defects," *Journal of Light Metals,* vol. 1, no. 1, pp. 73-84, 2// 2001.

[13]   M. Tiryakioğlu, J. Campbell, and C. Nyahumwa, "Fracture surface facets and fatigue life potential of castings," *Metallurgical and Materials Transactions B,* vol. 42, no. 6, pp. 1098-1103, 2011.

[14]   C. Nyahumwa, N. Green, and J. Campbell, "Effect of Mold-Filling Turbulence on Fatigue Properties of Cast Aluminum Alloys (98-58)," *Transactions of the American Foundrymen's Society,* vol. 106, pp. 215-223, 1998.

[15]   N. Promisel, "Evaluation of Non-Ferrous Materials," in *Materials Evaluation in Relation to Component Behavior, Proc. Third Sagamore Ordnance Materials Research Conference*, 1956.

[16]   H. Mayer, C. Ede, and J. Allison, "Influence of cyclic loads below endurance limit or threshold stress intensity on fatigue damage in cast aluminium alloy 319-T7," *International journal of fatigue,* vol. 27, no. 2, pp. 129-141, 2005.

[17]   M. Tiryakioğlu, J. Campbell, and J. T. Staley, "Evaluating structural integrity of cast Al–7% Si–Mg alloys via work hardening characteristics," *Materials Science and Engineering: A,* vol. 368, no. 1-2, pp. 205-211, 2004.

[18]   L. Liu and F. Samuel, "Effect of inclusions on the tensile properties of Al–7% Si–0.35% Mg (A356. 2) aluminium casting alloy," *Journal of Materials Science,* vol. 33, no. 9, pp. 2269-2281, 1998.

[19]   Q. G. Wang, P. N. Crepeau, C. J. Davidson, and J. R. Griffiths, "Oxide films, pores and the fatigue lives of cast aluminum alloys," *Metallurgical and Materials Transactions B,* journal article vol. 37, no. 6, pp. 887-895, 2006.

[20]   M. Tiryakioğlu, "On the relationship between statistical distributions of defect size and fatigue life in 7050-T7451 thick plate and A356-T6 castings," *Materials Science and Engineering: A,* vol. 520, no. 1, pp. 114-120, 2009.

[21]   M. Tiryakioğlu, "Relationship between Defect Size and Fatigue Life Distributions in Al-7 Pct Si-Mg Alloy Castings," *Metallurgical and Materials Transactions A,* vol. 40, no. 7, pp. 1623-1630, 2009.

[22]   J.-M. D. I. Farup, M. Rappaz, "IN SITU OBSERVATION OF HOT TEARING FORMATION IN SUCCINONITRILE ACETONE," *Acta Materialia,* vol. 49, pp. 1261-1269, 2001.

[23]   T. C. Piwonka and M. C. Flemings, "Pore formation is solidification," *Transactions of the Metallurgical Society of AIME,* vol. 236, pp. 1157-1165, 1966.

[24]   G. Timelli and D. Caliari, "Influence of Process Parameters on the Microstructure and Casting Defects of a LPDC Engine Block," M. Tiryakioğlu, M. Jolly, and G. Byczynski, Eds. Cham: Springer International Publishing, 2016, pp. 151-158.

[25]   P. Beeley, *Foundry technology*. Butterworth-Heinemann, 2001.

[26]   D. G. E. L. Katgerman, "In Search of Prediction of Hot Cracking in Aluminium Alloys," in *Hot Cracking Phenomena in Welds II*, H. H. Thomas Bollinghaus, Carl E. Cross, John C. Lippold, Ed. Berlin: Springer, 2008, pp. 3-18.

[27]   A. Nazarboland and R. Elliott, "The effect of intrinsic casting defects on the mechanical properties of austempered, alloyed ductile iron," *International Journal of Cast Metals Research,* vol. 10, no. 2, pp. 87-97, 1997/09/01 1997.

[28]   K. A. Jackson and J. D. Hunt, "Transparent compounds that freeze like metals," *Acta Metallurgica,* vol. 13, no. 11, pp. 1212-1215, 1965/11/01 1965.

[29]   Q. Han, "Motion of bubbles in the mushy zone," *Scripta Materialia,* vol. 55, no. 10, pp. 871-874, 2006.

[30]   W. C. McCrone, *Fusion Methods in Chemical Microscopy*. Interscience Publishers, 1957.

[31]   E. M. Chamot and C. W. Mason, "Handbook of chemical microscopy," 1958.

[32]   J. D. Hunt, K. A. Jackson, and H. Brown, "Temperature Gradient Microscope Stage Suitable for Freezing Materials with Melting Points between −100 and +200°C," *Review of Scientific Instruments,* vol. 37, no. 6, pp. 805-805, 1966.

[33]   W. F. Kaukler, "Hot stage and sample cell design for the solidification of transparent materials with and without forced convection," *Review of Scientific Instruments,* vol. 55, no. 10, pp. 1643-1647, 1984.

[34]   P. D. Lee and J. D. Hunt, "Hydrogen porosity in directional solidified aluminium-copper alloys:in situ observation," *Acta Materialia,* vol. 45, no. 10, pp. 4155-4169, 1997.

[35]   L. Arnberg and R. H. Mathiesen, "The real-time, high-resolution x-ray video microscopy of solidification in aluminum alloys," *JOM,* journal article vol. 59, no. 8, pp. 20-26, 2007.

[36]   H. Yin and J. N. Koster, "In-situ Observed Pore Formation During Solidification of Aluminium," *ISIJ International,* vol. 40, no. 4, pp. 364-372, 2000.

[37]   A. V. Catalina, S. Sen, D. M. Stefanescu, and W. F. Kaukler, "Interaction of porosity with a planar solid/liquid interface," *Metallurgical and Materials Transactions A,* journal article vol. 35, no. 5, pp. 1525-1538, 2004.

[38]   P. Lee and J. Hunt, "Hydrogen porosity in directional solidified aluminium-copper alloys: in situ observation," *Acta Materialia,* vol. 45, no. 10, pp. 4155-4169, 1997.

[39]   A. Murphy, D. Browne, Y. Houltz, and R. Mathiesen, "In situ X-ray observations of gas porosity interactions with dendritic microstructures during solidification of Al-based alloys," in *IOP Conference Series: Materials Science and Engineering*, 2016, vol. 117, no. 1, p. 012067: IOP Publishing.

[40]   Z. Lei, L. Hengcheng, P. Ye, W. Qigui, and S. Guoxiong, "In-situ observation of porosity formation during directional solidification of Al-Si Casting Alloys," *Research & Development,* 2011.

[41]   E. Kato, "Pore nucleation in solidifying high-purity copper," *Metallurgical and Materials Transactions A,* journal article vol. 30, no. 9, pp. 2449-2453, 1999.

[42]   M. Volmer and A. Weber, "Keimbildung in Tibersatting Gebilden," *Zeitschrift für physikalisch Chemie,* vol. 119, pp. 277-301, 1926.

[43]   M. Volmer, *Kinetics of phase formation*. Cambridge, Mass.: Air Force Cambridge Reasarch Center, Geophysics Research Division, Atmospheric Physics Laboratory, 1940.

[44]   R. Becker and W. Döring, "Kinetische Behandlung der Keimbildung in übersättigten Dämpfen," *Annalen der Physik,* vol. 416, no. 8, pp. 719-752, 1935.

[45]   J. W. Gibbs, H. A. Bumstead, and R. G. Van Name, *Scientific Papers of J. Willard Gibbs ...: Thermodynamics* (Scientific Papers of J. Willard Gibbs). Longmans, Green and Company, 1906.

[46]   J. H. Hollomon and D. Turnbull, "Nucleation," *Progress in Metal Physics,* vol. 4, pp. 333-388, 1953.

[47]   J. P. Hirth and G. M. Pound, *Condensation and Evaporation: Nucleation and Growth Kinetics*. Macmillan, 1963.

[48]   J. P. Hirth, G. M. Pound, and G. R. St. Pierre, "Bubble nucleation," *Metallurgical Transactions,* vol. 1, no. 4, pp. 939-945, 1970.

[49]   F. G. Blake, *The tensile strength of liquids a review of the literature*. Cambridge, Mass.: Acoustics Research Laboratory, Dept. of Engineering Sciences and Applied Physics, Harvard University, 1954.

[50]   J. Frenkel, *Kinetic Theory of Liquids* (Dover Publications). Dover, 1955, pp. 174-182.

[51]   J. A. Clark, "The thermodynamics of bubbles," Cambridge, Mass.1956, Available: http://hdl.handle.net/1721.1/61459.

[52]   S. F. Jones, G. M. Evans, and K. P. Galvin, "Bubble nucleation from gas cavities — a review," *Advances in Colloid and Interface Science,* vol. 80, no. 1, pp. 27-50, 1999.

[53]   J. C. Fisher, "The fracture of liquids," *Journal of Applied Physics,* vol. 19, no. 11, pp. 1062-1067, 1948.

[54]   P. D. Lee, A. Chirazi, and D. See, "Modeling microporosity in aluminum–silicon alloys: a review," *Journal of Light Metals,* vol. 1, no. 1, pp. 15-30, 2001.

[55]   K. Kubo and R. D. Pehlke, "Mathematical modeling of porosity formation in solidification," *Metallurgical Transactions B,* vol. 16, no. 2, pp. 359-366, 1985.

[56]   I. Katzarov and J. Popov, "Pore formation in hot spots," *International journal of heat and mass transfer,* vol. 39, no. 14, pp. 2861-2867, 1996.

[57]   D. R. Poirier, K. Yeum, and A. L. Maples, "A thermodynamic prediction for microporosity formation in aluminum-rich Al-Cu alloys," *Metallurgical Transactions A,* vol. 18, no. 11, pp. 1979-1987, 1987.

[58] Q. T. Fang and D. A. Granger, "Prediction of pore size due to rejection of hydrogen during solidification of aluminum alloys," pp. 927-935.

[59] I. J. Chiou and H. L. Tsai, "Modeling of porosity formation in castings," *AFS Transactions,* vol. 98, pp. 823-830, 1990.

[60] J. D. Zhu and I. Ohnaka, "Computer simulation of interdendritic porosity in aluminum alloy ingots and casting," *Modeling of Casting, Welding and Advanced Solidification Processes,* vol. V, pp. 435-442, 1991.

[61] P. Lee and J. Hunt, "A model of the interaction of porosity and the developing microstructure," Minerals, Metals and Materials Society, Warrendale, PA (United States)1995.

[62] P. D. Lee, D. See, and R. C. Atwood, "Porosity formation during solidification±a comparison of micro modelling approaches," *Cutting Edge of Computer Simulation of Solidification and Casting,* pp. 97-111, 1999.

[63] P. D. Lee, R. C. Atwood, R. J. Dashwood, and H. Nagaumi, "Modeling of porosity formation in direct chill cast aluminum–magnesium alloys," *Materials Science and Engineering: A,* vol. 328, no. 1, pp. 213-222, 2002.

[64] J. G. Conley, J. Huang, J. Asada, and K. Akiba, "Modeling the effects of cooling rate, hydrogen content, grain refiner and modifier on microporosity formation in Al A356 alloys," *Materials Science and Engineering A,* vol. 285, no. 1-2, pp. 49-55, 2000.

[65] J. Huang, J. G. Conley, and T. Mori, "Simulation of microporosity formation in modified and unmodified A356 alloy castings," *Metallurgical and Materials Transactions B,* vol. 29, no. 6, pp. 1249-1260, 1998.

[66] R. C. Atwood, S. Sridhar, W. Zhang, and P. D. Lee, "Diffusion-controlled growth of hydrogen pores in aluminium–silicon castings: in situ observation and modelling," *Acta materialia,* vol. 48, no. 2, pp. 405-417, 2000.

[67] D. M. Stefanescu, "Computer simulation of shrinkage related defects in metal castings – a review," *International Journal of Cast Metals Research,* vol. 18, no. 3, pp. 129-143, 2005.

[68] D. M. Stefanescu and A. V. Catalina, "Physics of microporosity formation in casting alloys – sensitivity analysis for Al–Si alloys," *International Journal of Cast Metals Research,* vol. 24, no. 3-4, pp. 144-150, 2011.

[69] J. C. Fisher, J. H. Hollomon, and D. Turnbull, "Nucleation," *Journal of Applied Physics,* vol. 19, no. 8, 1948.

[70] S. G. Bankoff, "Ebullition from solid surfaces in the absence of a pre-existing gaseous phase," *Transactions of the American Society of Mechanical Engineers,* vol. 79, pp. 735-740, 1957.

[71] L. Bernath, "Theory of Bubble Formation in Liquids," *Industrial & Engineering Chemistry,* vol. 44, no. 6, pp. 1310-1313, 1952.

[72] W. F. Gale and T. C. Totemeier, *Smithells metals reference book*. Butterworth-Heinemann, 2003.

[73] L. Bernath, "Theory of Bubble Formation in Liquids," *Industrial & Engineering Chemistry,* vol. 44, no. 6, pp. 1310-1313, 1952.

[74] T. Bazhirov, G. Norman, and V. Stegailov, "Cavitation in liquid metals under negative pressures. Molecular dynamics modeling and simulation," *Journal of Physics: Condensed Matter,* vol. 20, no. 11, p. 114113, 2008.

[75] Z. Insepov, A. Hassanein, T. Bazhirov, G. Norman, and V. Stegailov, "Molecular dynamics simulations of bubble formation and cavitation in liquid metals," *Fusion Science and Technology,* vol. 52, no. 4, pp. 885-889, 2007.

[76]   P. Yousefian and M. Tiryakioğlu, "Theoretical Calculations for Pore Formation in Molten Metals During Solidification," presented at the Defects and Properties of Cast Metals (TMS 2017), San Diego, California, USA, 2017.

[77]   M. M. Martynyuk, "Ideal tensile strength of metals on the basis of a generalized Van der Waals equation," *Journal of Engineering Physics and Thermophysics,* journal article vol. 72, no. 4, pp. 682-686, 1999.

[78]   H. Fredriksson, M. Haddad-Sabzevar, K. Hansson, and J. Kron, "Theory of hot crack formation," *Materials Science and Technology,* vol. 21, no. 5, pp. 521-530, 2005.

[79]   S. J. Zinkle, L. E. Seitzman, and W. G. Wolfer, "I. Energy calculations for pure metals," *Philosophical Magazine A,* vol. 55, no. 1, pp. 111-125, 1987.

[80]   H. Brooks, *Impurities and Imperfections*. Ohio: ASM Seminar, 1955.

[81]   K. A. Jackson, "The nucleation of dislocation loops from vacancies," *Philosophical Magazine,* vol. 7, no. 79, pp. 1117-1127, 1962.

[82]   G. Thomas and R. H. Willens, "Defects in aluminum quenched from the liquid state," *Acta Metallurgica,* vol. 12, no. 2, pp. 191-196, 1964.

[83]   G. Thomas and R. H. Willens, "Vacancy concentrations in quenched aluminum," *Acta Metallurgica,* vol. 14, no. 10, pp. 1385-1390, 1966.

[84]   D. Kuhlmann-Wilsdorf and H. G. F. Wilsdorf, "On The Behavior of Thermal Vacancies in Pure Aluminum," *Journal of Applied Physics,* vol. 31, no. 3, pp. 516-525, 1960.

[85]   G. Thomas and R. Willens, "Defects in Aluminum Quenched from the Liquid State," DTIC Document1963.

[86]   J. P. Perdew, Y. Wang, and E. Engel, "Liquid-drop model for crystalline metals: Vacancy-formation, cohesive, and face-dependent surface energies," *Phys. Rev. Lett.,* vol. 66, no. 4, pp. 508-511, 1991.

[87]   J. A. Sigler and D. Kuhlmann-Wilsdorf, "Calculations on the Mechanical Energy of Vacancy Condensation Loops, Stacking Fault Tetrahedra, and Voids," *physica status solidi (b),* vol. 21, no. 2, pp. 545-556, 1967.

[88]   M. R. Mruzik and K. C. Russell, "Equilibrium forms of small voids in metals," *Surface Science,* vol. 67, no. 1, pp. 205-225, 1977/10/01 1977.

[89]   A. Si-Ahmed and W. Wolfer, "Effect of radiation-induced segregation on void nucleation," *Am. Soc. Test. Mater., Spec. Tech. Publ.;(United States),* vol. 782, no. CONF-820628-, 1982.

[90]   C. Ransley and H. Neufeld, "The solubility of hydrogen in liquid and solid aluminium," *Journal of the Institute of Metals,* vol. 74, no. 12, pp. 599-620, 1948.

[91]   W. Eichenauer, "THE SOLUBILITY OF HYDROGEN AND DEUTERIUM IN HIGH- PURITY ALUMINIUM AT 400-630 C," *Z METALLKUNDE,* vol. 59, no. 8, pp. 613-616, 1968.

[92]   S. Zinkle, W. Wolfer, G. Kulcinski, and L. Seitzman, "Stability of vacancy clusters in metals. II. Effect of oxygen and helium on void formation in metals," *Philosophical Magazine A,* vol. 55, no. 1, pp. 127-140, 1987.

[93]   S. Yoshiharu and M. Yoshijiro, "Formation of Voids in Pure Aluminum Quenched in Hydrogen Gas," *Japanese Journal of Applied Physics,* vol. 20, no. 10, p. 1787, 1981.

[94]   W. Kazuto, M. Yumi, Y. Hiroyuki, and Y. Sho, "Effect of Helium and Hydrogen Atoms on the Formation of Voids in Quenched Aluminium," *Japanese Journal of Applied Physics,* vol. 20, no. 10, p. 1791, 1981.

[95]   M. Kiritani, "Formation of Voids and Dislocation Loops in Quenched Aluminum," *Journal of the Physical Society of Japan,* vol. 19, no. 5, pp. 618-631, 1964/05/15 1964.

[96]   G. Das and J. Washburn, "Defects formed from excess vacancies in aluminum," *Philosophical Magazine,* vol. 11, no. 113, pp. 955-967, 1965.

[97]   M. A. S. A. Chaudhuri, B.J. Diak, C. Cuoppolo & A.R. Woll, "Nanovoid characterization of nominally pure aluminium using synchrotron small angle X-ray Scattering (SAXS) methods," *Philosophical Magazine,* vol. 93, no. 35, pp. 4392-4411, 2013/12/01 2013.

[98]   E. D. Hondros, "The effect of adsorbed oxygen on the surface energy of B.C.C. iron," *Acta Metallurgica,* vol. 16, no. 11, pp. 1377-1380, 1968/11/01 1968.

[99]   C. Bauer, R. Speiser, and J. Hirth, "Surface energy of copper as a function of oxygen activity," *Metallurgical and Materials Transactions A,* vol. 7, no. 1, pp. 75-79, 1976.

[100] M. F. Felsen and P. Regnier, "Influence of some additional elements on the surface tension of copper at intermediate and high temperatures," *Surface Science,* vol. 68, pp. 410-418, 1977/11/01 1977.

[101] I. F. Bainbridge and J. A. Taylor, "The Surface Tension of Pure Aluminum and Aluminum Alloys," *Metallurgical and Materials Transactions A,* vol. 44, no. 8, pp. 3901-3909, 2013.

[102] I. Egry, E. Ricci, R. Novakovic, and S. Ozawa, "Surface tension of liquid metals and alloys — Recent developments," *Advances in Colloid and Interface Science,* vol. 159, no. 2, pp. 198-212, 2010.

[103] F. A. Halden and W. D. Kingery, "Surface Tension at Elevated Temperatures. II. Effect of C, N, O and S on Liquid Iron Surface Tension and Interfacial Energy with Al2O3," *The Journal of Physical Chemistry,* vol. 59, no. 6, pp. 557-559, 1955.

[104] D. Sageman, "SURFACE TENSION OF MOLTEN METALS USING THE SESSILE DROP METHOD," Ames Lab., Iowa1972.

[105] E. Whittenberger and F. Rhines, "Origin of porosity in castings of magnesium-aluminum and other alloys," *Journal of metals,* vol. 7, pp. 409-420, 1952.

[106] B. Chalmers, "Principles of Solidification," in *Applied Solid State Physics*, W. Low and M. Schieber, Eds. Boston, MA: Springer US, 1970, pp. 161-170.

[107] J. Campbell, "The Origin of Griffith Cracks," *Metallurgical and Materials Transactions B,* journal article vol. 42, no. 6, pp. 1091-1097, 2011.

[108] J. Campbell, "Invisible macrodefects in castings," (in English), *Journal de Physique IV Colloque,* vol. 03, no. C7, pp. C7-861-C7-872, 1993 1993.

[109] J. Runyoro, S. Boutorabi, and J. Campbell, "Critical gate velocities for film-forming casting alloys: a basis for process specification," *AFS Transactions,* vol. 100, pp. 225-234, 1992.

[110] M. Divandari, "Mechanism of Bubble Damage in Castings," PhD, School of Metallurgy and Materials, University of Birmingham, Birmingham, UK, 1999.

[111] S. Fox and J. Campbell, "Visualisation of oxide film defects during solidification of aluminium alloys," *Scripta Materialia,* vol. 43, no. 10, pp. 881-886, 10/30/ 2000.

[112] S. Boutorabi, J. Campbell, and J. J. Runyoro, "Critical Gate Velocity for Film-Forming Casting Alloys; A Basis for Process Specifications," 1997.

[113] D. Mackie, J. Robson, P. Withers, and M. Turski, "Characterisation and modelling of defect formation in direct-chill cast AZ80 alloy," *Materials Characterization,* vol. 104, pp. 116-123, 2015.

[114] A. Shafaei and R. Raiszadeh, "Reduced Pressure Test Verification of Healing of Double Oxide Film Defects in Al-Mg Alloys," *Metallurgical and Materials Transactions B,* vol. 45, no. 6, pp. 2486-2494, 2014// 2014.

[115] M. Tang and P. C. Pistorius, "Oxides, porosity and fatigue performance of AlSi10Mg parts produced by selective laser melting," *International Journal of Fatigue,* vol. 94, Part 2, pp. 192-201, 1// 2017.

[116] Y. Fukai and N. Ōkuma, "Evidence of Copious Vacancy Formation in Ni and Pd under a High Hydrogen Pressure," *Japanese Journal of Applied Physics,* vol. 32, no. 9A, pp. L1256-L1256, 1993.

[117] H. K. Birnbaum *et al.*, "Hydrogen in aluminum," *Journal of Alloys and Compounds,* vol. 253, pp. 260-264, 1997.

[118] A. I. Kartamyshev, D. D. Vo, and A. G. Lipnitskii, "The interaction between light impurities and vacancies in titanium and aluminum metals: A DFT study," *St. Petersburg Polytechnical University Journal: Physics and Mathematics,* vol. 2, no. 2, pp. 96-102, 2016.

[119] G. Lu and E. Kaxiras, "Hydrogen Embrittlement of Aluminum: The Crucial Role of Vacancies," *Physical Review Letters,* vol. 94, no. 15, p. 155501, 04/18/ 2005.

[120] K. Tynelius, J. Major, and D. Apelian, "A parametric study of microporosity in the A356 casting alloy system," *TRANSACTIONS-AMERICAN FOUNDRYMENS SOCIETY,* pp. 401-413, 1993.

[121] J. Campbell, "Entrainment defects," *Materials Science and Technology,* vol. 22, no. 2, pp. 127-145, 2006.

[122] H. Dvorak and E. Schwegtier, "Statistical distribution of flaw sizes," *International Journal of Fracture Mechanics,* vol. 8, no. 1, pp. 110-111, 1972.

[123] M. Tiryakioğlu, "Pore size distributions in AM50 Mg alloy die castings," *Materials Science and Engineering: A,* vol. 465, no. 1, pp. 287-289, 2007.

[124] M. Tiryakioğlu, "On fatigue life variability in cast Al–10% Si–Mg alloys," *Materials Science and Engineering: A,* vol. 527, no. 6, pp. 1560-1564, 2010.

[125] M. Uludağ, R. Çetin, D. Dispinar, and M. Tiryakioğlu, "Characterization of the Effect of Melt Treatments on Melt Quality in Al-7wt %Si-Mg Alloys," *Metals,* vol. 7, no. 5, p. 157, 2017.

[126] T. W. Anderson and D. A. Darling, "A Test of Goodness of Fit," *Journal of the American Statistical Association,* vol. 49, no. 268, pp. 765-769, 1954/12/01 1954.

[127] M. Tiryakioğlu and J. Campbell, "Weibull Analysis of Mechanical Data for Castings: A Guide to the Interpretation of Probability Plots," *Metallurgical and Materials Transactions A,* vol. 41, no. 12, pp. 3121-3129, 2010.

[128] K. M. Gruenberg, B. A. Craig, B. M. Hillberry, R. J. Bucci, and A. J. Hinkle, "Predicting fatigue life of pre-corroded 2024-T3 aluminum," *International Journal of Fatigue,* vol. 26, no. 6, pp. 629-640, 6// 2004.

[129] X. Cao and J. Campbell, "The nucleation of Fe-rich phases on oxide films in Al-11.5 Si-0.4 Mg cast alloys," *Metallurgical and Materials Transactions A,* vol. 34, no. 7, pp. 1409-1420, 2003.

[130] X. Cao and J. Campbell, "The solidification characteristics of Fe-rich intermetallics in Al-11.5Si-0.4Mg cast alloys," *Metallurgical and Materials Transactions A,* journal article vol. 35, no. 5, pp. 1425-1435, 2004.

[131] D. N. Miller, L. Lu, and A. K. Dahle, "The role of oxides in the formation of primary iron intermetallics in an Al-11.6Si-0.37Mg alloy," *Metallurgical and Materials Transactions B,* journal article vol. 37, no. 6, pp. 873-878, 2006.

[132] L. Liu, A. Samuel, F. Samuel, H. Doty, and S. Valtierra, "Influence of oxides on porosity formation in Sr-treated Al-Si casting alloys," *Journal of materials science,* vol. 38, no. 6, pp. 1255-1267, 2003.

[133] J. Campbell, "An overview of the effects of bifilms on the structure and properties of cast alloys," *Metallurgical and Materials Transactions B,* journal article vol. 37, no. 6, pp. 857-863, 2006.

[134] M. Tiryakioğlu and R. T. Shuey, "Quench sensitivity of an Al-7 Pct Si-0.6 Pct Mg alloy: characterization and modeling," *Metallurgical and Materials Transactions B,* vol. 38, no. 4, pp. 575-582, 2007.

[135] C. J. Davidson, T. R. Finlayson, M. E. Fitzpatrick, J. R. Griffiths, E. C. Oliver, and Q. Wang, "Observations of the stress developed in Si inclusions following plastic flow in the matrix of an Al–Si–Mg alloy," *Philosophical Magazine,* vol. 97, no. 17, pp. 1398-1417, 2017.

Curriculum Vitae
Pedram Yousefian

Education

M.Sc. in Mechanical Engineering   **Spring 2016 – Summer 2017**
University of North Florida (UNF), FL, USA

Thesis Subject: on the Formation of Pores in Aluminum Castings and Their Extrinsic Effect on Casting Performance
Supervisor: Prof. M. Tiryakioglu

Current GPA: 4.0/4.0

B.Sc. in Materials Engineering   **2009-2014**
Isfahan University of Technology (IUT), Isfahan, Iran

Final Project: Production of Rheo Centrifuged Cast Iron in Sand Mold.
Supervisor: Prof. B. Niroumand

GPA: 15.71 / 20
Last 2 years' GPA: 17.09 / 20

Diploma in Mathematics and Physics Discipline   **2006-2009**
Shahid Ejei High school (NODET)[1], Isfahan, Iran

Honors and Awards

- **Awarded graduate scholarship** by University of North Florida (UNF)   2015-Present
- **7th Place** in the 10th National Heat Treatment Competitions   2013
- **2nd Place** in "Topical" section in the 1st International Metallography Competition 2012
- **2nd Place** in "Software" section in the 1st International Metallography Competition2012
- **Ranked 1st in Department** in the National University Entrance Exam   2009
- **Awarded scholarship** by NIOC (National Iranian Oil Company), Offered to top students in order of cumulative GPA   2009-2013
- **Ranked in the top 0.5%** of participants in Iranian University Entrance Exam, **Among 500,000** participants in mathematics-physics branch   2009
- Selected and honored in the first round of National Chemistry Olympiad   2006

Publications & Patents:

➢ P. Yousefian, M. Tiryakioglu," Theoretical Calculations for Pore Formation in Aluminum During Solidification", accepted for oral presentation at Defects and Properties of Cast Metals, TMS 2017.

---

[1] Exceptional Talents Schools are special centers of education, directed by NODET (National Organization for Development of Exceptional Talents), an organization to choose the most talented students by taking exams all over the country and each year only 100 students in each province get qualified to study at these schools.

➢ A. Timpanaro, P. Yousefian, O. P. Keifer, P. D. Eason, "Analysis of Polypropylene Refrigerator Filter Failure", under publication.

➢ **Patent:** A single stage semi-solid centrifuged method for casting of high melting point alloys in sand mold

➢ **Co-operation** in Manufacturing "High Temperature Pin on Disk Wear Testing Machine" **(Patent)**

Certificates & Membership

- Member of The American Society of Mechanical Engineers   2016-Present
- Member of The Minerals, Metals and Materials Society   2016-Present
- Certificate of participation in training workshop on "key to steel"
  Presented by Prof. Ahmad Saatchi   2012
- Certificate of participation in training workshop on "TEM"
  Presented by Prof. Pirooz Marashi   2012
- Certificate of participation in training workshop on "X'pert"   2012
- Certificate of "Visual Testing Level II"
  Authorized by A. Tabrizian sponsored by Germanischer Lioyd   2012
- Certificate of qualification in the 9th National Heat Treatment Competitions   2012
- Certificate of qualification in the 1st National Student Foundry Competitions   2012
- Certificate of participation in training workshop on Defects in Castings
  Presented by Prof. Jalal Hejazi   2011

Teaching & Internship Experience:

- **Teaching Assistant** for "Integrated Design & Manufacturing Lab"   2016-2017
  - ➢ Teach students how to operate manual and CNC Lathe and Milling Machines
  - ➢ Reviewed CAM files generated by students and run them on CNC HAAS mill
- **Teaching Assistant** for "Materials Science"   Fall 2016
- **Teaching Assistant** for "Introduction to Engineering I"   Summer 2016
- **Teaching Assistant** for "Solidification of Metals"   2012-2014
- **Engineer** in Gostaresh Tejarat Farasoo Co.   2014
  Assistant Manager of R&D and Manufacturing group, focusing on diecast and plastic injection mold design.
- **Summer Internship** Godaz Sanat Co., 320 hours.   2013
  Assistant Factory Manager in "GZ Co.", Alloy Steel Casting Foundry.
- **Internship** Daghigh Rizan Paya Hadid Co.**,** 200 hours.   2012
  Assistant production manager, Investment Casting Manufacturing Company.
- **Part-Time Intern** in Irmantech Sepahan Co.   2011- 2012
  R&D group, job consisted of research on "IR Window" and "Design and construction of composite container".
- **Internship** in Mana Ghete Sepahan Co.   2011- 2012
  R&D group to Reverse Engineering from "Inconel Turbocharger" for manufacturing.
- **Member of executive council** in Shahid Ejei Cultural Convention   2007- 2015
  (The NGO that does cultural activity, combination of citizenship learning, debate club, sport club, and scouting.)
- **Executive member of** in Cultural Convention of Materials Eng. Dept. at IUT   2010-2014
  Director of monthly scientific and cultural seminars in Materials Eng. department.

Skills

- Skillful in technical software related to materials and mechanical engineering such as **Catia, SolidWork, Autodesk Fusion 360, NX (FEA), ProCast, X'pert, PowerMill and Image J**
- Skilled in operating **Manual and CNC Lathe and Milling Machines**, **Materials Testing Machines**
- Skilled in **Casting**, **Heat Treatment, and Welding**
- Familiar with **PLC** systems